UNIVERSITÀ DELLA CALABRIA

UNIVERSITA' DELLA CALABRIA

Dipartimento di Fisica

Dottorato di Ricerca in

Scienze e Tecnologie Fisiche, Chimiche e dei Materiali

CICLO

XXXII

TITOLO TESI

Optical and mechanical responses of liquid crystals under confinement

Settore Scientifico Disciplinare FIS07

Coordinatore: Ch.ma Prof.s[illegible] Cipparrone

Firma [redacted]

Firma oscurata in base alle linee guida del Garante della privacy

Supervisore/Tutor: Dott. Bruno [redacted]

Firma [redacted]

Dottorando: Dott. Weichao Zheng

Fi[redacted]

Firma oscurata in base alle linee guida del Garante della privacy

Table of Contents

Abstract

The optics of liquid crystals (LCs) lay an important foundation for LC displays and the mechanics of LCs are the backbones of LC elastomers that are promising materials for artificial muscles. Despite broad prospects for applications, it is still a challenge to precisely measure both optics and mechanics at the nanoscale. Here both optical and mechanical responses are simultaneously probed by the Surface Forces Apparatus to understand how optical anisotropies of LCs interact with the birefringence of the mica, and how mechanical anisotropies of LCs interact with anchoring conditions and the confinement.

Optically, the birefringence of nematics adds complexities to the two intrinsic birefringent mica surfaces for multiple-beam interference. The phase retardation by multiple birefringent layers is a result of composition by the phase retardation from each layer and their relative intersection angles, which is intuitively understood by the parallelogram rule that is similar to the geometrical composition of forces but with double intersection angle. The simulation based on 4x4 matrices is used to reconstruct the interaction of fringes and to compare the deviation of average wavelengths in the same chromatic order and isotropic wavelengths generated by the average refractive indices.

Mechanically, LC behaviours result from the competition among surface anchoring, elasticity of LCs and confinements. During the retraction of surfaces, the neck of cholesteric layers is broken by the innermost circular dislocation defect that serves as a bulk crack with the opening mode of fracture, producing periodical twist transitions and structural forces. During the approach of surfaces, three regimes, constrained, stick-slip and sliding-slip, of cholesteric mechanical windings are observed with the time evolution

of the surface anchoring. The onset of three regimes and the retardation of twist transitions results from the balance between the twist elastic torque and the frictional surface torque, namely the anchoring torque and the viscous torque, which is analogous to friction torque in rotational friction. The deviation of the anchoring angle on surfaces provides evidence of interfacial ruptures, with tearing or sliding mode, described by the paradigm of fracture mechanics for the onset from static frictions to kinetic frictions. This thesis sheds light on the understanding of boundary effects on permeative flows, frictions, fractures, yield stress materials, adhesions and biomechanics.

Astratto

L'ottica dei cristalli liquidi (CLs) fornisce un importante supporto nel campo degli schermi a CL, e la meccanica dei CLs costituisce la spina dorsale dei cristalli liquidi elastomerici i quali sono materiali promettenti per i muscoli artificiali. Nonostante le vaste prospettive di applicazione, accurate misurazioni ottiche e meccaniche su scala nanometrica sono ancora una sfida aperta. In tale ambito le risposte ottiche e meccaniche sono simultaneamente testate dall'apparato delle forze di superficie allo scopo di comprendere come le anisotropie ottiche dei CLs interagiscono con la birifrangenza della mica, e come le anisotropie meccaniche dei CLs interagiscono con le condizioni di ancoraggio e con il confinamento.

Otticamente, la birifrangenza dei nematici aggiunge complessità alle due superfici di mica intrinsecamente birifrangenti a causa dell'interferenza a più fasci. Il ritardo di fase di più strati birifrangenti è il risultato della composizione dei ritardi di fase di ciascuno strato e dai loro relativi angoli di inserzione. Ciò si comprende in modo intuitivo dalla regola del parallelogramma, che è simile alla composizione geometrica delle forze, ma con un duplice angolo di inserzione. La simulazione basata sulle matrici 4x4 è usata per ricostruire le interazioni delle frange e per confrontare la deviazione delle lunghezze d'onda medie nello stesso ordine cromatico, nonché le lunghezze d'onda isotropiche generate dalla media degli indici di rifrazione.

Dal punto di vista meccanico, i comportamenti dei CLs sono il risultato della competizione fra l'ancoraggio di superficie, l'elasticità dei CLs e il confinamento. Durante la retrazione delle superfici la porzione degli strati colesterici soggetta a tensione è rotta dal difetto di dislocazione circolare più interno che funge da spaccatura di volume con

modalità di frattura aperta, producendo transizioni di twist periodiche e forze strutturali. Nell'avvicinamento delle superfici si osservano tre regimi a carico dell'inviluppo meccanico dei colesterici con evoluzione temporale dell'ancoraggio di superficie: regime vincolato, adesione allo scorrimento (stick-slip) e slittamento (sliding-slip). L'instaurazione dei tre regimi e il ritardo delle transizioni di twist risultano dal bilancio tra la coppia di torsione elastica e la coppia di attrito di superficie, cioè la coppia di ancoraggo e la coppia viscosa, che è l'analogo della coppia di attrito rotazionale. La deviazione dell'angolo di ancoraggio sulla superficie fornisce l'evidenza di rotture all'interfaccia, con modalità di strappo e scorrimento, descritte dal paradigma della meccanica della frattura per il passaggio dagli attriti statici a quelli dinamici. Questa tesi vuole gettare luce sulla comprensione degli effetti di confine in flussi permeativi, attriti, fratture, tensione di snervamento dei materiali, adesione e biomeccanica.

Declaration

This thesis is submitted for the degree of Doctor of Philosophy in the Department of Physics at the University of Calabria. No part of this thesis has been accepted or is currently being submitted for any degree, diploma, certificate, or other qualification in this University or elsewhere. This thesis is my own work, except where indicated.

1 Introduction

1.1 Liquid crystals

1.1.1 Liquid crystal phases

Liquid crystals (LCs) are central to a huge commercial market worth 100 billion dollars each year mainly in LC displays[1]. On top of this, they are also of great scientific interest for the fundamental understanding of condensed matter structure[2], biological self-assembly[3] and even cosmic strings[4]. As the name implies, LCs are a mesophase[2] connecting liquids and crystals. There are two types of LCs that are formed by rigid rod-like or disc-like molecules, namely thermotropic LCs that are temperature-dependent and lyotropic LCs that are mainly concentration-dependent. For both types, several phases are formed during phase transition depending on either temperature or concentration, shown in Fig. 1.1.

For thermotropic LCs, an isotropic phase that is similar to a simple liquid is formed at high temperature, with molecules freely moving and rotating without any positional or orientational order[2]. By decreasing the temperature from the isotropic phase a phase transition can occur, shown in Fig. 1.1. The long axis of the rod or the axis perpendicular to the plane of the disc, tends to point along a certain direction, called *director* **n**, introducing orientational order but still lacking positional order. This is known as a *nematic* phase. At this nematic phase, if the molecules are chiral[5-7] or are subjected to structure mismatch[8], confinement[9] and chiral dopants[10], chiral nematic phases with periodic helical structures can also emerge, called *cholesterics*. Further lowering the temperature will result in a second transition a phase with orientational and one-

dimensional positional orders, known as a *smectic* phase. This positional order brings about layer structures with a periodic thickness comparable to the molecular length. Molecules mostly move within layers, but occasionally they also jump across layers called *self-diffusion*[11]. Furthermore, a *columnar* phase with orientational and two-dimensional positional order appears at a lower temperature, where molecules can only diffuse along one dimension parallel to the molecule direction. Finally, crystals with positional and orientational order arise where molecules vibrate around a hexagonal lattice point over a long time. Those phases mentioned above usually appear reversibly during heating up of the sample, though which phases occur will depend on molecular properties[12-15] of the LC, such as aspect ratio, rigidity and polydispersity.

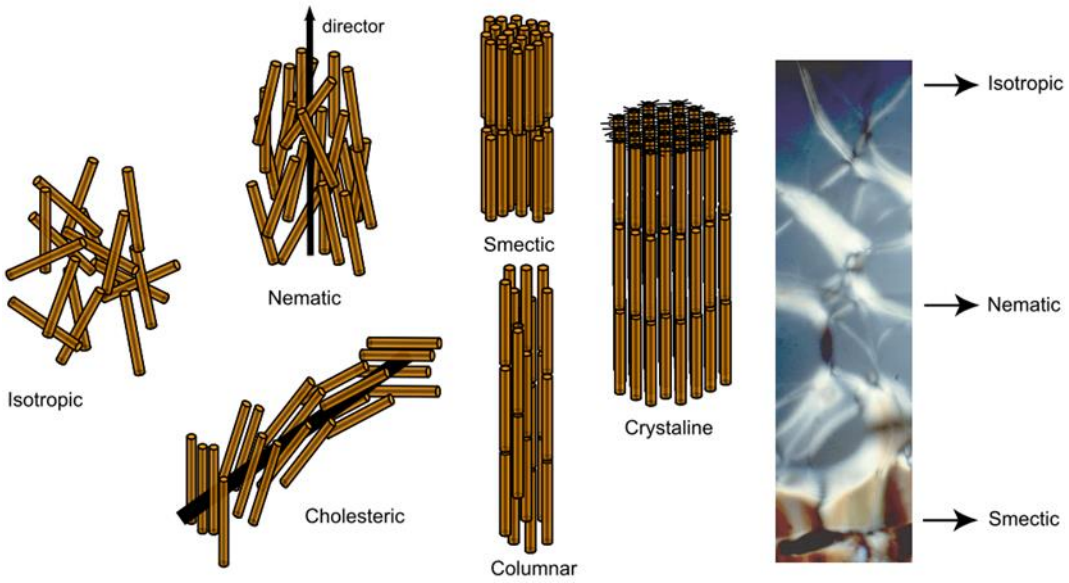

Figure 1.1 Schematic diagram of different LC phases and density-induced phase separation in the experimental sample, the figure is adapted from reference[16].

The nematic-isotropic transition is usually a first-order transition that is discontinuous, unless molecules are strongly confined on the surface or by geometry[17]. The transitions

between phases are characterized by an orientational order parameter[2] S as shown in Fig. 1.2a,

$$S = \langle \frac{3\cos^2\delta - 1}{2} \rangle \quad (1.1)$$

where δ is the angle between the molecular axis and the director **n**, and < > is the average over all molecules. If all molecules are parallel to the **n**, δ is 0 producing S = 1, whereas, in the isotropic phase, molecules orient randomly giving S = 0. The order parameter S decreases from smectic C with molecules tilted on the layer planes to smectic A with molecules perpendicular to the layer planes, nematic then isotropic phase with increasing temperature, and the transitions between different phases are sharp[3], shown in Fig. 1.2a.

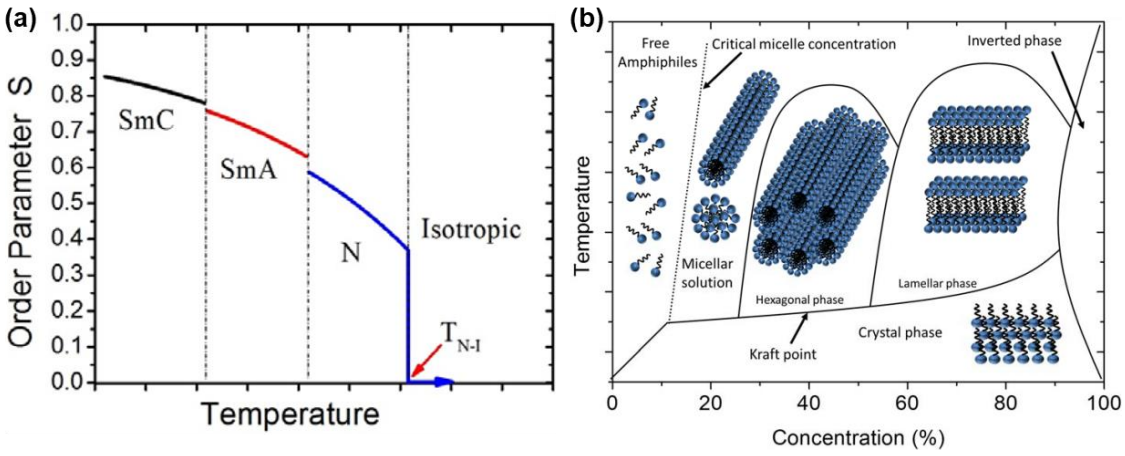

Figure 1.2 Phase diagram of thermotropic and lyotropic LCs. (a) Order parameter during the thermotropic phase transition from smectic C (SmC) to smectic A (SmA), nematic (N) and isotropic (I) phase as a function of temperature. (b) Lyotropic phase diagram as a function of temperature and concentration. The figure is adapted from reference[3].

Phase transitions in lyotropic LCs are mediated by the concentration of solute and temperature. However, the interaction between solute and solvent, such as the hydrophobic effect[18], also changes the morphology of self-assembly. For example, one

of the most common lyotropic LCs is formed by amphiphilic molecules that play an important role in cell membranes, shown in Fig. 1.2b. The most stable phase, whether spherical micelle to hexagonal phase or lamellar phases, is mainly determined by the packing parameter[19-21] which varies with concentration, which is consistent with free volume effect[22] for LCs.

1.1.2 Liquid crystal anisotropy

Like crystals, LCs also show anisotropy on both their optical and mechanical properties. Due to their flow properties, the anisotropies in LCs are even more complicated than in crystals. For example, when LCs are subjected to shear flow, there are 3 viscosities detected in different configurations of molecule orientation with respect to the shear gradient and shear direction, which are called Miesowicz viscosity coefficients[23]. The anisotropies actually simplify the applications by external control. Taking the dielectric anisotropy for instance, LCs can be controlled by electric fields, which is vital for LC display. More details about optical and mechanical anisotropies will be shown in section 2.2.

1.1.3 Frank free energy density

According to elastic continuum theory and ignoring molecular details of the LCs, Frank or distortion free energy density G_d is used to describe the free energy of a LC under distortion with three main elastic deformations:

$$G_d = \frac{1}{2}K_1(\nabla \cdot \mathbf{n})^2 + \frac{1}{2}K_2(\mathbf{n} \cdot \nabla \times \mathbf{n})^2 + \frac{1}{2}K_3(\mathbf{n} \times \nabla \times \mathbf{n})^2 \quad (1.2)$$

where K_1, K_2 and K_3 are the elastic constant of the fundamental splay, twist and bend distortion modes shown in Fig. 1.3. These elastic constants are typically 1-20 pN and play

a large role on the molecule distributions in a certain geometry thus also determining the defect positions[24, 25] and assisting self-assembly[26]. For instance, the splay-bend transition has been observed in a wedge when the opening angle increased, mediated by competition of boundary conditions, confinements and elastic constants[25].

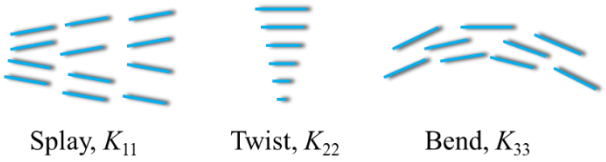

Figure 1.3 Schematic diagram of splay, twist and bend distortions in LCs, corresponding elastic constants are K_{11}, K_{22} and K_{33}.

A recent study[27] using atomistic molecular simulation has successfully extracted all the elastic constants from simulation, providing an understanding of the morphology of LCs confined in complicated geometries[28, 29] and allowing the design of new materials with a precise prediction of elastic interactions.

1.1.4 Defects in liquid crystals

The rotational symmetry of nematics is easily broken by local distortions, such as flow, boundary or fields, causing defects called disclinations including line and point defects[2]. One of the most profound phenomena is the tuneable defects around a spherical particle, shown in Fig. 1.4, where 3 types of defects are formed depending on particle boundary conditions called surface anchoring[26, 30-33]. With homeotropic anchoring where the molecular director is perpendicular to the particle surface, either dipolar hedgehog defect or Saturn-ring defect around particle equator are observed depending on the particle radius. The former defect is usually observed in larger particles[32]. With degenerate planar anchoring where directors of molecules are randomly distributed but parallel with the

surface, Boojum defects are found on both poles of the particle. Those defects with quadrupolar and dipolar symmetries can induce attractive elastic interaction analogous to electrostatics that assists and stabilizes self-assembly of colloidal lattices[26]. More complicated elastic hexadecapole, a combination of Saturn-ring and Boojum defects, which has also been reported by adjusting the conical surface anchoring[34, 35]. This symmetry breaking can also be hidden if a disk that is thin enough, less than 100 nm, is used to align LCs, in which case the LCs cannot be distorted by the foreign substance[36].

In cholesterics or smectics, breaking of translational symmetry, namely positional order, causes dislocations including edge and screw dislocations that are analogous to dislocations in solids. The edge dislocations in cholesterics are easily observed in the Grandjean-Grandjean-Cano wedge[37] since the period of rotation is large enough to be observed under an optical microscope. The position of dislocation in the edge is mediated by the competition of the boundary interaction and the Frank elastic energy[24]. With strong boundary interaction, the disorder of dislocations is repelled to the centre away from the surface, while it is attracted to the surface with weak boundary interaction.

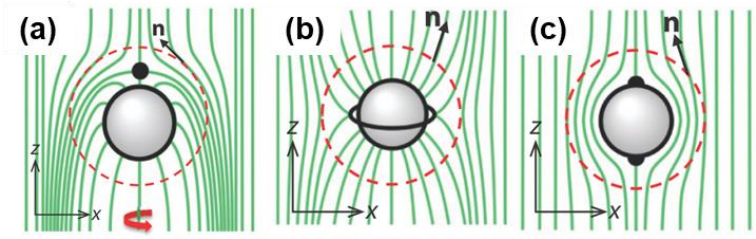

Figure 1.4 Defects formed around spherical particles, figures are adapted from reference[26]. (a) Dipolar hedgehog defect formed around particle with homeotropic anchoring and large radius. (b) Saturn-ring disclination defect around particle with homeotropic anchoring and small radius. (c) Boojum defects around particle with planar anchoring. Green lines are director **n** streamlines of LCs. Black dots and Saturn-ring are defects.

Defects in LCs act like totally melted regions where LC molecules self-diffuse faster compared with bulk[38]. However, this disordered region increases the viscosity for the diffusion of large particles which pin to the defects[39]. Therefore, those defects serve as a guided template to arrest and self-assemble particles[40] and the arrested particles, in turn, stabilize the defect network altering rheology and strengthening mechanical properties[41, 42].

1.2 Cholesteric liquid crystals

1.2.1 Tuneable selective reflection

On one hand, cholesterics share similarities to nematics as implied by the name chiral nematics; on the other hand, cholesterics behave like smectics because of the layered structure and mechanical instability[1], except that structures of defects are different. The helical structure with 2π rotating periodical length called *pitch P* gives rise to a Bragg reflection that selectively reflects light forming a bandgap as shown in Fig. 1.5. Only circularly polarized light with the same handedness as cholesterics will be reflected, as a result, at least 50% of non-polarized light is transmitted[43, 44]. The edge wavelengths λ_o and λ_e of the bandgap are determined by ordinary μ_o and extraordinary μ_e refractive indices and pitch *P* of LCs with normal incidence,

$$\lambda_o = \mu_o P,\ \lambda_e = \mu_e P, \tag{1.3}$$

Therefore, LCs with higher birefringence or larger pitch produce a wider bandgap. This allows the bandgap to be tuned by changing pitch through external stimuli with a certain LC. Some common methods, such as electric field[45, 46], magnetic field[47-49], light[50, 51],

doping[52, 53], temperature[54-56] or stress[57, 58] have been applied to tune the bandgap over the range from infrared wavelength to ultraviolet wavelength[59].

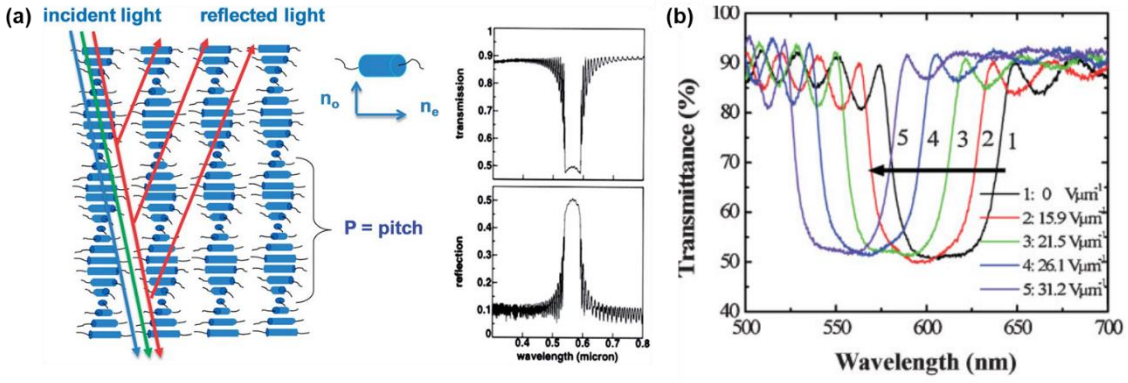

Figure 1.5 Tuneable selective reflection of cholesterics. (a) Bragg reflection forming bandgap with 50% reflection, n_0 and n_e are ordinary and extraordinary refractive indexes respectively, the figure is adapted from reference[44]. (b) Tuneable selective transmittance as a function of wavelength with electric fields, the figure is adapted from reference[60].

1.2.2 Applications

This unique bandgap characteristic, sensitive to external stimuli, opens up many possibilities for commercial application. For example, cholesterics, especially polymer-stabilized cholesteric[61], are used in displays with no power supply because they keep the static image without power. The temperature-responsive property makes cholesteric phase a good candidate for temperature sensors such as fever thermometers[62] or smart windows[63]. Especially in summer, heat increases the cholesteric pitch in the smart window that reflects redundant infrared wavelength at high temperature, but when the temperature cools down that decreases pitch allowing infrared wavelength to go through heating up the house. Additionally, cholesterics are used as colour filters[64] or for pumping the laser through bandedges[65].

1.3 Surface anchoring

1.3.1 Extrapolation length

When LCs are close to a surface, van der Waals forces attract LC molecules forming epitaxial layers of molecules[66-69], similar to the way in which a charged surface develops a Helmholtz layer and adjacent Debye layer[18, 70]. If the surface is also anisotropic, such as in muscovite mica or gypsum, usually there exists one or a few preferential positions called *easy axes* that anchor molecules, which minimizes free energy[2], shown in Fig. 1.6 for the nematics. The energy that prevents the molecules from moving from the easy axis to a certain position is called *anchoring energy*. In Fig. 1.6a, δ_0 and δ_D are deviation angles to the *z* axis on wall 1 and wall 2 respectively,

$$\frac{\partial}{\partial y}\delta = \frac{\delta_D - \delta_0}{D} \tag{1.4}$$

where δ_D is the fixed angle, D is the distance between wall 1 and wall 2, y is the axis perpendicular to the wall. Then this function can be plotted with δ as a function of y, therefore the extrapolation length L on the intercept of the y axis is obtained. The extrapolation length corresponds to the virtual depth inside the substrate where the molecule follows the easy axis, which is added up to the effective distance in free energy calculation[71]. By minimizing bulk energy and surface energy,

$$L = \frac{K_{2\ 2}}{W} \tag{1.5}$$

where $K_{2\ 2}$ is twist elastic constant, and W is anchoring strength, anchoring energy coefficient. There are three principal types of anchoring, namely planar (tangential), conical (conic) and homeotropic (perpendicular) anchoring. For planar anchoring with

one easy axis, the anchoring is known as homogeneous (non-degenerate) planar anchoring. With multiple axes, degenerate planar anchoring occurs. Conical anchoring is tilted anchoring between planar and homeotropic anchoring.

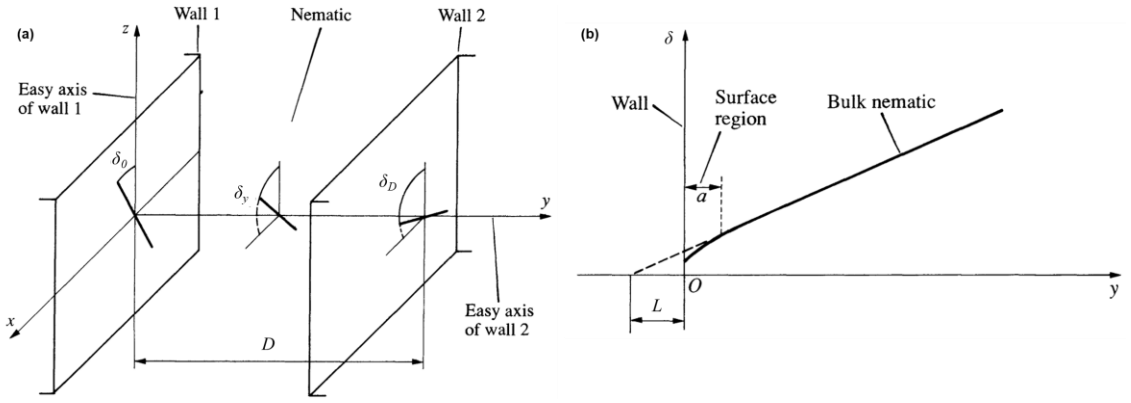

Figure 1.6 Schematic diagram of extrapolation length, figures are adapted from reference[2]. (a) Configuration of nematic LCs distributing between two walls at a distance *D* apart, δ_0, δ_y and δ_D are deviation angles from the easy axis of wall1 at distance $y = 0$, y and D respectively. (b) Deviation angle δ as a function of distance y, a is the distance within which molecules are affected by the wall, L is extrapolation length.

In section 1.1.4, it has been shown that position of defects around a particle or between wedge is related to the type of anchoring, anchoring strength, Frank elastic constant and radius of the particle. Here extrapolation length L in equation 1.5 is used to characterize the interaction between LCs and particles. If the particle radius is much smaller than the extrapolation length, there is no defect around the particle, which is the case with the thin disk mentioned above. If the particle radius is larger than extrapolation length, the competition of elastic energy with different elastic constants and anchoring energy leads to different defects, which could be understood by topological theory[26].

1.3.2 Anchoring energy

Anchoring energy sometimes is ambiguously referred to surface energy or adhesion energy[70] that describes the interaction of an isotropic liquid with the surface. Since there exists easy axis minimizing free energy, the surface energy G_s must have an anisotropic part[70, 72-74] that depends on the polar angle θ_0 and azimuthal angle φ_0 of molecules at the easy axis,

$$G_s = G_s(\theta_0, \varphi_0) + W(\theta - \theta_0, \varphi - \varphi_0) \tag{1.6}$$

where $G_s(\theta_0, \varphi_0)$ is the free energy function at the easy axis, $W(\theta - \theta_0, \varphi - \varphi_0)$ is a function that describes anchoring strength at deviated polar angle θ and azimuthal angle φ, W is anchoring strength. If only polar anchoring of free energy $G_s(\theta)$ is considered and neglect the higher-order terms in Taylor expansion for non-ferroelectric LCs[74],

$$G_s(\theta) = W_0 + W_p \text{ c } \text{o}^2 \text{s}\theta \tag{1.7}$$

where W_p is polar anchoring coefficient or polar anchoring strength, W_0 is a coefficient that is not related to angle. Generally, the anchoring potential[75] is given,

$$G_s(\theta) = -\frac{1}{2} W(\mathbf{n} \cdot \mathbf{n}_0)^2 \tag{1.8}$$

where $\mathbf{n}$ and $\mathbf{n}_0$ are the unit directors on the deviated position and easy axis respectively.

Usually, the strong anchoring strength W is estimated by de Gennes' dimensional argument assuming that extrapolation length b is equal to the molecular dimension a_m, namely $\frac{K}{b} = \frac{K}{a_m} = 1\ 0^3 - 1\ 0^2$ J/m^2, where K is elastic constant[2, 71, 72]. But for experimental measurements, the polar anchoring strength W_p is in the range $1\ 0^7 - 1\ 0^3$ J/m^2 and the azimuthal anchoring strength W_a is one or two orders lower[72]. Strong

anchoring exists on freshly cleaved crystalline surfaces[2, 73, 76] such as mica on which 4-Cyano-4'-pentylbiphenyl (5CB) molecules are parallel to the surface.

It has been shown that computational chemistry is able to predict the anchoring status of molecules on certain surfaces by taking into account the energy interaction of surface, molecules and the water adsorption based on first-principles calculations[77, 78]. This method provides a rational way to design and predict the anchoring status and strength, which opens up lots of possibilities on AI-assisted experiments[79].

1.4 Liquid crystals in constraints

In a broad sense, constraints could be more than just small geometry, for instance, constraints can include surface adsorption of molecules or direction control of molecules by external fields. It has been shown that epitaxial growth of molecules on surfaces resulting in structural forces is ubiquitous whether it is confined by two plates or not[80, 81]. Further, confinement induced Saturn-ring defects[82] or focal conic defects[83] can be replicated with the application of external fields. Those methods share a common ground that aligns or commands orientation of LCs in a certain direction.

1.4.1 Surface alignment

There are several methods[84] to induce anchoring alignment on surfaces other than natural surface alignment. One of the most common and easiest ways to induce alignment with the surface is to rub the surface with a cloth in one direction that orders molecules in the same orientation. A widely accepted theory to explain this rubbing is that friction creates grooves[85-87] and the alignment along the grooves minimizes the distortion energy, similar to the concept of easy axis but in a geometric manner shown in Fig. 1.7a. However, if the

surface is equally rubbed in two dimensions causing roughness, those molecules tend to be perpendicular to surface avoiding elastic strain energy[85, 88]. Another way is to coat self-assembled monolayers to align molecules by epitaxial growth[89, 90] of LC layers on the top of it giving rise to homeotropic, conical or planar anchoring depending on the density[91], molecular structures or texture of the monolayer[92, 93], shown in Fig. 1.7b. This self-assembled monolayer could also be controlled by external stimuli, like temperature[94], light[95, 96], ion beam[92] or chemicals[97], to adjust the anchoring strength and orientation, which in turn can be used as a sensor to visualize external stimuli[98, 99]. Some chemicals even with extremely small amount can bring about anchoring transition[100] that is easily distinguishable by eyes. Additionally, oblique deposition of an evaporated layer could generate tilted conical anchoring[101].

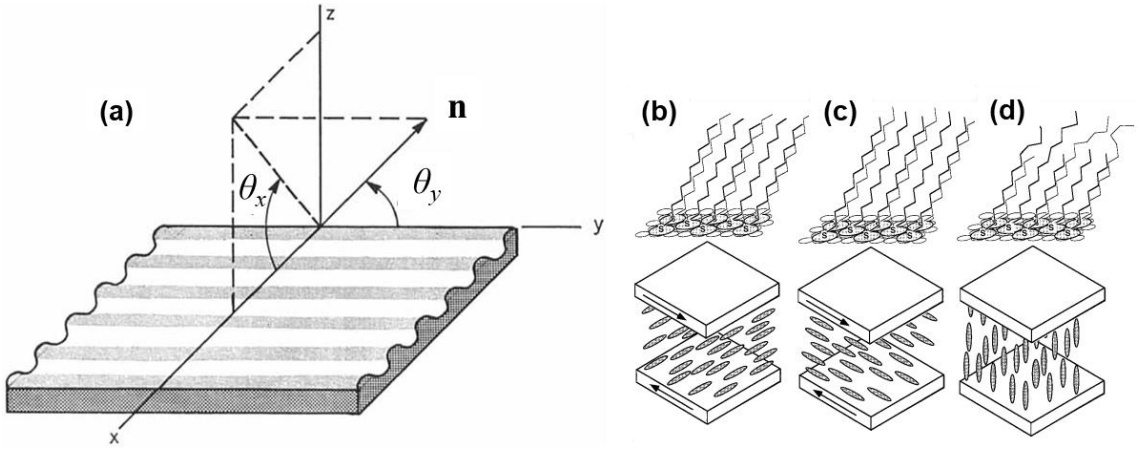

Figure 1.7 Mechanism of surface alignment. (a) Schematic diagram of rubbed grooved surface, **n** is molecular director, θ_x and θ_y are projecting angle of director on *x* and *y* axes respectively, the figure is adapted from reference[86]. (b-d) Configurations of self-assembled monolayers in top panels and corresponding LC alignments in bottom panels, figures are adapted from reference[93].

Bounded by the surface, not only the order parameter but also the nematic-isotropic transition temperature will be changed[17], shown in Fig. 1.8. With a weak surface energy

potential on semi-infinite surface, order parameter at the boundary is increasing but the transition temperature is still the same compared to the case without surface energy potential. With higher surface energy potential, both order parameter and transition temperature increase, at some point reaching critical surface energy potential, the transition becomes continuous from first order to second order.

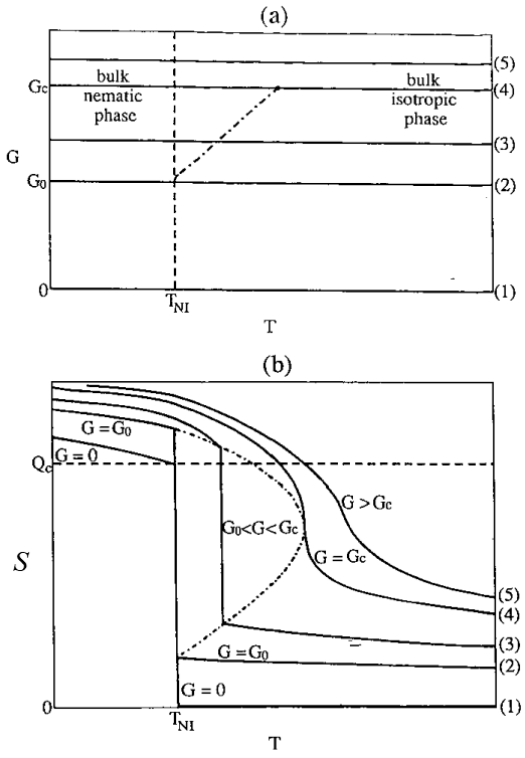

Figure 1.8 Boundary effect on order parameter and phase transition, the figure is adapted from reference[73]. (a) Nematic-isotropic (N-I) phase transition as a function of surface energy potential G and temperature T, the dashed line is the transition temperature T_{NI} without surface energy potential, the dot-dash line is the transition temperature at certain surface energy potential G. (b) Order parameter S as a function of temperature T with 5 surface energy potentials G as (a). G_0 is maximum potential that does not change the transition temperature, G_c is critical potential that vanishes the first-order transition, dashed line is critical order parameter S_c during N-I phase transition without surface energy potential, the centre line is critical order parameter during N-I and I-N phase transitions with various surface energy potential.

Furthermore, boundary effects, such as boundary fluctuation, have been found to add intriguing phenomena, namely sub-diffusion and super-diffusion[102], to the already complicated anisotropic diffusion[103-106] that is a result of competition between elastic stress and defects around particle both in nematics and cholesterics. How exactly surface chemistry plays a role on LC behaviours is still an open question, especially on a molecule level[107].

1.4.2 Liquid crystals in confined geometry

LCs have been confined in different geometries which can be classified into plates, spheres, tubes or combined complex geometries, such as fractal[108] or porous structures[109].

The same study as Fig. 1.8 also considered the order parameter and phase transition temperature as a function of confined thickness between two parallel plates, where stronger confinement with small thickness shifts both bulk and boundary transitions to higher temperatures, finally reaching second-order transitions[17]. However, the bulk transition that is less affected by confinement than boundary transition, makes the boundary transition disappear at certain distance confinement. The author[17] calculated that for typical LCs, below 200 nm confinement with anchoring energy 0.15 mJ/m^2, which is close to the upper range of common anchoring, would be able to see continuous phase transition. These predictions were proved firstly in thin-film and droplet confinement witnessing an increase of phase transition temperature[110] and continuous paranematic transition[111] respectively, also by a more recent experiment done in silica tubes which showed second-order transition[112]. It would still be interesting to see if the boundary layer will melt into the bulk transition.

With spherical confinements, such as droplets[113], tactoids[114] or shells[113, 115], more morphologies[116] than defect configurations around particle with nematics have been seen under the competition of sphere radius, elastic constants and anchoring energy, shown in Fig. 1.9. Besides, controllable frustrated structures were also seen in the droplet shells[117, 118]. Moreover, cholesteric defects also self-assemble into different screw dislocations in droplet confinement depending on anchoring and diameter of droplet[119-121], which has been used for laser[122].

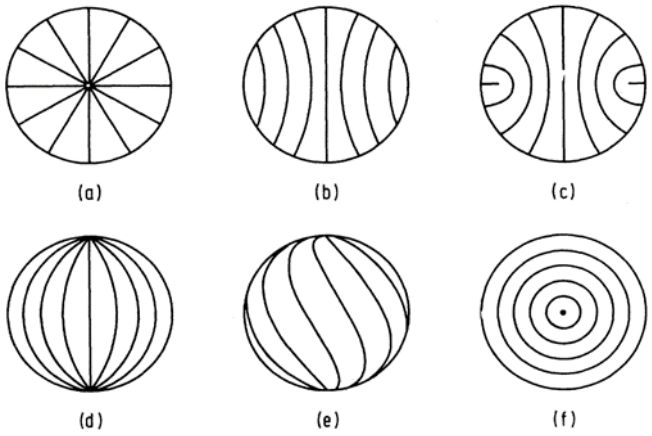

Figure 1.9 Nematic configurations in droplets, the figure is adapted from reference[116]. (a-c) Morphologies with homeotropic anchoring. (d-f) Morphologies with planar anchoring.

1.4.3 Magnetic and electric responses

1.4.3.1 Fréedericksz transition

LCs are responsive to magnetic and electric fields due to their diamagnetic and dielectric anisotropies which are very important in display applications switched by external fields. Particularly, when a nematic is confined between two plates with strong anchoring, the competition between elastic energy and electric fields (or magnetic field) results in a threshold voltage that distorts molecule orientation, which is called Fréedericksz

transition[123]. Taking the twist case with nematics distorted by the electric field as an example, where *x, y* coordinate system lies in the plane containing plate, the *z* axis is perpendicular with plate, the easy axis of planar anchoring is parallel with the *x* axis, the electric field is parallel with *y*, and the angle between the director of molecules and *x* axis is φ, then the free energy density G_d is calculated by twist elastic energy and electric energy[2],

$$G_d = \frac{1}{2}K_{22}\left(\frac{d\varphi}{dz}\right)^2 - \frac{1}{2}\varepsilon_0\Delta\varepsilon E^2 \sin^2\varphi \tag{1.9}$$

where K_{22} is twist elastic constant, ε_0 is the dielectric constant of vacuum, $\Delta\varepsilon$ is the dielectric anisotropy of LCs, and E is electric field strength. By minimizing free energy with respect to φ, a critical field E_c is obtained,

$$E_c = \frac{\pi}{d}\sqrt{\frac{K_{22}}{\varepsilon_0\Delta\varepsilon}} \tag{1.10}$$

$$V_c = \pi\sqrt{\frac{K_{22}}{\varepsilon_0\Delta\varepsilon}} \tag{1.11}$$

where d is sample thickness, and V_c is the critical voltage threshold which is typically a few volts independent of sample thickness. This critical voltage only orients the middle plane of the sample. With increasing voltage, also the molecules close to the wall will gradually be oriented[124]. Usually, inevitable ionic impurities in LCs will move along the electric field, creating a counter-field that compensates the effective voltage. As a result, AC fields at frequency 50 or 60 Hz are commonly applied in the display to suppress the ion mobility[125].

For a magnetic field, the magnetic threshold H_c is very similar to the electric threshold,

$$H_c = \frac{\pi}{d}\sqrt{\frac{K_2}{\Delta\chi}} \quad (1.12)$$

where $\Delta\chi$ is the diamagnetic anisotropy.

The Fréedericksz transition also applies to distortions related to other elastic constants, which provides a method to measure elastic constants or dielectric/diamagnetic difference of LCs. It should be noted that this calculation only applies to strong anchoring[2, 74], or else, the anchoring energy, such as the Rapini-Papoular potential, needs to be taken into account, which will lead to, for electric case threshold field E_c, which is thickness-dependent since the extrapolation length changes effective thickness of elastic energy, rather than threshold voltage[74]. Sometimes the pretransitional epitaxial boundary layer will also change the effective sample thickness thus changing critical voltage[126].

1.4.3.2 Cholesteric-nematic unwinding

For cholesterics confined between two plates, the application of magnetic or electric fields parallel with the plates gives rise to an interesting phenomenon called cholesteric-nematic unwinding, which was predicted independently by P. G. de Gennes[2] and R. Meyer[47], then proved in several studies[45, 48, 49, 127], shown in Fig. 1.10. The threshold electric field E_c and threshold magnetic field H_c are calculated below considering competition of twist elastic energy and field,

$$E_c = \frac{\pi^2}{P_0}\sqrt{\frac{K_2}{\varepsilon_0\Delta\varepsilon}} \quad (1.13)$$

$$H_c = \frac{\pi^2}{P_0}\sqrt{\frac{K_2}{\Delta\chi}} \quad (1.14)$$

where P_0 is original cholesteric pitch.

Fig. 1.10a,c shows normalized pitch as a function of normalized magnetic field and

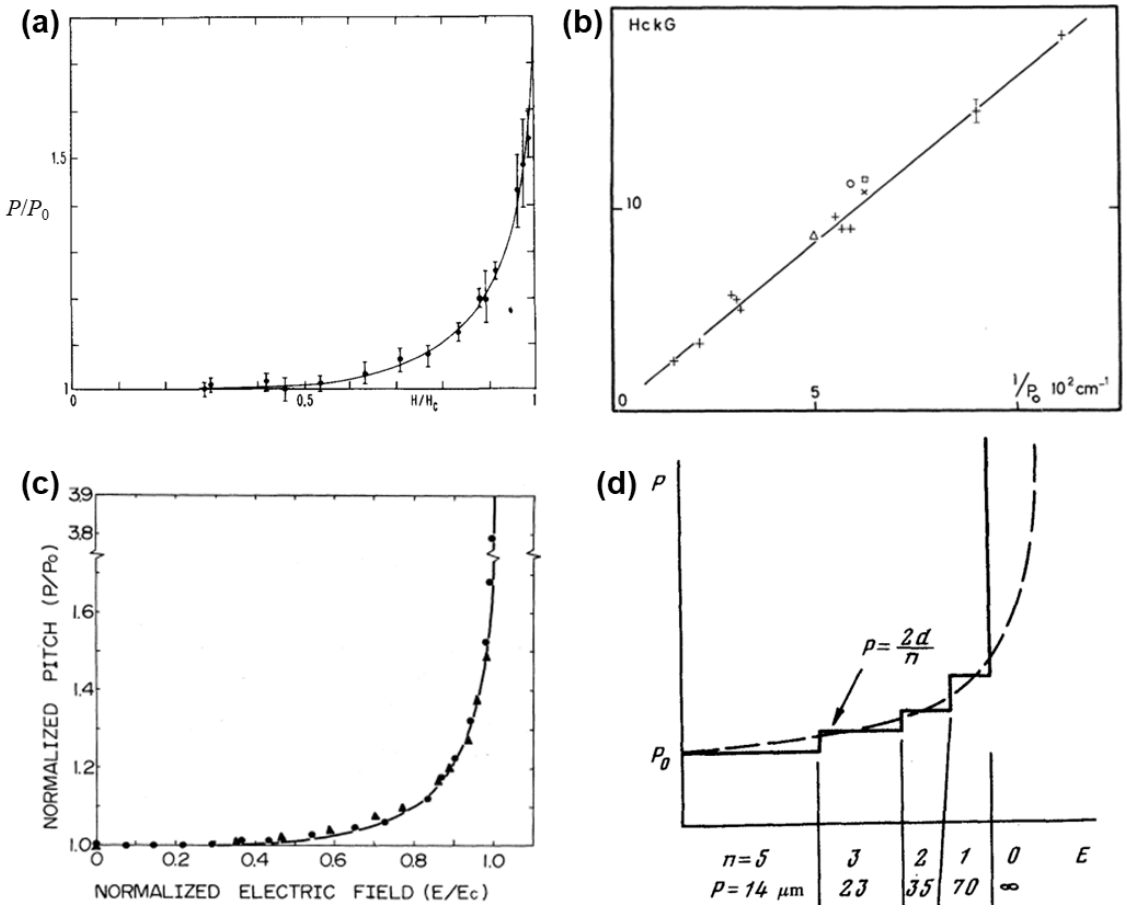

Figure 1.10 Magnetic and electric responses of cholesterics under spherical Grandjean-Cano wedge. (a) Normalized pitch by original pitch P/P_0 as a function of the normalized magnetic field by critical field H/H_c for cholesteric-nematic transition, the solid line is a theoretical calculation, the figure is adapted from reference[48]. (b) Critical field H_c as a function of inverse pitch $1/P_0$, solid line is a theoretical calculation, the figure is adapted from reference[49]. (c) Normalized pitch by the original pitch P/P_0 as a function of the normalized electric field by critical field E/E_c for cholesteric-nematic transition, the solid line is a theoretical calculation, the figure is adapted from reference[45]. (d) Pitch $P = 2d/n$ as a function of electric field E, d is surface separation, n is the number of half-pitch, the dashed line is a theoretical calculation, the figure is adapted from reference[128].

electric field respectively, which is in agreement with the prediction[2, 45, 48]. Fig. 1.10b confirms the inversed proportion between critical magnetic threshold and pitch[49].

However, R. Meyer[47] also discussed that strong boundary conditions may maintain the helix depending on the competition between twist and bend elastic constants until the field threshold is reached. Some other studies[128-134] argued that the prediction by P. G. de Gennes was based on the bulk transition that is free from the influence of boundary. If the anchoring condition is taken into account under confinement, discontinuous stepwise (sometimes called stick-slip) unwinding or winding will happen as predicted by different studies[57, 135-140] induced by external stimuli, such as temperature, magnetic and electric field, light, stress. Particularly, a recent paper[141] reported that if the easy axis of one surface can be rotated in a certain direction on one surface, the cholesterics would be in three possible different regimes from the free rotation to stick-slip or winding balanced by surface torque[137, 141-144] depending on the anchoring strength. Some evidences[128, 145, 146] about this discontinuous transition have been reported, for example, step unwinding[128] by electric field shown in Fig. 1.10d.

1.5 Scope of thesis

LCs show lots of optical and mechanical behaviours that not only share similarities with liquids and crystals, but also reveal unique characteristics which are subtly balanced by anchoring strength, elastic constants and confinement. Although tremendous research has been done in different confined geometries, it is still very intriguing to see how far we can perform self-assembly with LC elasticities despite its recent progresses[26], and how much the surface chemistry can affect bulk system[107].

Originally this thesis aimed at using a unique technique, the Surface Forces Apparatus (SFA), which can simultaneously and precisely measure optics and mechanics at the nanoscale, to study the optical and frictional properties of LCs under the

nanoconfinement. At the nanoscale, the epitaxial molecular layers are strongly affected by surface energy, but may still be controllable by electric fields, which will help the fundamental understanding of molecular properties at the extreme confinement, and have the potential of applications on the lubrication in Micro Electro Mechanical Systems (MEMS) or nanofluidics. The difficulty of the project is the application of large voltage drop across atomically smooth surfaces that anchor LCs, which has not been achievable by either rough indium tin oxide (ITO) substrates or insulated mica surfaces that are commonly used in SFA. Recently, Prof. S. Perkin group at the University of Oxford developed the Graphene Surface Force Balance (GSFB)[147] that possesses conductive and atomically smooth graphene surfaces, which makes the project possible. However, during collaboration, it turned out that the delicate preparation of graphene surfaces takes too much time, which is difficult for experimental tests.

Fortunately, a side project, initialized at the University of Calabria with 16 months collaboration in Prof. S. Perkin group, aiming at measuring equilibrium forces of cholesterics during twist transitions have been going well. The SFA is used to probe the competition of anchoring, elasticity and confinement with cholesterics subjected to muscovite mica surfaces that impose strong anchoring. It was found that rich morphologies including three regimes, constrained, stick-slip and sliding-slip, transform during the time evolution of the surface anchoring in the mechanical winding of cholesterics, which clarifies the long-term debate about the anchoring effect on cholesteric-nematic unwinding. The features of twist transitions are well captured by the 4x4 matrix simulation, and the mechanical windings are expounded with the frictional surface torque and fracture mechanics.

Following thesis starts with recent advances of LCs confined in the SFA and experimental setup from Chapter 2, followed by the analysis of multiple-beam interferometry obtained from SFA with emphasis on optical simulation in Chapter 3. Chapter 4 shows twist transitions and equilibrium forces in cholesterics during the surface separation. Chapter 5 shows three-regime forces emerging stick-slip winding mediated by anchoring strength during the compression of the surface. Finally, conclusions and outlook will be summed up as closing remarks in Chapter 6.

2 Background and experimental methods

2.1 Surface Forces Apparatus

2.1.1 This work

The Surface Forces Apparatus (SFA) was developed by J. N. Israelachvili and G. E. Adams[148] from a prototype which was invented in University of Cambridge by D. Tabor for surface force measurement[149, 150]. It is based on multiple-beam interferometry (MBI) that generates "Fringes of Equal Chromatic Order" (FECO) on a spectrometer to measure the distance between two surfaces, shown in Fig. 2.1a. The precision of the distance measurement is 0.1 nm (accuracy ~ 0.5-1.0 nm) and the force experienced by the surface based on the spring system can be calculated with a typical sensitivity of 0.1 μN. With such precision, SFA has been widely used to detect surface forces[18] generated by van der Waals forces, electrostatic and hydrophobic interactions, frictional or other structural forces in a medium.

The optics of the SFA are shown in Fig. 2.1a, where collimated white light is reflected by a mirror to crossed cylinders in which FECO are formed before being transmitted thought prisms to a spectrometer then a camera. All the optical components are well aligned to make sure vertical incidence through cylinders, which have typical radius 1-2 cm. Those cylinders are in the form of glass lenses with a thin layer of glue over the cylindrical face. Onto the glue is stuck a silver-coated mica piece of uniform thickness, silver side down, resulting in a glass-glue-silver-mica layered structure. The two lenses are aligned in a crossed cylinder configuration with mica surfaces facing each other. The silver layers reflect more than 95 % of light[151] and only resonated rays of which optical

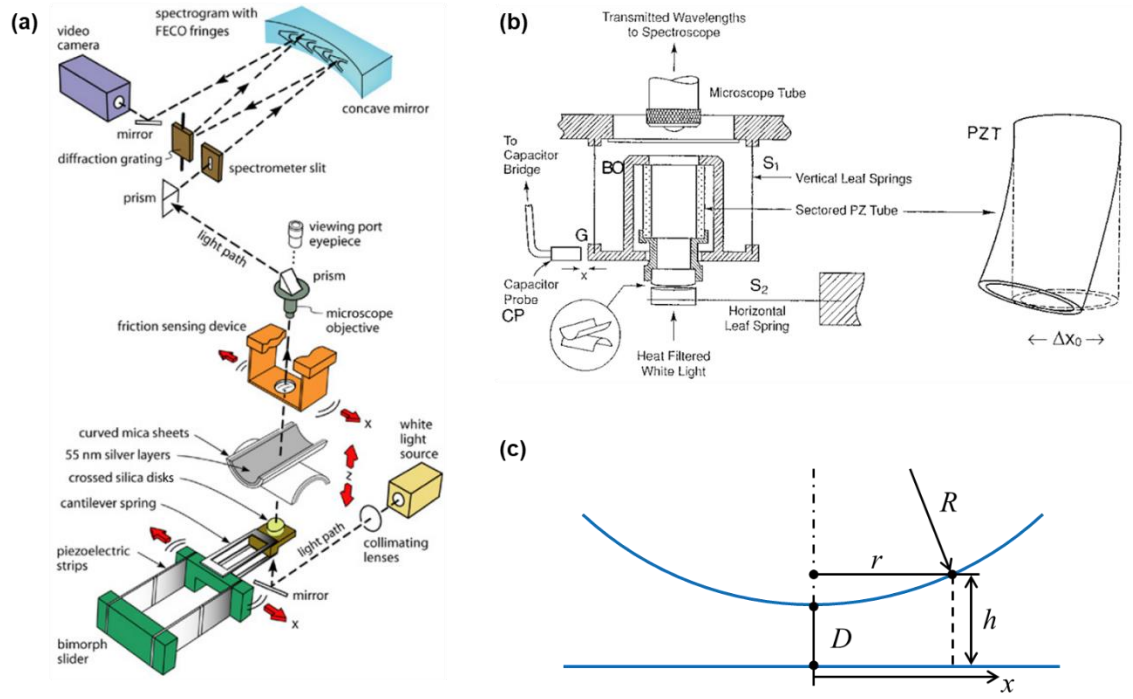

Figure 2.1 Schematic diagram of the SFA/SFB. (a) Optic setup of the SFA, the figure is adapted from reference[152]. (b) Top-mounted part of the SFB for piezo-controlled movement, the figure is adapted from reference[153]. (c) Approximate geometry of crossed cylinders with radius *R*, minimum distance *D*, lateral radius *r* at height *h*.

path length meets integer wavelength can be transmitted through silver layers, such that sharp fringes are obtained as shown in Fig. 2.2, similar to a Fabry-Pérot interferometer[124]. In order to reach a high resolution of thickness measurement, atomically smooth mica that is transparent and chemically inert is used[154]. Most importantly, mica is flexible and can be cleaved with a large and equal-thickness area.

2.1.1.1 The crossed-cylinder geometry

The confinement under geometry between two crossed cylinders with radius *R* is similar to the geometry of a sphere with radius *R* approaching a flat plate[18], shown in Fig. 2.1c,

when the lateral radius *r* is much smaller than radius *R*, which is the typical working distance in the SFA. This approximate geometry is described as,

$$h = D + \frac{r^2}{2R} \tag{2.1}$$

where *h* is certain height of confinement, corresponding to lateral radius *r* from the point of minimum surface separation (i.e. *r* = 0 and *D* = *h*).

2.1.1.2 Fringes of equal chromatic order

Fringes of equal chromatic order emerging from the interferometer are shown in Fig. 2.2 where curved fringes are as a result of the spherical geometry, which is useful for determination of the radius of curvature *R*. At larger height *h*, longer wavelengths are satisfied with the same chromatic order, called *red shift*. Contact between the surfaces happens at *D* = 0 distance. Adhesion between the surfaces in contact leads to a flattening of the surfaces which is seen in Fig. 2.2a. By comparing wavelengths at *D* = 0 to those of known mercury lines, a calibration can be made to allow separation *D* to always be known. Usually flattening is due to the deformation of glue since its Young's modulus is smaller than mica[155], thus the thickness of mica is considered as unchanged. When the surfaces are separated with distance *D*, this distance can be calculated with following equation[151] by calculating the propagation of light in mica and medium between two sliver layers,

$$\tan(2\pi\mu D/\lambda_n^D) = \frac{2\bar{\mu}\sin[\pi(1-\lambda_n^0/\lambda_n^D)/(1-\lambda_n^0/\lambda_{n-1}^0)]}{(1+\bar{\mu}^2)\cos[\pi(1-\lambda_n^0/\lambda_n^D)/(1-\lambda_n^0/\lambda_{n-1}^0)]\pm(\bar{\mu}^2-1)} \tag{2.2}$$

where μ is the refractive index of the medium, λ_n^0 and λ_{n-1}^0 are wavelengths of the n^{th} and n-1$^{\text{th}}$ fringes at *D* = 0 respectively, while λ_n^D is the n^{th} fringe at distance *D*, $\bar{\mu} = \mu_{mica}/\mu$, μ_{mica} is the average refractive index of mica. The sign $\pm$ is positive for fringes with odd

fringes and negative for even fringes, which explains the observed difference in odd and even fringes. If λ_n^D moves to the position of λ_{n-1}^0, namely $\lambda_n^D = \lambda_{n-1}^0$, right the hand side of equation 2.2 is 0, therefore, $D = {\lambda_{n-1}^0}/{2\mu}$ which provides a simple way to estimate the distance that the surface moves.

In Fig. 2.2, each fringe splits into a doublet which is due to birefringence and the relative intersection angle Ψ between the index axes of the two mica surfaces. The two polarizations β and γ in the doublet experience ordinary μ_β and extraordinary μ_γ refractive index of mica respectively, which produce different optical paths. More details about splitting, shape and parity of fringes will be discussed in section 2.2.1 and section C.

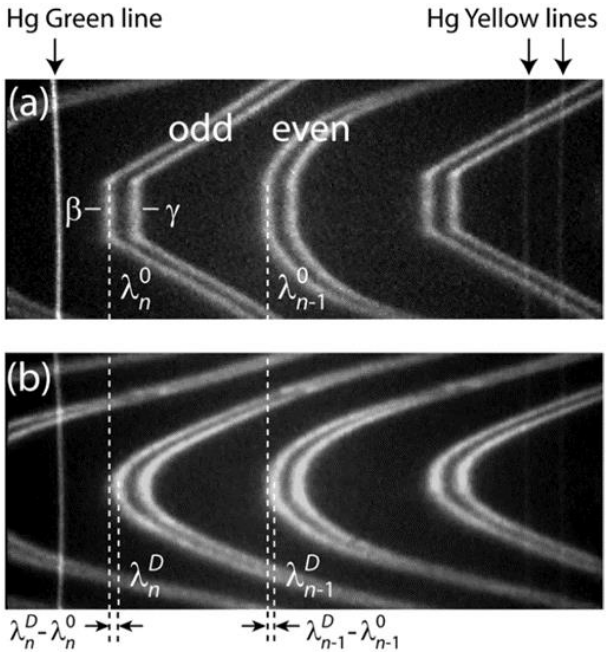

Figure 2.2 FECO and mercury lines by the SFA, the figure is adapted from reference[152]. (a) Fringes, Hg green line and yellow lines at contact position in the air, β and γ rays experience refractive index of brownish mica μ_β and μ_γ respectively, λ_n^0 and λ_{n-1}^0 are n^{th} and n-1th β fringes at zero distance respectively. (b) Fringes at distance D. λ_n^D and λ_{n-1}^D are n^{th} and n-1th β fringes at distance D respectively. Dashed line indicates position of β fringe.

2.1.1.3 Normal force measurements

In a SFA the bottom surface is connected to a cantilever spring that is driven by a motor with controllable but constant speed. When the bottom surface experiences zero force $F(t) = 0$, the speed of surface deduced from the distance profile will be the same as that of the motor. When the surface speed is smaller than that of the motor, it means that surface encounters repulsive force $F(t) > 0$, otherwise, surface undergoes attractive force $F(t) < 0$. $F(t)$ can be calculated from the following equation,

$$F(t) = k(D(t) - D_0 + v\ t) \tag{2.3}$$

where *k* is spring constant, $D(t)$ is the instant distance at time *t*, D_0 is the initial distance where the motor starts to move, *v* is constant motor speed which is assumed positive during the surface approach. Although motor speed *v* is constant, its exact value of it is usually deduced from the measured distance profile based on the assumption that at a large distance no force is encountered. This is because motor speed depends not only on control voltage applied, but also on the position of thread, backlash or specific configuration of setup.

The force the surface encounters can be calculated by the Derjaguin approximation[18] at the working distance *D* much smaller than cylinder radius *R*, then the free energy per unit area *G* between two surfaces is known,

$$F = 2\pi\ R\ G \tag{2.4}$$

where $R = \sqrt{R_1 R_2}$. R_1 and R_2 are radiuses of two cylinders, which typically are the same value.

For shear motion, the SFA uses piezoelectric bimorph slider shown in Fig. 2.1a to induce lateral motion and the displacement of spring is detected by a laser beam during the experiment.

2.1.1.4 Surface Force Balance

Fig. 2.1b shows another version of the SFA, called Surface Force Balance (SFB) developed by J. Klein[156], which is also based on MBI to measure the distance and force. In its early development[156], mechanical components were simplified to allow easy assembly and enhanced cleanliness avoiding adsorption of molecules on the device. Later on, a piezoelectric tube was used to apply normal and lateral motion[153], and a capacitor probe was used to detect the signal of shear motion which could also indicate the purity of the liquid during normal motion, such that the resolution of shear force is 0.1 μN, comparable to typical SFA normal force measurement. The motion of the piezoelectric tube is very sensitive, but the speed and range of displacement are much smaller than movement by bimorph slider during shear measurements. Recently several advances of the SFB were made in S. Perkin's laboratory. In one experimental setup, graphene is coated on the surfaces to give electrodes for the application of electric fields[147]. In another, the set up includes 3 gold mirrors, which can be used to measure small surface separation for facile application of surface potential[157].

In this thesis, both the SFA and the SFB are used to carry out experiments for optics and mechanics of liquid crystals.

2.1.2 Further examples

More examples of the SFA will be discussed here to show the flexibility of customization for different requirements of experiments. The newest version SFA 2000[152] is designed

to be easily adjustable and customizable, including allowing for some attachments to increase sensitivity or surface velocity. Recently, a mini version of the SFA called μSFA[158] was designed based on the SFA 2000 to simultaneously measure distance and observe the sample under an inverted microscope, which broadens the application by taking advantage of fluorescent or Raman measurement.

X-ray has been adapted to replace white light for measuring orientation and structure of molecules for both static and dynamic conditions[159], which is very useful for the LC studies under confinement.

M. Heuberger used a fast spectral correlation[160] method, called extended surface forces apparatus, to extract *in situ* information, such as surface separation and refractive index, from fringes to improve precision over very long-range distance, which opens up possibilities to analyse the results while doing experiments. Following this, precise temperature control[161] and high-speed measurement[162] were developed.

Capacitor probes have been used to measure the distance and oscillating frequency[163] without any interferometry measurement that eliminates the need for optical tracking. This is very important for distinguishing the dissipation and equilibrium forces in a dynamic way[164], which is useful for the study of viscoelastic materials or opaque materials.

S. Granick developed a homebuilt simplified SFA[165] which focused on minimizing drift mechanics or temperature at the cost of reducing the precision. It has also been used to measure the dielectric property of liquids[166], for example, LCs with different orientations.

2.2 Past studies with liquid crystals confined in the SFA

2.2.1 Optics of liquid crystals in the SFA

As has been shown in Fig. 2.2, birefringence affects the splitting of fringes. With the injection of simple liquid, the optics will not be more complicated than that at contact, since a simple liquid has only a single refractive index. By contrast, LCs confined between mica add another birefringent layer and create a possible mismatch on optical alignment, resulting in intriguing phenomena and several puzzles, which generate lots of difficulties and hinder the further research on LCs using a SFA. This section will review some representative articles on optics of LCs in the SFA.

2.2.1.1 Phase retardation

The typical evolution of fringe splitting in LCs under planar anchoring with an increase of surface separation is shown in Fig. 2.3a, where splitting gradually increases at large distances[167], due to the birefringence of LCs that increases the optical path difference, called *phase retardation*. Although in reality, the optical axis from LCs may have a mismatch with the index axes of mica, which might be antagonistic with birefringence from mica, at a large distance the birefringence of LCs is dominant, regardless of the effect of intersection angle Ψ. When the intersection angle Ψ among layers is taken into account at a small distance, the optics is more complicated.

Firstly, mica-mica at contact position is examined with parallel and perpendicular intersection angle Ψ as shown in Fig. 2.3b, where a parallel configuration maximizes the splitting whilst a perpendicular one minimizes splitting resulting in singlet[168]. In a typical SFA setup, cleaved mica, of which three refractive indices α, β and γ form geometrical relationship called index ellipsoid, is with α refractive index axis almost perpendicular to the [001] crystalline cleavage plane[169]. This simplifies the analysis of mica birefringence

from biaxial to uniaxial crystal provided that white light is 90 ° incident to the surface, such that rays experiencing γ and β refractive index can also be called extraordinary and ordinary rays respectively. When mica γ axes are parallel to each other, the two mica pieces of equal thickness *T* are equivalent to a single layer of mica with double thickness 2*T*, which produces optical path difference or phase retardation R_t between two rays,

$$R_t = R_{t1} + R_{t2} = 4T(\mu_\gamma - \mu_\beta) = n(\lambda_\gamma - \lambda_\beta) \tag{2.5}$$

where R_{t1} and R_{t2} are phase retardation from first and second layers respectively, n is chromatic order, λ_γ and λ_β are wavelength generated by refractive index μ_γ and μ_β respectively. When mica γ axes are perpendicular to each other, the β ray from the first layer experiences a refractive index μ_γ in the second layer, therefore, the total phase retardation is $R_t = 0$ giving rise to a singlet. In the general case for all intersection angles, phase retardation R_t is given by the empirical equation[170, 171],

$$R_t = 4T(\mu_\gamma - \mu_\beta)\cos\Psi = n(\lambda_\gamma - \lambda_\beta) \tag{2.6}$$

where Ψ is the acute intersection angle between the longest index axes of two birefringent layers.

In the more general case of two different birefringent materials with different thicknesses, V. Kitaev and E. Kumacheva[168] introduced a concept named complex ellipsoid that is effective index ellipsoid a ray experience through two-layer crystals. This effective retardation is calculated by,

$$R_t = R_{t1}\cos 2\varepsilon + R_{t2}\cos 2(\Psi - \varepsilon) = n(\lambda_\gamma - \lambda_\beta) \tag{2.7}$$

$$\varepsilon = \frac{1}{2}\tan^{-1}\frac{\sin 2\Psi}{\cos 2\Psi + \frac{R_{t1}}{R_{t2}}} \tag{2.8}$$

where ε is the intersection angle between the complex ellipsoid and first-layer ellipsoid.

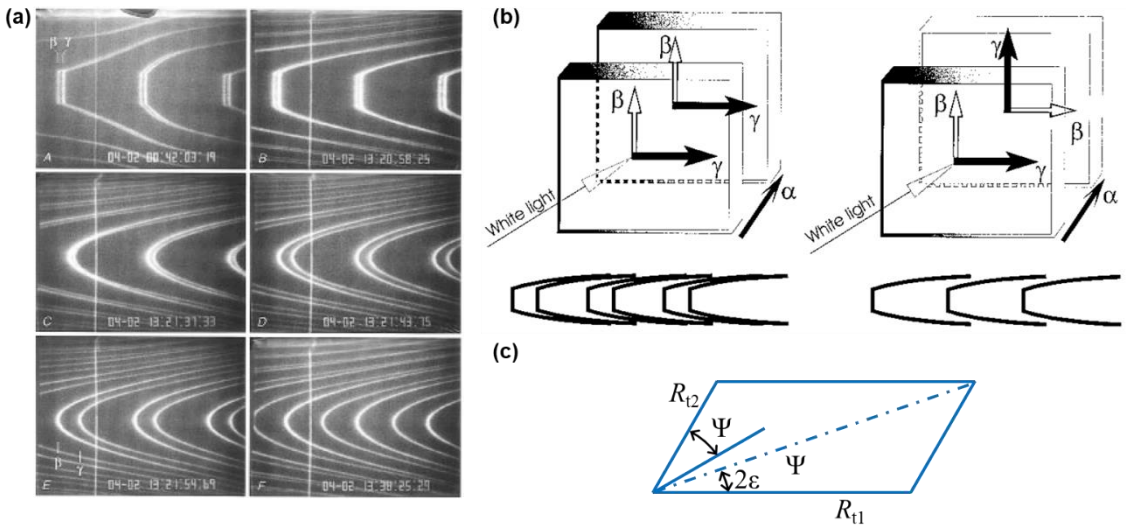

Figure 2.3 Optics of birefringent layers. (a) Snapshots of fringes of 8CB LCs with planar anchoring at various distances confined in the SFA, the figure is adapted from reference[167]. (A-F) Distance increases from 0 to 900 nm. (b) Parallel (left panel) and perpendicular (right panel) configurations of mica surfaces with equal thickness, and corresponding fringes, α, β and γ are index axes of mica, the figure is adapted from reference[168]. (c) Parallelogram rule of the effective index, or complex, ellipsoid. R_1 and R_2 are phase retardation or optical path difference of two layers of birefringent materials, Ψ is the acute intersection angle of two layers, ε is the intersection angle between complex ellipsoid and first layer R_1.

Equation 2.7 and 2.8 describe a parallelogram rule of effective phase retardation R_t calculated by phase retardation R_{t1} and R_{t2} with double intersection angle 2Ψ, additionally, ε is half the angle between diagonal of the parallelogram and first-layer ellipsoid, shown in Fig2.3c. This parallelogram rule is analogous to the composition of forces but with double intersection angle 2Ψ, which provides a simple geometrical way of understanding optics with LCs in the SFA. Ideally, with the above equations, multiple birefringent layers and LCs with twist angles can be analysed. Please note that this

equation is based on the assumption that silver coating is perfect mirror and phase change or dispersion between layers are negligible. This was confirmed in experiments which showed a reasonably good match with the theory[168].

2.2.1.1 Tuneable phase retardation

Rich phenomena were observed in the SFA by J. Klein *et al*[172, 173] shown in Fig. 2.4, due to the anchoring conditions of LCs on mica, namely the anchoring strength, alignments and transitions. With either parallel or perpendicular configurations of mica, three orientations of LCs were obtained, regardless of the exact twist angle of the LCs or the relative angle to mica. For the perpendicular configuration of mica shown in Fig. 2.4a, firstly, easy axes of anchoring on both mica surfaces are parallel which results in a planar orientation, where the mica birefringence is cancelled and the doublet of fringe is from phase retardation between the ordinary and extraordinary refractive index of the LCs, in addition, the surface experiences repulsive forces. Secondly, easy axes are twisted with a certain angle that was not indicated clearly in the paper, resulting in planar twisted orientation and only a singlet resulting from the average refractive index can be seen, with repulsive forces again, shown in Fig. 2.4a. In last orientation with mica exposed in air for a long time, some molecules like water in the air might absorb on surfaces, leading to homeotropic orientation and only a singlet experiencing the ordinary index is observed. In this case, attractive forces are measured near the contact position.

For the parallel configuration of mica, behaviours of optics are basically the same, except that fringes at contact are not singlet but doublet. In the paper, it is not clear how the alignment of mica was made, but from Fig. 2.4c planar and planar twisted orientations were observed in fresh parallel mica, one can suspect that one of the mica surfaces was

front-back flipped before silvering, a popular method that allows easy control for mica orientation[170].

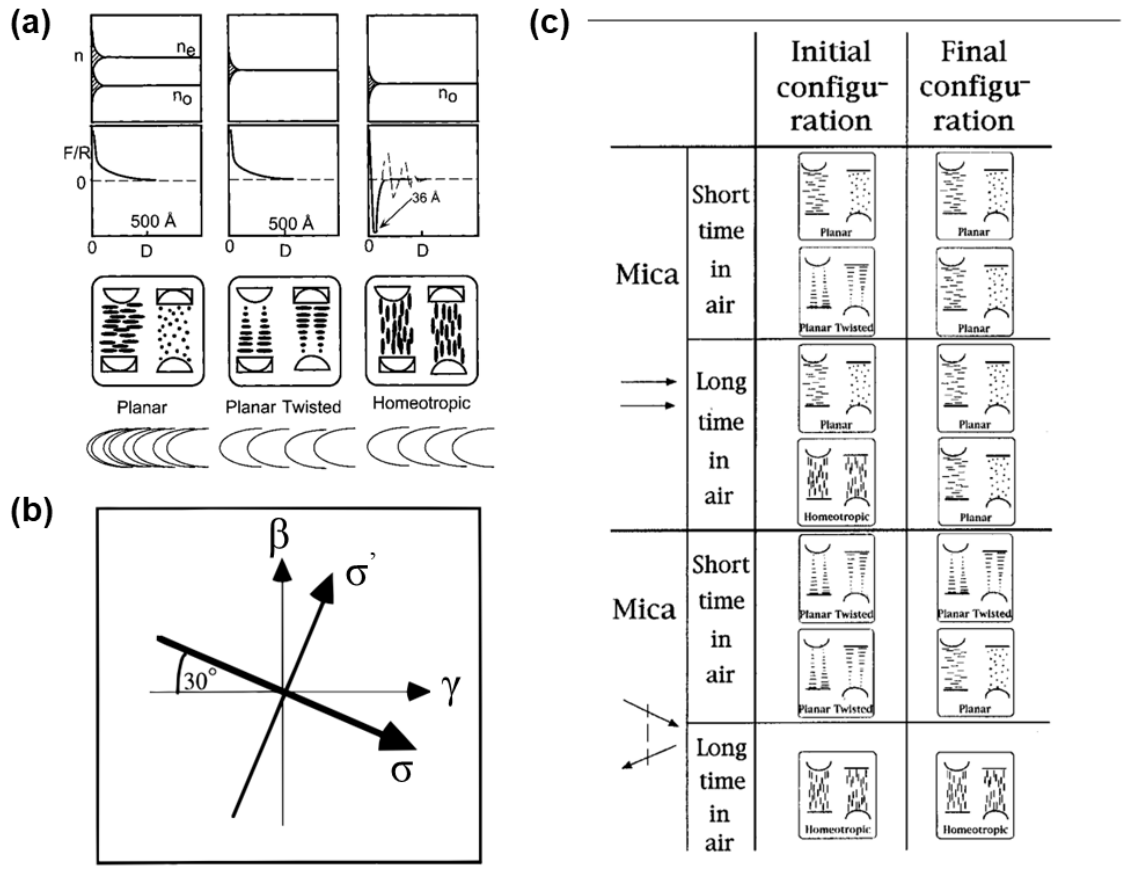

Figure 2.4 Anchoring transitions on mica. (a) Three anchoring configurations with mica surfaces perpendicular with each other, the figure is adapted from reference[173]. n_e and n_o are extraordinary and ordinary refractive indices respectively. *F*/*R* is the normalized force profile as a function of distance *D*. (b) Anchoring transition from the easy axis σ, which is 30 ° to the index axis γ, to σ' as a result of water adsorption, the figure is adapted from reference[172]. (c) Initial and final anchoring configurations during anchoring transitions for both parallel and perpendicular mica setups exposed either for a short or long time in the air, the figure is adapted from reference[172].

Some studies[76, 174] have shown that easy axes of LCs sit ±3 0° alternately to the index axis γ on different mica crystalline layers, and the adsorption of water or other molecules in the air will bring about the transition of the easy axis to a perpendicular direction,

shown in Fig. 2.4b as an example. Therefore, after a few days of the water adsorption, transitions between different orientations happened. However, the exact reasons how molecules distributed after transition were not clear. At that time, the camera was not available to take snapshots of fringes, and LC samples might not be well controlled or treated before experiments, thus it is difficult to interpret more about these intriguing results now. Nevertheless, this study shows the importance of surface chemistry and quality control of the sample. More details about LC pre-treatment for experiments done in this thesis will be shown in section 2.3.

When hybrid anchoring condition, one surface with planar against another with homeotropic anchoring, is applied, the fringe behaviours are even more complex. Such hybrid anchoring is expected to create a defect in the contact centre and induce a transition to planar configuration under strong confinement[175, 176] since the homeotropic anchoring strength is typically weaker than the planar one. During the transition, molecules rotate their orientation, changing the extraordinary refractive index and the relative angle to mica, thus changing the optics of the observed fringes, as shown in Fig. 2.5, where the curvature of the extraordinary fringe is negative at large distance $D \approx 6\ \mu m$, if that of the ordinary fringe is defined as convex and positive. Subsequently the curvature of the extraordinary fringe becomes zero then positive with decreasing of distance before surfaces are flattened at contact. During the whole transition, the extraordinary fringe is disturbed by thermal fluctuation induced index change[175], while the ordinary fringe is almost unchanged owing to the unchanged ordinary refractive index of index ellipsoid in a different orientation. Following this, the optics in surface retraction is mostly reversible.

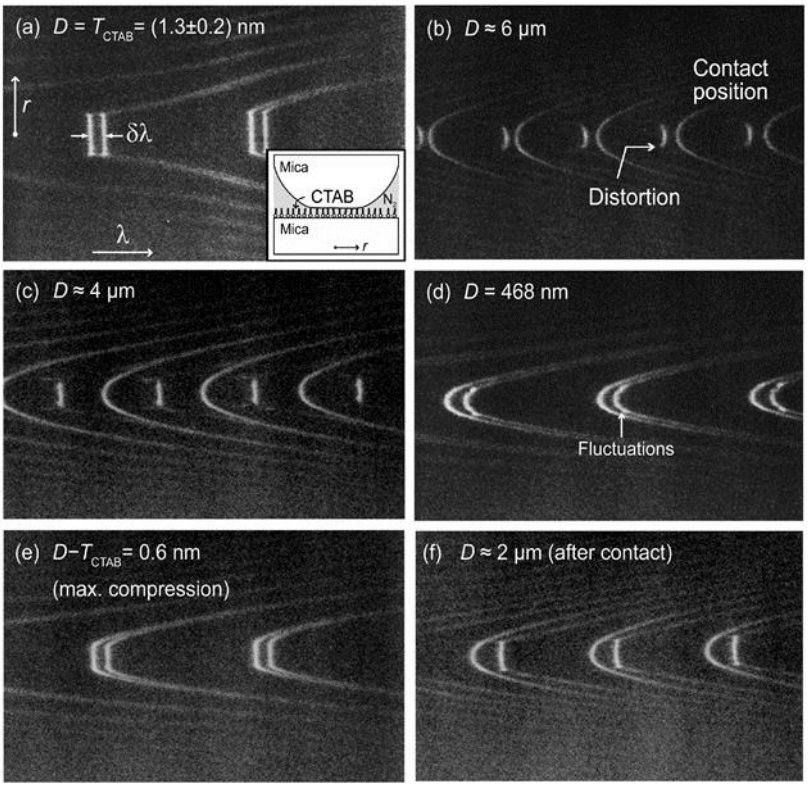

Figure 2.5 Snapshots of fringes of 5CB LCs under hybrid (planar-homeotropic) anchoring at various distances confined in the SFA, figure is adapted from reference[175]. (a) Mica-mica contact in N_2, surface separation $D = T_{CTAB} = 1.3 \pm 0.2\ nm$, T_{CTAB} is the thickness of the homeotropic coating Cetyltrimethyl Ammonium Bromide (CTAB), λ is the wavelength, r is the lateral radius with the contact point as the centre, δλ is the splitting of the doublet, inserted panel is crossed-cylinder setup. (b) Gradual approach from $D \approx 6\ \mu m$ (c) $D \approx 4\ \mu m$ (d) $D \approx 468\ nm$ (e) $D - T_{CTAB} = 0.6\ nm$ at maximum compression. (f) $D \approx 2\ \mu m$ after retraction from contact.

Engineering anchoring conditions provides a way to manipulate and control the optics of fringes, yet it is not that easy to tune the anchoring strength on mica. With the mature development of LC displays, the electro-optical response has been well understood[2], which is much simpler to adjust the orientation of molecules and design optics as needed. Fig. 2.6 shows how voltage, polarity and ions in LCs mediate the fringe behaviours[125]. With 5CB confined between silver layers avoiding birefringence of mica, smooth fringes corresponding to ordinary ray and jagged fringes representing extraordinary ray were

observed. The later fringes are similar to those fringes in hybrid anchoring, but still a bit different in terms of anchoring direction. The silver layer does not align LCs in a certain direction but rather in tilted random directions with multiple domains, shown in Fig. 2.6a, which also decreases Freedericksz threshold that is theoretically 0.8 V to 0.5 V. Slightly above Freedericksz transition, the extraordinary ray is shifted to shorter wavelengths across several ordinary rays towards the one with same chromatic order, without changing ordinary rays. Reversal of polarity of surface also suddenly shifted the position of the extraordinary ray to smaller wavelengths then relaxed back. During relaxation, the free ions in LCs played quite important roles that ions moved to opposite polarity compensating the voltage drop, such that molecules reoriented back to original position. In real experiments, if voltage drop is expected to be constant, higher frequencies are needed, for example, 50 or 60 Hz are quite typical in LC display. At higher voltage above 1.5 V, the convective movement of ions is even more drastic which leads to electrohydrodynamic instability that is circular or hexagonal domains, shown in Fig. 2.6e,f. Especially when the voltage is above 5 V, densely packed hexagons are formed across a broad view through a microscope or fringes, which is reminiscent of Rayleigh-Bénard convection[177] that is induced by temperature-mediated density gradient.

2.2.2 Mechanics of liquid crystals in the SFA

2.2.2.1 Normal forces of liquid crystals in the SFA

LCs possess both liquid and crystal properties leading to viscous and elastic responses respectively, which can be measured separately by the SFA[178, 179], in other words, the SFA is a unique tool for investigating not only optics but also viscous and elastic forces produced by LCs. With nematic LCs confined in the SFA, three types of structural forces

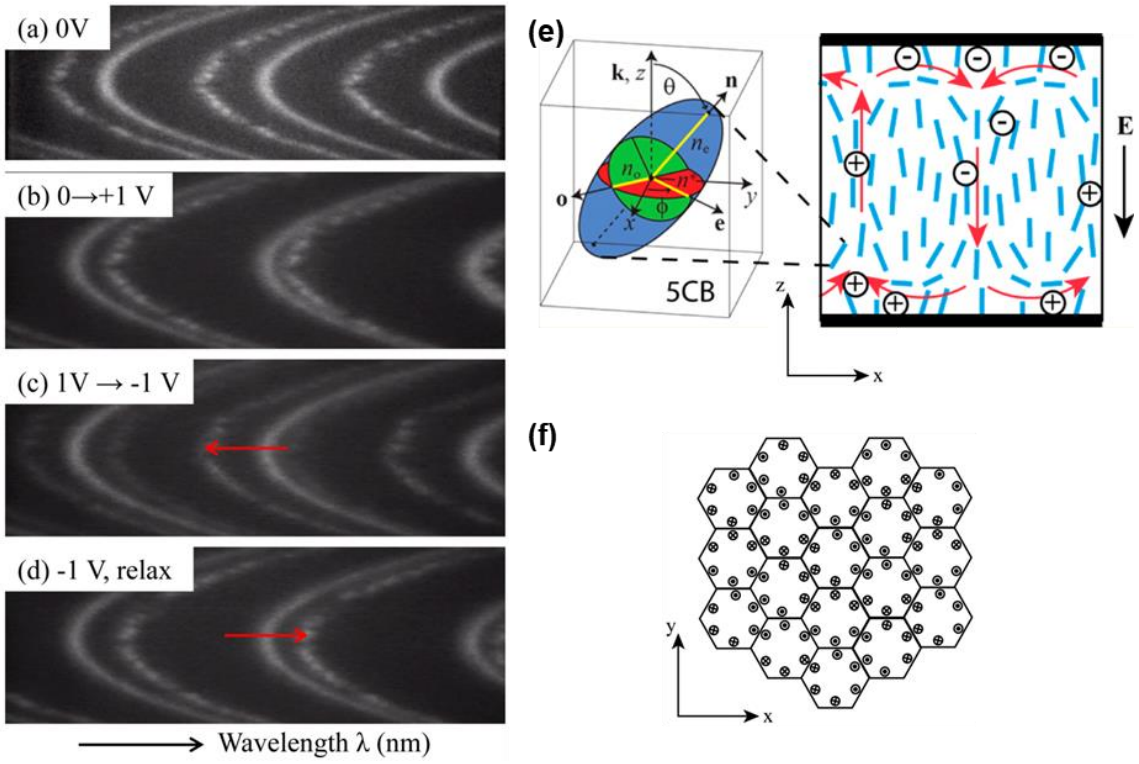

Figure 2.6 Electro-optical response of extraordinary fringe with 5CB, the figure is adapted from reference[125]. (a-d) Application of voltage from 0 to 1 then -1 V with 0.05 Hz at distance 7 μm. (e) Schematic diagram of the molecule and ion distribution on cross-section under high voltage, the inserted panel is a zoom-in ellipsoid of molecular director of 5CB. (f) Top view diagram of the hexagonal flow pattern and ion distribution under high voltage.

based on different ranges were typically measured and classified[178] during normal motion. It should be noted that long-range forces like Laplace pressure and surface tension on capillary bridge[178], which are not reproducible existing in background, will not be discussed here. Firstly, mismatch of easy axes for LC planar alignment between the two surfaces causes medium-range twist elastic forces. It has been shown in the last section that the easy axis on mica is $\pm 3\ 0^{\circ}$ with index axis γ and during assembly, it is easy to induce surface mismatch with a non-zero intersection angle Ψ. Twist elastic energy *G* per unit area is integrated from free energy density,

$$G = \int_0^D \frac{1}{2} K_{2\ 2} \left(\frac{\partial \Phi}{\partial\ D}\right)^2 d\ D = \frac{1}{2} K_{2\ 2} \frac{\Phi^2}{D} \quad (2.9)$$

$$F = 2\pi\ R\ G = \pi\ R\ K_{2\ 2} \frac{\Phi^2}{D} \quad (2.10)$$

where D is surface separation, $K_{2\ 2}$ is the Frank twist elastic constant of the LC, Φ is the twist angle of LCs, F is the force based on the Derjaguin approximation, R is the radius of the cylinder.

However, in real experiments, the measured forces were larger than expected, even when the twist angle is $\Phi = 0$, shown in Fig. 2.7a, due to unknown background force that is the second medium-range force detected in confined LCs 5CB. If this background force is considered after rotating the surface 15 °, the twist elastic force can be fitted very well with the model. However, the model does not fit the 33 ° rotation case, where untwist of LCs occurs at strong confinement, which adds another complication. This untwist remained during retraction until 830 nm where the twist was restored. Unfortunately, no snapshots or sample details were available for further analysis of this mystery now, but it seems reasonable given that surface chemistry and adsorption can affect the molecular configuration significantly, as has been shown in Fig. 2.4. Moreover, the authors also mentioned irreproducible results in different runs or experiments[178].

It is worth noting that this medium-range background force was also measured with homeotropic anchoring, where elastic forces from splay-bend contributions were negligible[178]. As for the mixed case with hybrid anchoring[180], it showed mainly splay-bend elastic forces and background forces shown in Fig. 2.7b, where forces decreased with successive runs.

This second medium-range structural force showing in the background was explained by an enhanced order parameter at small distances with both planar and homeotropic anchoring despite the twist, since it disappeared when the temperature was above nematic-isotropic transition, but the exact theory of this is still unclear.

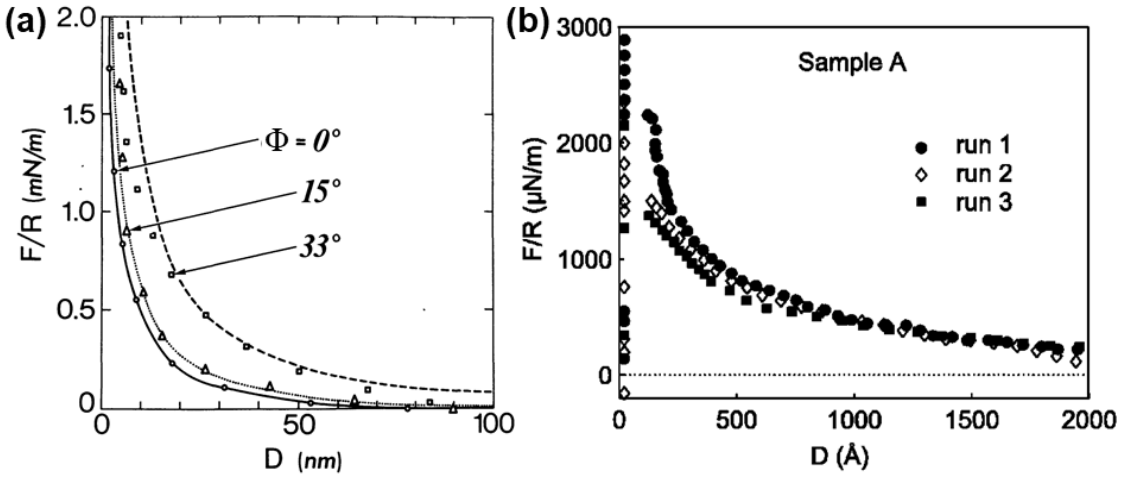

Figure 2.7 Medium-range forces measurement with 5CB LCs confined in the SFA. (a) Force *F* normalized by radius *R* as a function of distance *D* with different planar twist angle . Lines are theoretical calculation, the figure is adapted from reference[178]. (b) Force *F* normalized by radius *R* as a function of distance *D* with hybrid anchoring (Mica/5CB/CTAB) in different runs of sample A, the figure is adapted from reference[180].

Thirdly, short-range structural forces were found in confined 5CB, shown in Fig. 2.8, where periodically oscillatory forces were measured for surface separation of less than 15 nm, becoming more intense and well packed at a closer distance. For homeotropic anchoring, the oscillatory period is equal to the length of 5CB molecule 2.5 nm, which is reminiscent of smectic assembly, however, in planar anchoring, similar oscillation with a period 0.5 nm, equal to the width of 5CB was observed, meaning that this phenomenon is ubiquitous rather than particular to liquid-crystal phase assembly. The oscillatory decay is due to the adsorption or epitaxial growth of molecules on the surface interaction, which

was discussed in section 1.4. The decay length can be used to estimate the correlation length of molecular order, which has become a common measurement in the SFA or the Atomic Force Microscope (AFM) to probe the purity, self-assembly or friction of liquids on a surface. Nevertheless, this short-range structural force is very sensitive to surface and environment properties that vary even from run to run[178], depending on mica sheet, contact position, runs, humidity, working time and so on that might affect molecule ordering. Above anchoring experiments in section 2.2.1 are the best examples. If hybrid anchoring is applied, a plateau with constant force above 10 nm was observed[175] before going into normal 0.5 nm oscillatory period, shown in Fig. 2.8c. All these experiments again highlight the importance of sample preparation and experimental environment.

As for 8CB, both nematic and smectic phases[167] showed short-range structural forces that were similar to Fig. 2.8b with planar anchoring, except that the period of oscillations corresponded to the length of a molecular dimer were observed in the former phase and large background forces ascribed to permeation phenomena were observed in the later phase. With homeotropic anchoring, the structural forces observed in smectic 8CB was not short-range any more[167]. Instead, they extended very large separation due to the nature of smectic ordering, while the basic force behaviours were similar to those in Fig. 2.8a. Some interesting experiments regarding lamellar phases[181, 182] or smectic defects[183] shown below were performed to measure the interaction between layers during the squeezing out process.

Fig. 2.9 shows the force measurement of lyotropic multilamellar mesophases with

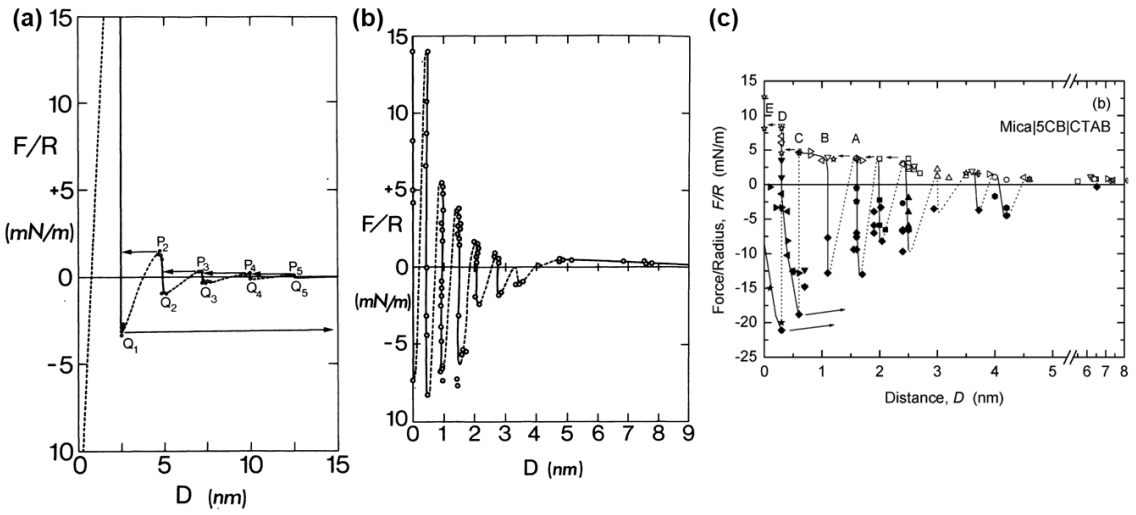

Figure 2.8 Short-range force F normalized by radius R as a function of distance D with 5CB LCs confined in the SFA. (a) Homeotropic anchoring, P and Q are instability points during approach and retraction respectively, the figure is adapted from reference[178]. (b) Planar anchoring, the figure is adapted from reference[178]. (c) Hybrid anchoring (Mica/5CB/CTAB), the figure is adapted from reference[175], A-E are jump points, open and filled points are data during approach and retraction respectively. Dashed lines are guided lines that are not measured by soft springs.

homeotropic anchoring to estimate modulus of layer compression B that is related to the interaction within membranes. This compression constant is calculated by,

$$B = d\left(\frac{\partial^2 G}{\partial D^2}\right)_n \tag{2.11}$$

where D is layer thickness, G is free energy per unit area and n is the number of layers per unit length. The compression constant B is determined by charge distribution, if the electrolyte concentration is large, screening length is small, resulting in undulation forces and $B \propto 1/D^3$; otherwise, $B \propto 1/D^2$ depending on electrostatic forces[182]. Under SFA confinement, the compression energy per unit area G is calculated by,

$$G = \frac{1}{2} B \frac{\Delta l_n^2}{l_n} \tag{2.12}$$

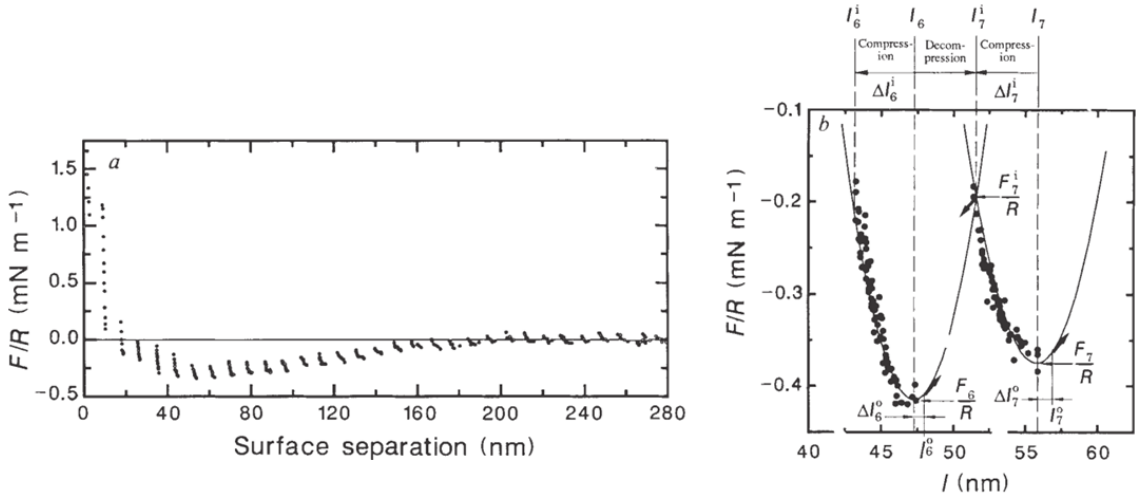

Figure 2.9 Forces measurement normalized by radius R with lyotropic lamellar mesophases confined in the SFA, the figure is adapted from reference[182]. (a) Force F as a function of surface separation with homeotropic anchoring. (b) 6th and 7th jump forces F as a function of surface separation l, dots are experimental data, and lines are theoretical calculations.

where $\Delta l_n = l_n - l$, l_n is the relaxed length of integral n layers, l is length after stretch or compression. This equation is very similar to equation 2.9, which is applicable to all layered systems, as long as compression modulus B is determined. The force experienced by the surface is calculated from the Derjaguin approximation[18] $F = 2\pi RG$, shown in Fig. 2.9a, where forces oscillate from long-range distance similar to the smectic ordering mentioned above and there is an long-range attractive background close to contact. This attractive background was explained by supressed-fluctuation-induced disjoining pressure[181] that is similar to effective attractive interaction in depletion effect caused by osmotic pressure in colloidal systems[184]. Alternatively, the integer-layered structures under crossed cylinders form dislocation defects between which compression and stretch regions exist, somehow causing attractive balance[182]. Apart from this attraction, the elastic force can be fitted with force generated by free energy as given in equation 2.2 with compression modulus B that is consistent with the value obtained from X-ray

scattering. This experiment opens up the possibility for direct measurement of compressibility and interaction of layered structures with high resolution.

Although in Fig. 2.9 the force behaviours can be explained very well by elastic deformation, the exact mechanism for triggering the threshold of the single avalanche-like event is not entirely explained. Fig. 2.10 provides an explanation based on the screw-dislocation-line-mediated instability confirmed by simulation[183, 185]. The authors found that during this plastic flow, edge dislocations were pinned so that they were not the main reason for jump behaviours, by contrast, the screw dislocations everywhere in 8CB smectics played a big role. Under certain stress, the layers were compressed until a threshold force that is inversely proportional to threshold distance is reached, resulting in a layer being removed, then with a small additional force, the next layer jumped, during which the screw dislocation line (SDL) was compressed from a straight line into a helix, afterwards growing into a larger radius becoming edge dislocation. At higher compression rate, multiple-layer jumps are also observed. These behaviours are not determined by the strain or stress, but arise directly due to the order parameter in the form of the SDL. Further optical examination in a Grandjean-Cano wedge[186-188] confirms that those screw dislocations are pinned on the surface such that dragging the movement of the surface.

2.2.2.2 Shear forces of LCs in the SFA

Normal forces done with 8CB have been shown in section 2.2.2.1, here only viscosity and friction by shear measurements with different anchoring conditions[167] will be discussed, and are shown in Fig. 2.11, where two monolayers, dihexadecyldimethyl ammonium acetate (DHDAA) and cadmium arachidate (Cd-arachidate), with different

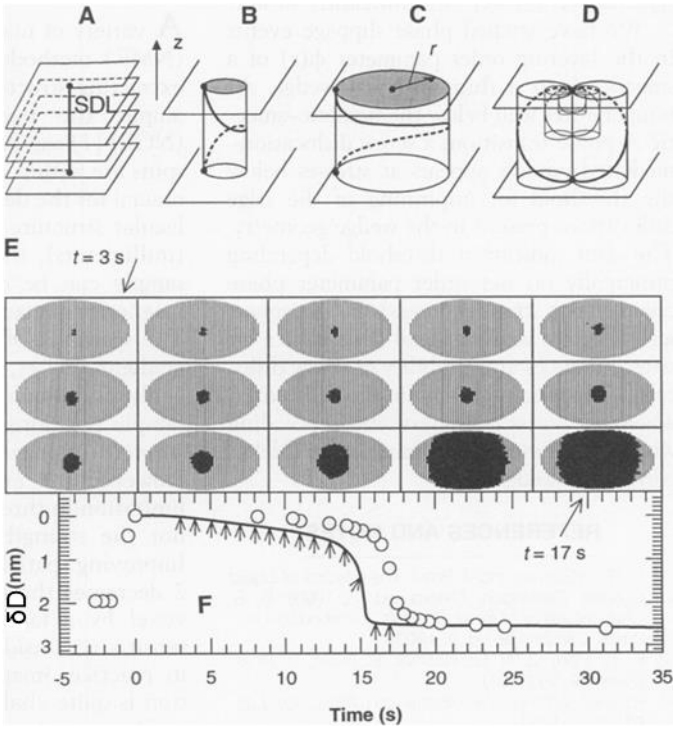

Figure 2.10 Screw dislocation line (SDL) avalanches in a smectic A, the figure is adapted from reference[183]. (A) Straight SDL with 2π rotation. (B) Helical SDL after squeezing out of one layer. (C) Expansion of radius *r* of SDL under compression of the surface. (D) SDL pairs under compression. (E) Simulation and (F) experiment of jump behaviours, snapshots in (E) starting from t = 3 s are indicated with arrows in (F) where surface displacement δD is a function of time, open circles are from experimental data, the solid line is simulation data.

packing densities, are used to induce homeotropic anchoring. DHDAA is a loose-packed amorphous monolayer at low temperature but liquid-like at high temperature, which allows LCs to penetrate into the monolayer causing strong anchored LCs that cannot be totally removed under strong compression. By contrast, Cd-arachidate is a dense-packed solid monolayer but with possible defects within the temperature range for measurements, which form better ordering LCs on surfaces, manifesting short-range structural layers that can be almost totally removed by compression.

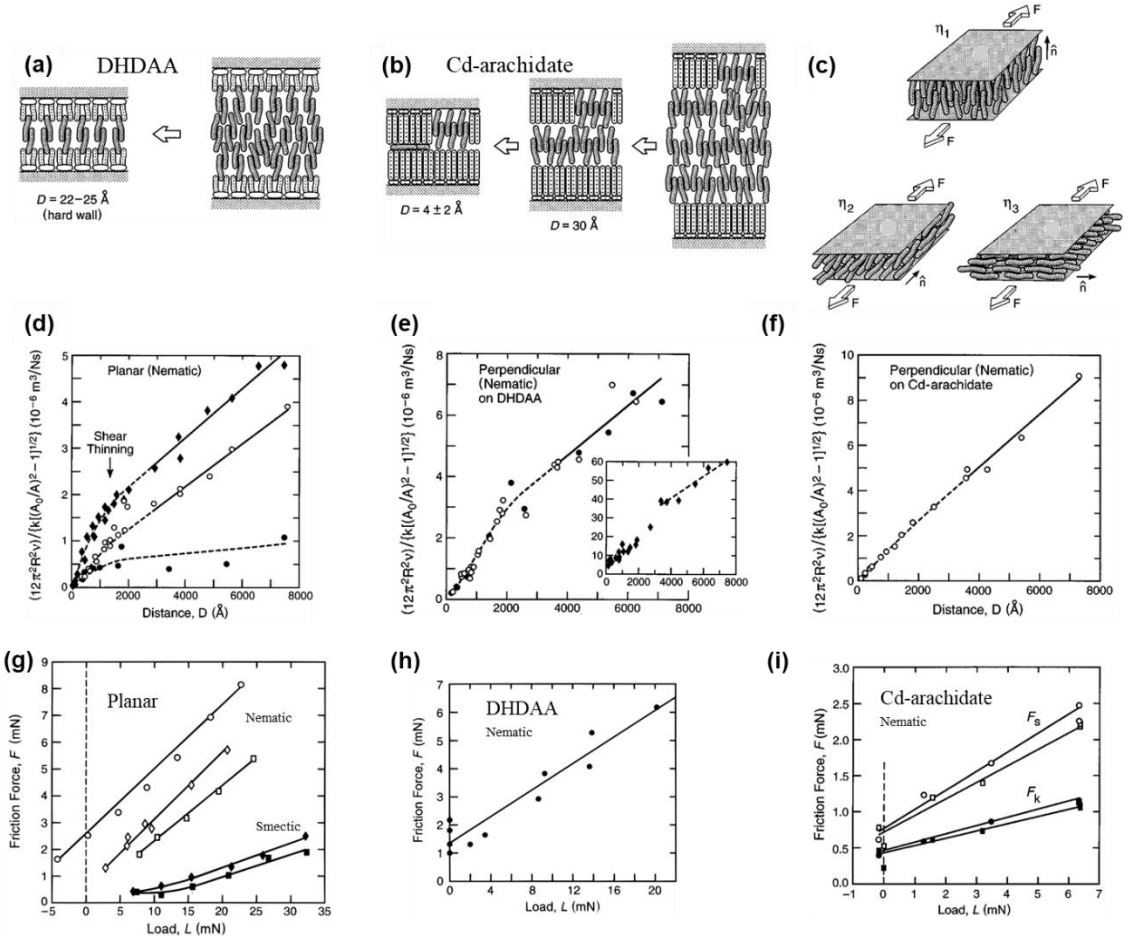

Figure 2.11 Shear of 8CB LCs in the SFA, figures are adapted from reference[167]. Schematic diagram of confined LCs with (a) dihexadecyldimethyl ammonium acetate (DHDAA) and (b) cadmium arachidate (Cd-arachidate) alignment. (c) Schematic diagram of different molecule orientations under shear, F is shear force, η is viscosity, $\hat{n}$ is molecule director. (d-f) Shear parameter $1\ 2\pi^2R^2v/[k[(A_0/A)^2-1]^{0.5}]$ (shown in main text) as a function of distance D with nematic 8CB on different surface alignments, inverse of the slope is viscosity. Filled circles are shear rate $v = 0.0\ 5s^{-1}$, open circles are $v = 0.1\ s^{-1}$, filled diamonds are $v = 0.2\ s^{-1}$, inserted panel shows very small viscosity. (g-i) Friction force F as a function of load force L with nematic or smectic 8CB on different surface alignments, (g) Open symbols are nematic while filled symbols are smectic, circles are shear speed $v = 0.0\ 6\mu\ m/s$, diamonds are $v = 0.1\ \mu\ m/s$, squares are $v = 0.2\ \mu\ m/s$. (h) Circles are shear speed $v = 0.0\ 6\mu\ m/s$ (i) Circles are shear speed $v = 0.0\ 6\mu\ m/s$, squares are $v = 0.1\ 7\mu\ m/s$, F_s and F_k are static and kinetic frictions respectively.

Three possible configurations for molecule orientation under shear are shown in Fig. 2.11c, where molecules could be parallel to shear gradient, shear direction or perpendicular to both shear gradient and shear direction, which produce three possible viscosities called Miesowicz viscosity coefficients[23]. If the molecules are between the latter two cases, for example, 45 ° with shear direction, the viscosity will increase due to this more disordering orientation. Viscosity η can be measured by vertical oscillation of one surface with certain amplitude and frequency with a no-slip boundary assumption[167],

$$\eta = \frac{k\ D}{1\ 2\pi^2 R^2 \nu}\left[\left(\frac{A_0}{A}\right)^2 - 1\right]^{0.5} \tag{2.13}$$

where k is the spring constant, D is the surface distance, R is the radius of the cylinder, ν is the oscillating frequency, A_0 is the applied amplitude that is typically less than 1/10 of surface distance D, A is the measured amplitude.

Shear thinning, decrease of the viscosity by shear, was observed in all configurations with nematic 8CB at distances smaller than 200 nm where boundary conditions had a strong effect and corresponding viscosities were consistent with reported measurements[189], shown in Fig. 2.11d-f, although shear thinning was not obvious with dense-packed Cd-arachidate. The increase of shear rate that aligns molecules better also increased the shear-thinning effect resulting in much lower viscosity. For smectics, the measured viscosities were typically 1 order higher than that in nematics, which was attributed to the inter-penetration between smectic layers called *permeation*[190].

For friction measurements shown in Fig. 2.11g-i, the smectic phase shows a lower friction coefficient that slightly depends on shear velocity than in the nematic phase under planar anchoring, which means better ordering in LCs gives rise to lower friction. However, no stick-slip motion was observed, indicating that shear-induced ordering was still not strong

enough to cause static friction[167]. This ordering effect also demonstrates the difference in two different monolayer coatings. With the dense-packed Cd-arachidate monolayer, the friction coefficient was smaller in nematic 8CB than the case with DHDAA, even stick-slip motion was observed, revealing strong smectic ordering, which is consistent with observation in short-range structural forces. On the other hand, with Cd-arachidate, only small loads can be applied to induce friction motion, since LCs were easily removed on this dense-packed monolayer.

2.3 Experimental setup

2.3.1 Liquid crystal anchoring on mica surface

Experiments in section 2.2 have revealed the importance of boundary conditions, therefore the anchoring directions are checked firstly before performing an experiment with the SFA. Nematic LCs QYPDLC-036 purchased from Qingdao QY LC Co., Ltd (Chengyang China) were used to check easy axes on mica, shown in Fig. 2.12, where cleaved mica with crystalline steps was used. The LCs were sandwiched between a mica plate with crystallographic steps and a glass slide coated with octadecyl-trichloro-silane (OTS) monolayer inducing homeotropic anchoring[83]. This homeotropic anchoring surface is used to ensure only a single anchoring direction dominates. Although LC anchoring on mica has been discussed in section 2.2.1, the optics dealing with birefringence from both mica and LCs may still be complicated. When the γ axis of mica is rotated to be either parallel or perpendicular with the analyser, bare mica without LC coverage is black and two domains LC1 and LC2 on different steps can be seen in Fig. 2.12a, indicating that LC director is not aligned the same as the γ axis. If mica is rotated clockwise 30 °, the colour of mica changes to blue, simultaneously the LC domain LC2

becomes almost identical colour as bare mica while LC1 is yellow shown in Fig. 2.12b, signifying that two domains do not align in the same direction and the domain LC2 is not producing a birefringent effect, i.e. the director of LCs in LC2 is either parallel or perpendicular to the analyser. This is also applied to the counterclockwise rotation where the easy axis on LC1 domain is either parallel or perpendicular with the analyser, shown in Fig. 2.12c.

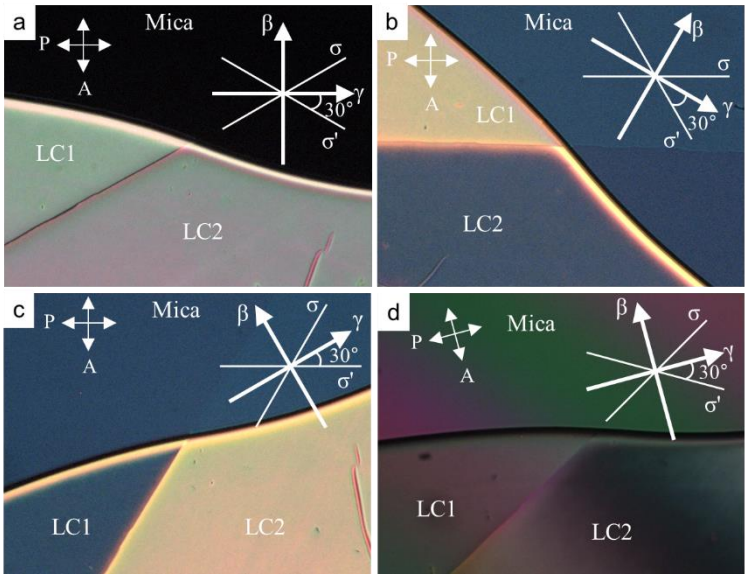

Figure 2.12 LC anchoring on mica surfaces. (a) Nematic LC domains on a mica surface under a polarized microscope. LC1 and LC2 are domains on different mica crystalline steps, the black region is mica without LCs, β and γ are index axes of mica that are parallel with analyser "A" and polarizer "P" respectively, σ and σ' are possible easy axes with ±30 ° to γ axis. (b) Rotation of mica until σ axis is parallel with polarizer "P". (c) Rotation of mica until σ' axis is parallel with polarizer "P". (d) Rotation of mica until σ axis is perpendicular with the inserted γ axis of the compensator, rotation of analyser "A" and polarizer "P" to be parallel with β and γ axes respectively, the black shadow on LC2 is compensated region by changing the thickness of compensator.

The polarizer and analyser are not enough to determine the exact direction of the easy axis alone. Here, a Berek compensator made by Leica (Germany) is used to determine

the γ axis of the mica and the director of the LCs. Firstly, mica without LC coverage is examined by aligning it parallel or perpendicular with the γ axis of the compensator. Subsequently, the compensator is rotated to change the thickness. If black textures are seen, it means that the γ axis of mica is perpendicular with the γ axis of the compensator, or else, parallel. This method is based on Michel-Lévy interference colour chart[191] where the colour of a sample of given thickness changes periodically due to birefringence when rotated under a polarized microscope, shown in Fig. 2.13. If the γ axes of the mica and the compensator are parallel, a change of compensator thickness will never decrease the effective birefringence to black. By contrary, if the γ axes of the mica and the compensator are perpendicular with each other, the birefringence of the compensator could cancel that of the mica resulting in a black colour provided that the thickness of the mica is reasonably thin. After determining the γ axes of the mica, a LC director is checked with the same method, shown in Fig. 2.12d, except that meanwhile, polarizer and analyser need to be aligned to cancel the birefringence of mica avoiding confusion. Indeed, easy axis σ is ±30 ° to γ axis on the alternate crystalline layer of mica, consistent with the reported results obtained with other cyanobiphenyl-based LCs[76, 172, 174].

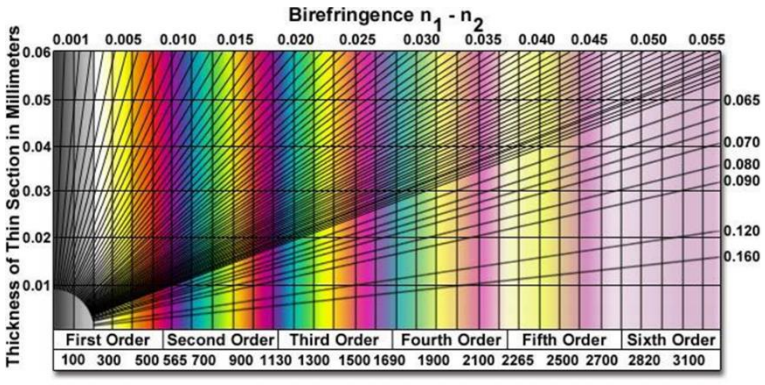

Figure 2.13 Michel-Lévy interference colour chart with colour as a function of the thickness of the thin section, birefringence n_1-n_2 and retardation in wavelength (bottom axis). Six order colours are shown, the figure is adapted from reference[191].

With time exposed to ambient air, the easy axis σ, for example, -30 ° crystalline case shown in Fig. 2.14, shifts discontinuously to σ_1 = 30 ° then finally σ_2 = 60 ° that is perpendicular with the original easy axis. This is also consistent with research[174] performed with LC *E*9, although in this study more complicated and reversible transitions were observed with controlled water vapour pressure, which was explained by a change of interfacial energy[78, 174] after adsorption of water molecules.

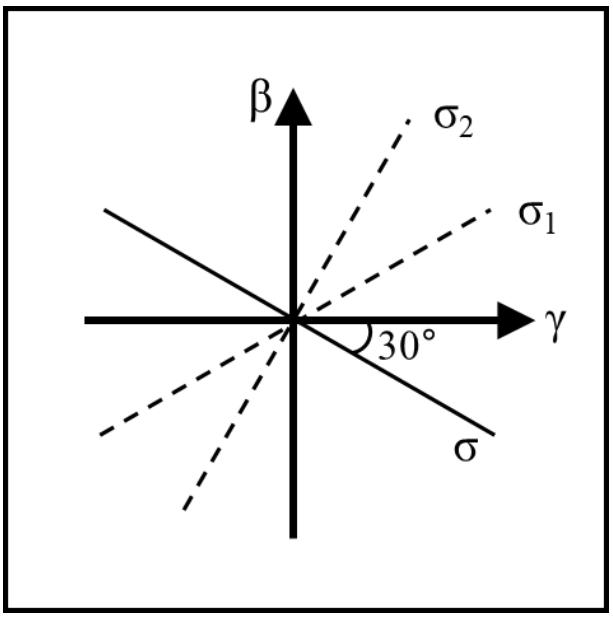

Figure 2.14 Anchoring transitions from easy axis σ = -30 ° to σ_1 = 30 ° then σ_2 = 60 ° with time exposed to ambient air, β and γ are index axes of mica and Cartesian coordinates.

2.3.2 Mica cleavage and silvering

Mica is a mineral that can be easily cleaved on [001] crystalline cleavage plane[169]. Typically, brownish muscovite mica with known refractive index is used as it provides an atomically smooth surface for SFA measurements. Cleavage can be initiated by tearing the edge of the mica or splitting the mica with a sharp needle. If the cleaved mica is thin enough, usually below 10 μm, colourful domains with crystalline steps can be observed,

with a brighter colour corresponding to thinner mica, shown in Fig. 2.15a. The colours are from thin-film constructive interference between two refractive rays from top and bottom surfaces, so that they can be used to indicate equal-thickness regions that can be easily larger than 1 cm^2. Generally, mica with bright colour but still rigid enough to be handled producing around 3 μm thickness is used in the SFA. Mica pieces with the large area are cut with a hot platinum wire before being laid down on a large back sheet of mica that attracts and protects mica pieces by van der Waals forces. This process should be quick and the mica is oriented to be upstream of the platinum wire in the laminar airflow to avoid the platinum particles from hot wire adhering to the freshly cleaved surface[192], thus thick mica that is difficult to cut cannot be guaranteed to be free from particle pollutants. All the cleavage processes are performed in a laminar flow hood, though, some visible contaminations from mica flakes or the platinum wire are inevitable, which shows bumps between the mica pieces and the back sheet.

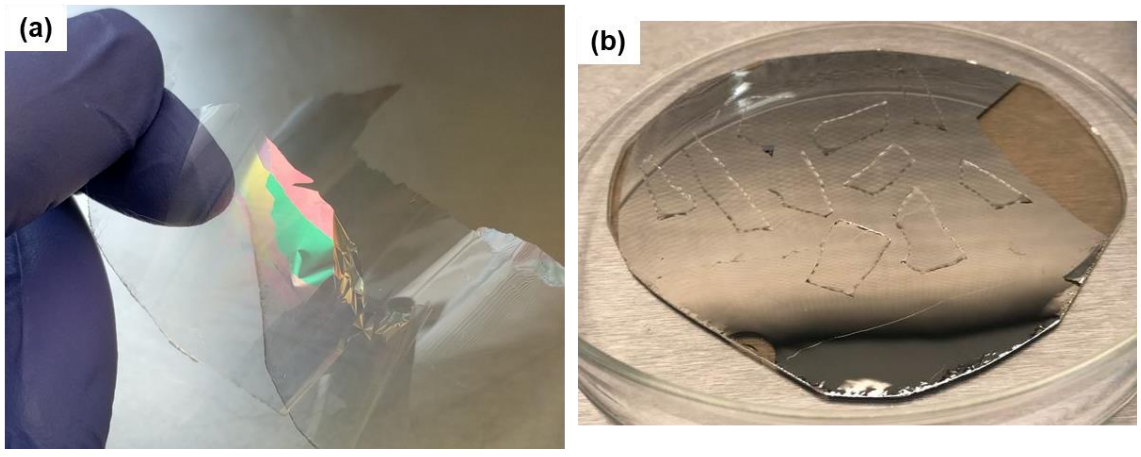

Figure 2.15 Mica cleavage and silvering. (a) Crystalline domains with different thicknesses of cleaved mica, each colour represents an area of equal thicknesses. (b) Mica pieces coated with a 55 nm layer of silver, sitting on a backing sheet of mica, the figure was provided by Hannah Hayler.

The cleaved mica sheet is transferred to a vacuum evaporator for coating with 55 nm of silver that is measured by the vibration of quartz crystal. The evaporating rate is below 1 Å/s, controlled by the current to ensure a smooth deposition of silver, producing a smooth mirror. Mirrors with thicknesses below 55 nm are sometimes used to generate brighter fringes on spectrometer for easy tracking and analysis. After cooling down in the vacuum chamber, the mica sheet is placed in a glass petri dish, shown in Fig. 2.15b, which has been cleaned by piranha solution, then the dish is transferred to a desiccator for storage. When needed in an experiment, a piece of mica is cut into the desired size and picked up to glue on the cylindrical lens.

2.3.3 Cylindrical lens preparation

Before glueing the mica to a cylindrical lens, all the metallic tools that are used to cut the mica or handle other necessary materials are sonicated by three solvents, namely toluene, chloroform and ethanol each for 5 minutes to dissolve grease and other organic contaminants, before they are rinsed with plenty of deionized and purified water with high resistance, 18.2 MΩ·cm, and total organic carbon (TOC) lower than 5 ppb. Subsequently, tools are cleaned with 33% diluted nitric acid for a few hours to further remove organic contaminations and avoid rusting. Finally, tools are rinsed with plenty of deionized water with TOC lower than 2 ppb and stored in ethanol. The SFB boat, which contains the cantilever spring onto which one lens is mounted, is cleaned the same way as tools, although due to its delicacy it is only sonicated in each solvent for around 10 seconds.

For glassware or Teflon components, the pre-treatment with three solvents and water is the same as tools. However they are cleaned with piranha solution, a mixture of 3 portions

of H_2SO_4 and 1 portion of H_2O_2 to totally remove any organic contaminants. The reaction between piranha solution and organic contaminations is very strong that might explode, which is quite dangerous, therefore special precaution must be followed in the lab when handling piranha solution, furthermore, glassware and Teflon components should be pre-cleaned quite well before being put into piranha solution. Finally, glassware and Teflon components are rinsed with plenty of deionized water with TOC lower than 2 ppb and dried by Nitrogen gas or heater then wrapped by aluminium foil.

All the tools are taken out from ethanol and dried by the flow in a laminar flow hood, shown in Fig. 2.16a, where tools and syringe are sitting on petri dishes and foils, which is ready for lens glueing. Two lenses are put on a heater and heated to 180 ° to remove residual ethanol and melt 1004F EPON resin glue. A needle is used to smoothly spread glue until no major defects are seen on the lens. After this, a piece of mica is cut and placed on the lens with the silver side laying down on lens. The laminar flow and capillary forces from the melted glue help to smooth the mica onto the lens, however, sometimes tweezer is needed to stretch possibly wrinkled mica. The lenses with glued mica are shown in Fig. 2.16b stored in petri dish.

2.3.4 Surface Force Balance assembly

The lenses are mounted and tightened by screws to seats on the spring boat and top part. The top part contains a piezoelectric tube for fine vertical motion and an air gap capacitor to measure lateral motion (see section 2.1.1), shown in Fig. 2.17. This operation needs to be very careful with tweezer holding seats made by foils, not only to avoid possible dust but also to not twist or detach delicate components such as spring.

Subsequently, the spring boat and top part are mounted to the SFB chamber to make

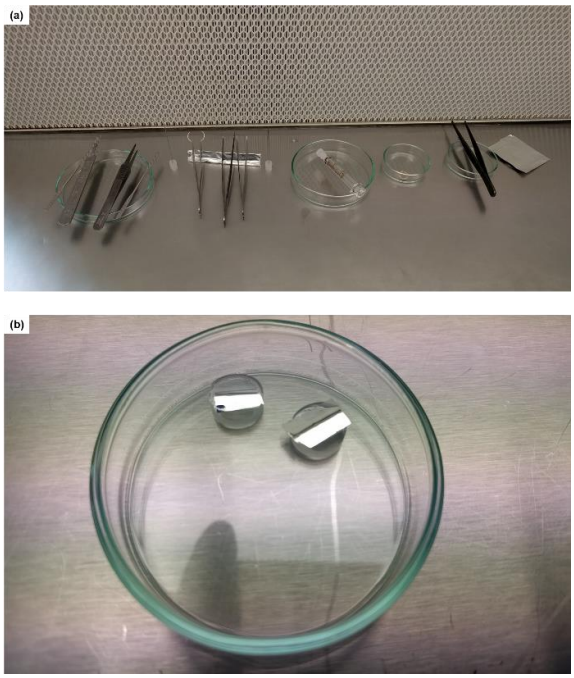

Figure 2.16 Cylindrical lens preparation. (a) Tools and syringe on a glass petri dish or aluminium foils (b) Prepared lenses with back-silvered mica glued by 1004F EPON resin.

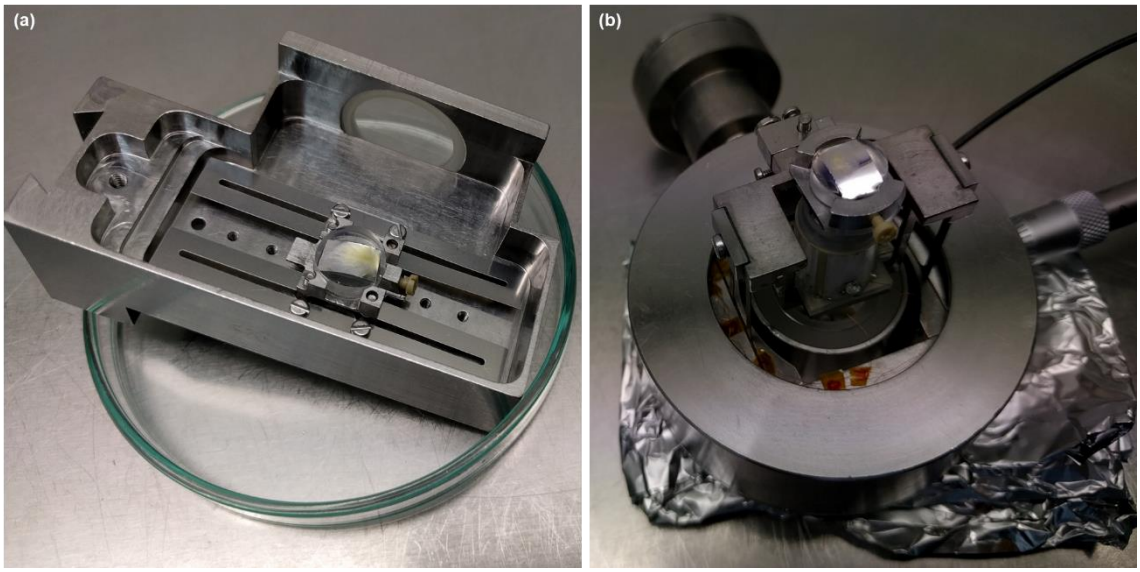

Figure 2.17 Assembly of the lens on (a) spring boat and (b) top part.

crossed cylinders shown in Fig. 2.18. If an electric field is needed, a plug-in component with wires is available to connect with the boat and the handle of the chamber. A P_2O_5 desiccant is placed in the SFB chamber to adsorb water vapour in the chamber preventing

unstable anchoring transitions on the mica surfaces. This P_2O_5 is a strong hygroscopic chemical that produces lots of heat when reacting with water, which is dangerous during disposal to the sink. Finally, the door of the chamber is closed by tightening the screws. There are several windows that are dismountable on the door of the chamber for wire connection, injection and gas or liquid circulation.

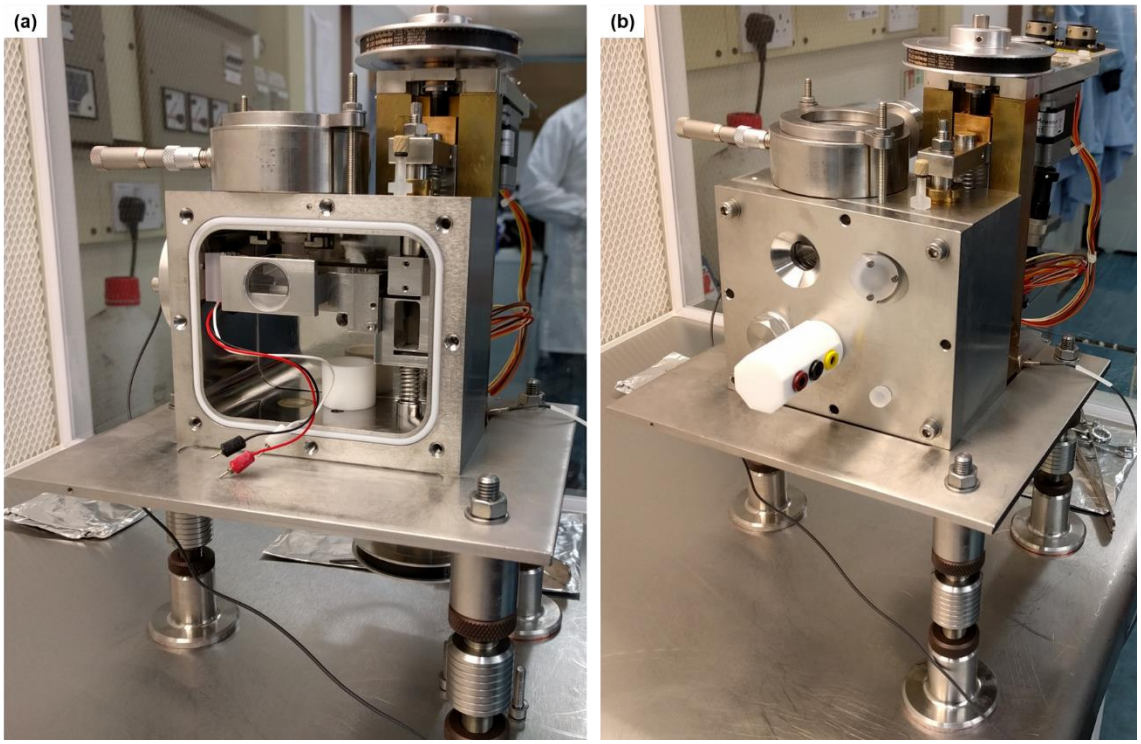

Figure 2.18 Assembly of the SFB. (a) The assembled chamber interior, including the spring boat, top part, and Teflon cup containing P_2O_5. (b) Sealed chamber with the door, the Teflon handle is for electric connections.

The SFB experiment is conducted in an isolated thermostatic room free from wet chemistry. The assembled SFB instrument is transferred to this room before collimated white light being calibrated, so that the light is vertically inserted to crossed-cylindrical surfaces. The SFB chamber is purged with filtered high purity nitrogen at least 1 h, drying the whole chamber and mica surfaces removing any absorbed water. During drying, the

SFB is connected with all external wires and cables, and the surface contact spot is checked to see if there is any flaw. Firstly, the capacitance probe is set to be grounded for further use to check surface purity or friction measurement. Secondly, the piezo controller and motors are connected with all the cables clamped with damping rubbers to absorb vibrations, then the related software could be started. Finally, the contact spot is checked with a microscope by which a bright cross could be seen. If the spot is too close to the edge of mica or there are bumps or defects around the spot, the top part needs to be untightened and moved on both parallel and perpendicular directions of the cylinder until a good spot is observed.

After nitrogen purging, the SFB is ready for contact calibration. At this time, the vibration table upon which the SFA is mounted, camera and other related instruments are turned on. The vibration table is used to actively damp any vibrations from the surrounding environment, which is very sensitive to large shake, therefore it could only be turned on after connection of cables and needs to be turned off once large shake is applied. Likewise, the camera cannot work for very long times and needs to be turned off when it is not in use. Subsequently, the interference light from the crossed cylinders is finely tuned to be vertically incident in the spectrometer through a prism until bright and clear fringes can be seen on the monitor screen. Finally, the surfaces are gently brought into contact for contact calibration successively by the coarse motor, fine motor and piezoelectric tube. More details about the contact calibration and related analysis will be shown in section C.

After contact calibration, surfaces are separated to a large distance, then the SFB is disconnected and transferred to a laminar flow hood for injection. About 30 μL of liquid is injected to the gap between crossed cylinders forming a capillary bridge using a clean

syringe or pipette through the dismountable window on the door of the chamber. Sometimes, the door of the chamber will be totally dismounted for convenience during the injection.

2.3.5 Grandjean-Cano wedge and crossed-cylinder geometry

It has been shown in section 2.1.1 that geometry under crossed cylinders is very similar to a sphere approaching flat plate as long as surface separation is much smaller than the radius of the cylinder. In Fig. 2.19 the textures formed by cholesterics, 62.4 wt% nematics QYPDLC-036 (similar to the BL036 with low temperature sensitivity from Merck) and 37.6 wt% chiral dopant R2011 purchased from Qingdao QY LC Co., Ltd (Chengyang China), in both the Grandjean-Cano wedge and crossed cylinders are compared. Under confinement by thickness gradient, integral half-pitch layers of cholesterics distribute along the whole space drawing isocline-like map. Between adjacent layers, a clear defect line forms, which is very clear under a polarized microscope. A Grandjean-Cano wedge forms parallel equally-spaced lines while crossed cylinders form non-equidistant circles confirming that indeed crossed-cylindrical geometry is similar to sphere-plate geometry. The intervals between the circles without any deformation decrease with increasing distance, following equation 2.1.

2.3.6 Liquid crystal desiccation

Section 2.2 has shown that LC experiments in an SFA were easily influenced by surface properties, sample materials and the ambient environment, since the SFA is a very sensitive technique to probe those subtle behaviours. During an experiment, usually fresh mica cleaved in laminar flow hood and stored in desiccator is used; all the tools related to experiment are properly cleaned; LCs are 99% pure and are purchased from the

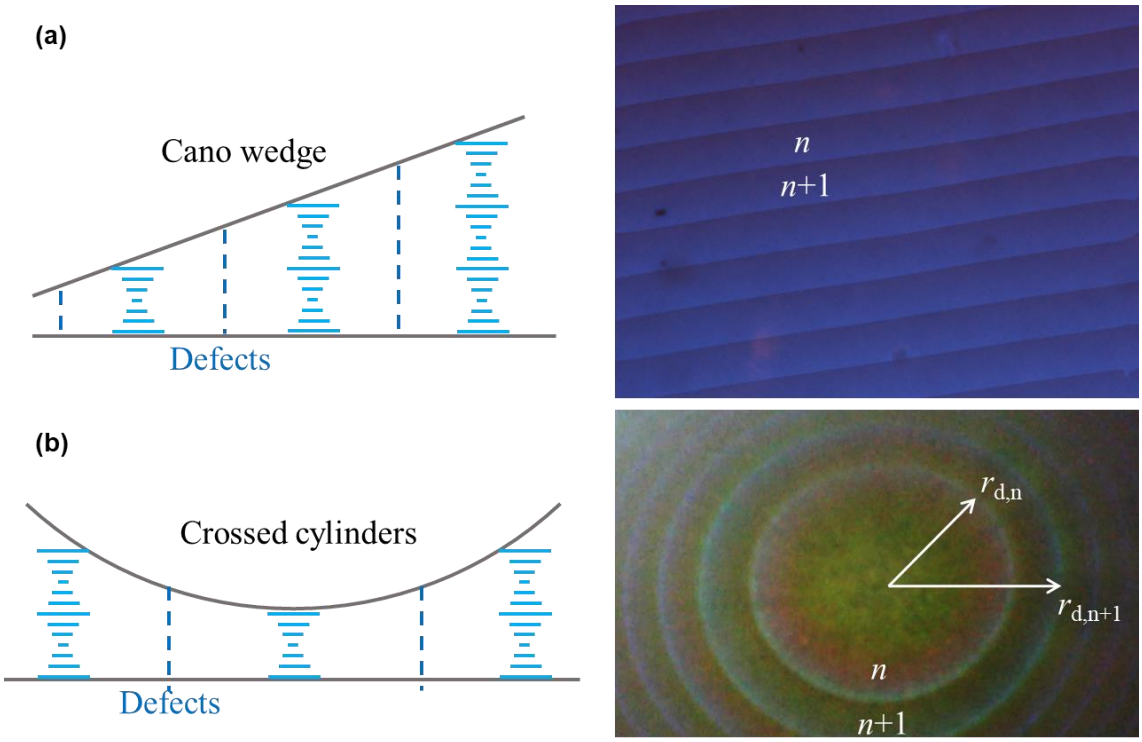

Figure 2.19 Observation of dislocation lines in cholesterics. (a) Schematic diagram and microscope image of cholesterics confined in (a) the Grandjean-Cano wedge and (b) crossed cylinders. n represents integral half-pitch cholesteric layers, $r_{d,n}$ is the radius of the n^{th} defect.

professional chemical company; filtered high purity nitrogen is purged for at least 1 h to dry the surfaces and chamber; P_2O_5 is adopted to keep the chamber dry during the experiment; Experimental room is free of wet chemistry with controlled temperature and monitored humidity. Nevertheless, the anchoring of LCs was still not stable in a typical experimental timescale. This could be due to the fact that LCs, such as 5CB, are hygroscopic materials, and despite efforts to keep the experiment free from water, the LCs still manage to adsorb some atmospheric water vapour. It has been shown that even a very small amount of specific chemicals, such as Endotoxin[100], were able to induce a transition from planar to homeotropic anchoring. As a result, LCs used in experiments are dried on a Schlenk Line under vacuum and 50 ° heat overnight to remove any

dissolved chemicals before injection. Only at the moment of injection will the stopper be opened to release the vacuum status in the flask.

2.4 Summary

After decades of development, the SFA has become a mature technique for simultaneous measurements of surface separation and the encountering forces in confined geometry. This chapter reviews the mechanisms of the SFA and its modified versions, as well as optical and mechanical responses of LCs confined in the SFA, including some intriguing puzzles. Finally, the setup of the SFB is shown to highlight some key experimental procedures. Some conclusions are drawn below,

(1) The multiple-beam interferometry based SFA provides a unique tool to measure surface separation and forces with resolution 0.1 nm and 0.1 μN respectively. The crossed cylinder geometry is equivalent to a sphere approaching flat plate at surface separations much smaller than the radius of cylinders.

(2) The splitting of fringes generated by multiple birefringence layers is affected by the retardation of single layer and their relative intersection angle, which could be understood by the parallelogram rule with double intersection angle under the assumption that phase change and dispersion at interfaces is negligible.

(3) The surface properties of mica and humidity in ambient air affect the anchoring and its transitions, therefore, fringe behaviours can be tuned by engineering the anchoring condition on surfaces. Stimuli-sensitive LCs also allow external manipulation, such as the electric field.

(4) Two medium-range forces, twist elastic force and order-parameter-related force, and short-range structural force dominate normal forces with nematics under SFA confinement.

(5) Elastic compression explains the deformation during the squeezing of lyotropic multilamellar mesophases, while the threshold during layer jumps in smectics is expounded as screw-dislocation-line-mediated instability rather than strain or stress under the confinement of the SFA.

(6) Nematics under confinement and shear enhance positional order and orientational order respectively. This enhanced orientational order induces shear thinning that decreases viscosity. The viscosity of smectics is almost one order higher than that of nematics.

(7) With planar anchoring, the friction coefficient is lower in smectics than in nematics, which is related to the ordering in the LC phase. Loose-packed monolayers induce strong homeotropic anchoring that impedes the squeezing out of the last LC layer and produces higher friction coefficients, whereas dense-packed monolayers that strengthen smectic ordering generate lower friction coefficients but lose LC layers easily.

(8) The easy axis of LCs on a mica surface is situated ± 30 ° to the γ axis alternately on mica crystalline layers. In a humid ambient environment, it reversely shifts to a metastable position finally to be perpendicular to the original direction.

(9) Nitrogen gas and P_2O_5 are introduced to dry the chamber and surfaces, furthermore, LCs are desiccated using a Schlenk line, in order to control stable anchoring conditions.

3 Analysis of multiple-beam interference

3.1 Introduction

As has been mentioned in section 2.2.1, the optical system of the SFA containing multiple birefringent layers is already complicated. Adding LCs that are birefringent and twisted simply increases the uncertainties in the distance measurement. This chapter will present the detection of surface separation at various distances with different chromatic orders. A simulation method based on 4x4 transfer matrix multiplication for the calibration and analysis of multiple-layer birefringence will be discussed to understand the splitting of fringes. Finally, the potential of simulation will be discussed. Some technical analysis showing the calibration of the optics and the understanding of fringe behaviour at contact will be presented in Appendix C.

3.2 Detection of surface separation

3.2.1 Short distance detection

After contact calibration, around 30 μL of the LC 5CB was injected into the gap between the crossed cylinders forming a capillary bridge. 5CB (4-Cyano-4'-pentylbiphenyl, C18H19N), was commonly used as the model system to perform LC experiments in the past studies shown in section 2.2. The melting point of the 5CB (Alfa Aesar, United States) from a crystalline phase to a nematic phase is 22-23 °C depending on the purity. Then a force profile including both approach and retraction was run with a low speed around 2 nm/s of the motor, and the evolving fringes/interference pattern was captured by a camera. Each frame of video was analysed by cropping and averaging 8 pixels of the centre region of the fringes that is the region encompassed by the dashed lines in Fig. C.1. Put together,

all frames formed a spectrogram in Fig. 3.1a showing the movement of fringes with time, which is directly correlated to the surface movement, by approaching surface from a certain distance at around 100 frames to contact during 700-800 frames, then retracting surface until 1400 frames. At the beginning and end parts of the spectrogram, the surfaces are almost still but slightly shifting due to thermal and mechanical drift. The splitting of the doublet increases with increasing distance, which is totally different from what is observed in isotropic liquids because the optical path difference from the birefringence of the LCs increases with increasing distance. Notably, the splitting of the prime fringe *q* is less sensitive to medium and keeps constant at small surface separations compared with the *q*-1 fringe, which is consistent with observations in Fig. C.1c and C.4.

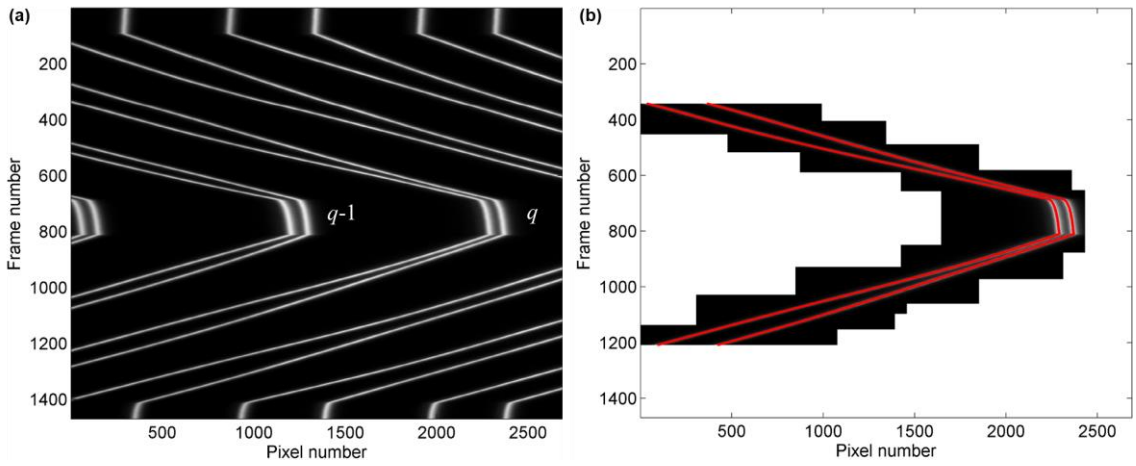

Figure 3.1 Short distance detection of surface motion. The frame number is approximately proportional to the elapsed time. (a) Spectrogram formed by cropping and averaging 8 pixels of the centre area of fringes, similar to Fig. C.1, from each frame of captured video. (b) Tagged *q* fringes in (a) for detection of peaks highlighted by red lines. The image is processed the same as in Fig. C.3.

Typically, the prime fringe *q* is cropped following procedures described for Fig. C.3 to detect the peak positions of the fringes which are highlighted by red lines in Fig. 3.1b. The detected wavelengths are converted into the distance by equation 2.2 with average

wavelengths of the doublet and average refractive index of the medium, shown in Fig. 3.2, where the surface moves almost linearly from 350 nm to contact then retracts to 350 nm. It is worth noting that the fixed boat with infinite spring constant avoids surface jumps due to van der Waals attraction near contact, but it also loses the information of forces that are encountered by the surfaces.

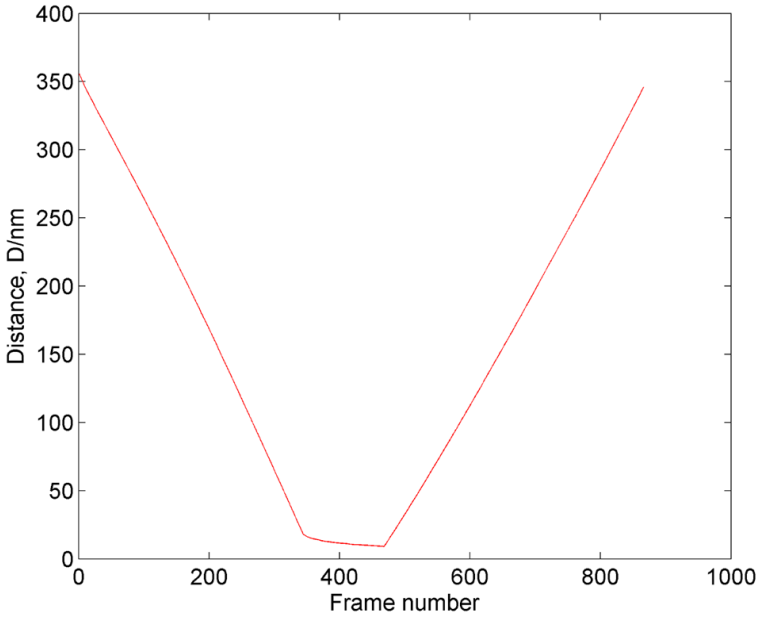

Figure 3.2 Distance profile of the prime fringe as a function of relative frame number in Fig. 3.1.

3.2.2 Long distance detection

In Fig. 3.1a, the prime fringe shifts to longer wavelength and finally disappears from the screen, such that the video at a large distance cannot be analysed if only the prime fringe is detected. In Fig. 3.3a, fringes and corresponding chromatic order relative to the prime fringe are taken into account in every frame, which extends the distance profile and narrows down the wavelength span that decreases errors of the spectrometer and wavelength-dependent refractive index. In this method, the relative chromatic order to

the prime fringe is used to extract the correct solution of the Tangent function in equation 2.2. The distance profile in Fig. 3.3b shows the distance evolution with time.

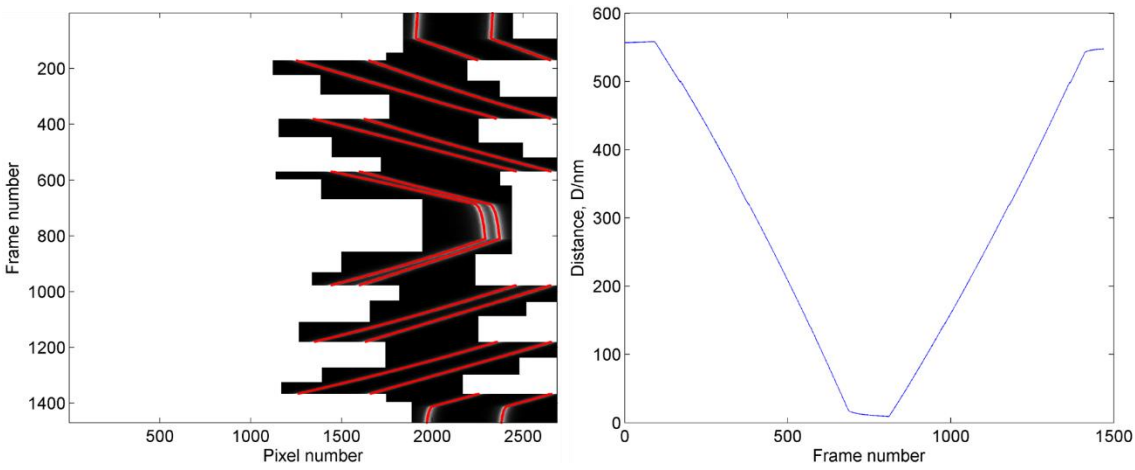

Figure 3.3 Long-distance detection of surface motion: (a) Tagged fringes in different chromatic orders across the whole spectrogram in Fig. 3.1a, red lines are detected peak positions. (b) Calculated whole distance profile as a function of frame number.

The difference between short and long-distance profile is shown in Fig. 3.4, where short (red) and long (blue) profiles overlay very well without obvious deviation. This small deviation is also shown in Fig. 3.4b where values in the long-distance profile are subtracted from the short-distance profile in the same region. In the frame range from 600 to 1000 marked with red centre lines, there is no deviation since they are all using prime fringe to do the calculation. In the other regions where the chromatic order is different, the deviation fluctuates without a certain tendency, but there is a sharp jump during the change of chromatic order. All the deviation is within 1.5 nm which is quite small considering that the distance is above 100 nm.

3.2.3 Effect of chromatic order on distance calculation

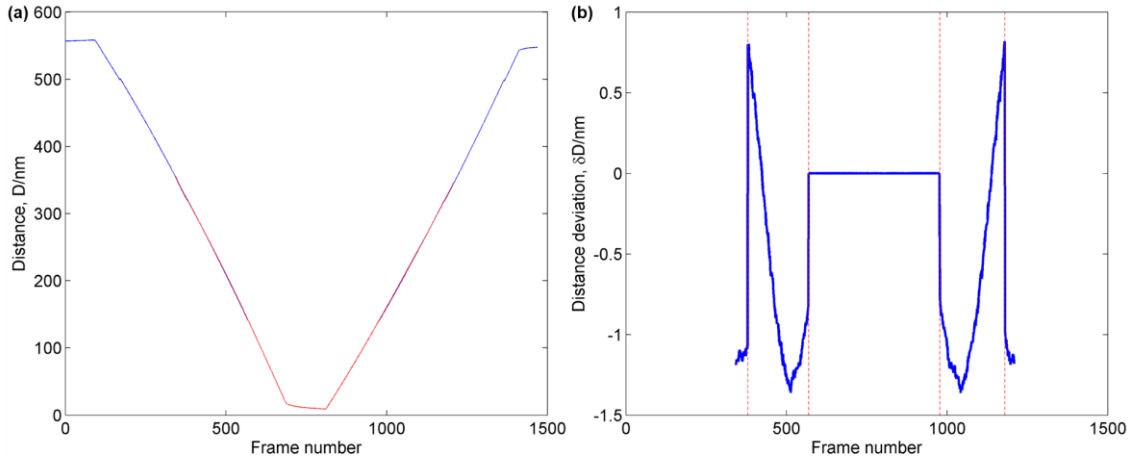

Figure 3.4 Comparison of short and long-distance profile: (a) overlay of short (red) and long (blue) distance profile. (b) Distance deviation between the long and short profile in the same frame range. The red centre lines are the position where chromatic changes occur in the long profile.

With the equation 2.2 used for calculating distance, the sign named Fnum needs to be considered depending on whether the reference prime fringe is odd (Fnum = 1) or even (Fnum = -1). However, it is not clear if the sign needs to be changed when the long distance is detected with higher chromatic order fringes. The results are compared with distance profiles calculated by Fnum = 1 and Fnum changing with parity in Fig. 3.5. From the overlay, it is hard to tell which method is correct since they have similar results. But, the deviation of those two methods is quite large shown in Fig. 3.5c where deviation fluctuates within 2.5 nm in the different sign of parity calculation and peaks at around frame 500 and symmetric frame 1100. Those deviations are 1% ($\delta D/D$) which is relatively high but if we compare the deviation in Fig. 3.4 which is caused by systematic errors, the results are still acceptable.

For the reasons mentioned above, air with a refractive index significantly different from that of the mica is used as the medium to highlight the deviation in the distance calculation using different Fnum. Fig. 3.6 shows a spectrogram similar to Fig. 3.1, though splitting

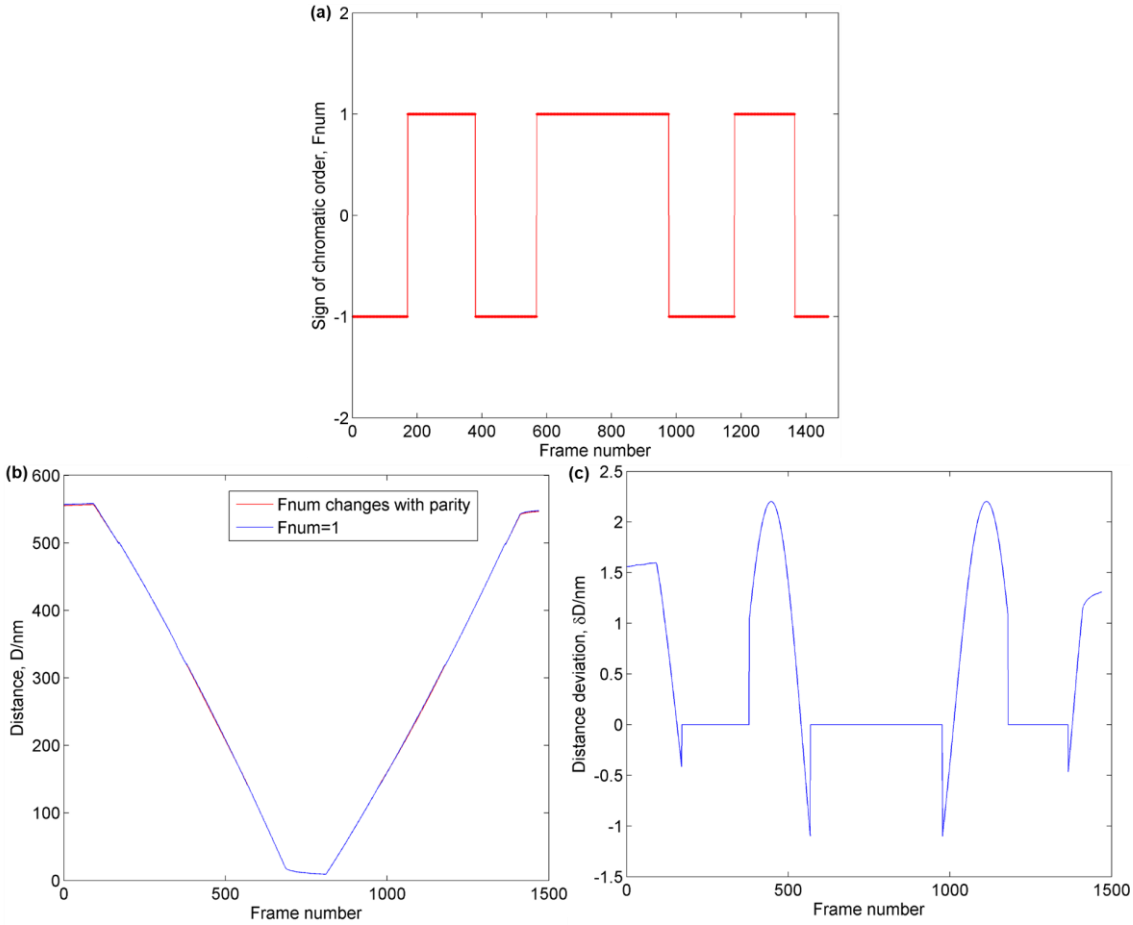

Figure 3.5 Effect of chromatic order in distance calculation of Fig. 3.3a: (a) Sign of parity of chromatic order named Fnum for distance calculation, odd (Fnum = 1) or even (Fnum = -1). (b) Overlay of distances with different Fnum, blue line is with Fnum = 1, while red line with Fnum changing by parity. (c) Deviation of distance profiles with constant and parity-determined Fnum.

is clearly larger at the contact position. This is because of larger mica thickness $Y = 4.3004$ μm and smaller intersection angle $\Psi = 28.6$ ° in Fig. 3.6. Specifically, Fig. 3.6a shows retraction of the surface from contact with a fixed spring boat. With infinite spring constant, adhesion at contact does not affect the delay of jump-out, so the surface jumps out sharply at frame 1000 after waiting some time in contact. Between frame 1000 and 1500, the motor stops, but two step-wise motions are applied to move the surfaces closer together. After frame 1500 the surface retracts linearly until frame 2500. Fringes appear

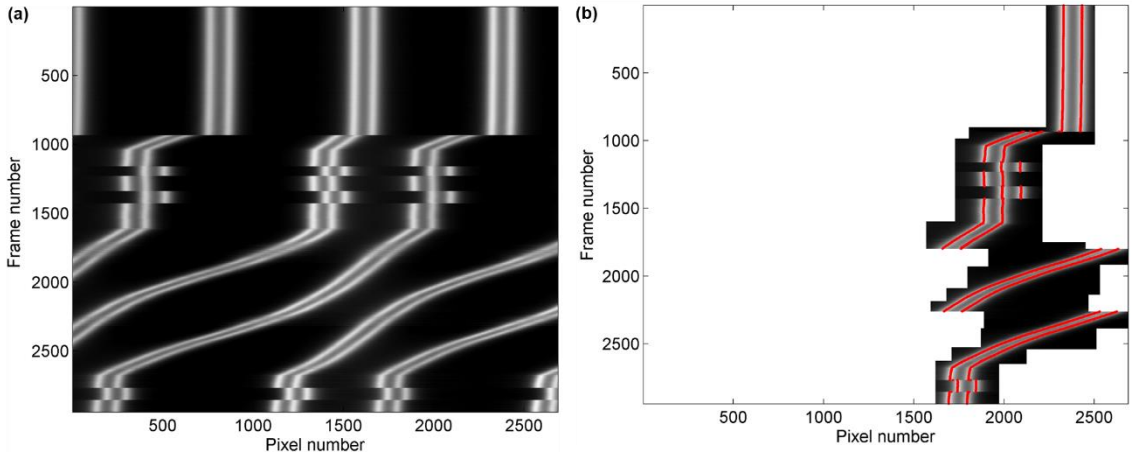

Figure 3.6 Spectrogram of surface motion in the air: (a) Spectrogram formed from a captured video of surface retraction from contact. The discontinuous fringes are due to step-wise motion of the surfaces. (b) Tagged fringes for detection of peaks highlighted by red lines. The image is processed the same as Fig. C.3.

wavy owing to the contrast of the refractive index between the medium and the mica. This spectrogram is tagged and detected in Fig. 3.6b using the method in Fig. 3.3.

The detected fringes in Fig. 3.6 are converted into distances with different Fnums either with a fixed sign or a sign based on the parity of fringes. Blue in Fig. 3.7b is calculated with Fnum = 1 for all points, which is consistent with the description in Fig. 3.6, while the overlaid red line with Fnum from parity, shown in Fig. 3.7a, shows large deviations in distance profile. Such deviations are magnified with air as the medium with up to 80 nm of errors as shown in Fig. 3.7c, which is not acceptable in experiments with large refractive index contrast.

To conclude, the sign of chromatic order calculated at a large distance does not need to change according to parity, as long as the parity of prime fringe at contact has been taken into account, nevertheless, relative chromatic order to the prime fringe is required to resolve the correct angle of the Tangent function in equation 2.2.

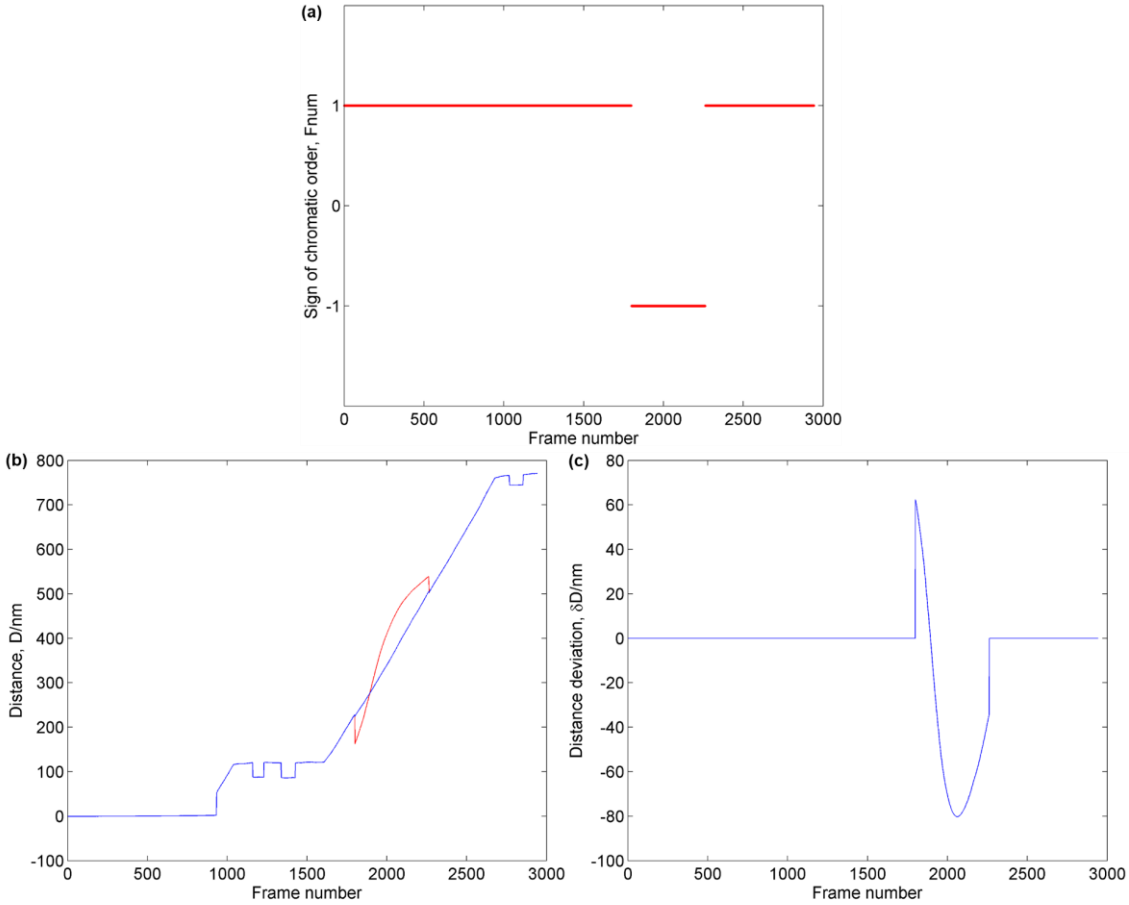

Figure 3.7 Effect of chromatic order in the distance calculation of Fig. 3.6: (a) Parity of chromatic order for the distance calculation. (b) Overlay of distances with different Fnum, the blue line is with Fnum = 1, whilst the red with Fnum changing by parity. (c) Deviation of distance profiles with constant and parity-determined Fnum.

3.3 Simulation of multiple-beam interferometry

3.3.1 Simulation tools

The transmissivity for multiple-beam interferometry with typically 3 layers have been calculated analytically[151, 193] and numerically[157, 160, 171, 194-197] based on a 2x2 matrix[198]. However, usually, only isotropic medium may be analysed with this approach, although sometimes the average wavelength can be analysed[171, 180]. Here the simulation tool developed in our lab[199], or a similar technique[200], based on a 4x4 method[201, 202] are

required to reproduce and analyse the MBI spectra produced under normal incidence by LCs in the SFA. We start by considering a uniform LC with the director parallel to the surfaces shown in Fig. 3.8. The mica surfaces are separated by a distance D with intersection angle Ψ between two index axes γ_1 and γ_2, the director forms an azimuthal angle φ to the bisector of Ψ and polar angle θ to the z axis normal to the surfaces. The simulation could capture the fringes obtained in this optical system, as long as the director configuration with respect to the mica surfaces is known.

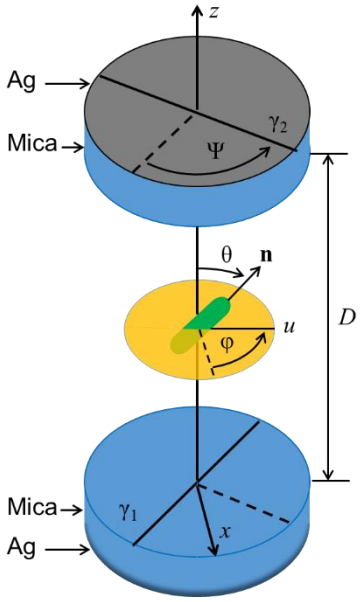

Figure 3.8 SFA setup for multiple-beam interferometry. With silver coating on the back, two mica surfaces are randomly separated with distance D along the normal axis z direction with acute intersection angle Ψ between two index axes γ_1 and γ_2. The bisector of Ψ is the x axis. The LC director **n** has polar angle θ to the z axis and projected direction u that forms an azimuthal angle φ with x.

3.3.2 Mica-mica contact simulation

With the 4x4 matrix simulation, the position of the fringes at contact are regenerated with the real mica thickness Y and the intersection angle Ψ calibrated in Table C.1. The thickness of silver layers estimated as 45 nm is also an important parameter taking phase

change into account. This thickness might need to be adjusted if the deposition thickness of silver is not correctly obtained from the silver evaporator. From the results shown in Fig. 3.9 where the fringes at contact are a function of the surface separation and the wavelength, the position of fringes is well-matched with red dots that are values from the measurement of the fringes in Table C.1, indicating that the thickness and intersection angle of mica has been accurately measured and calibrated by taking into account the phase change and dispersion.

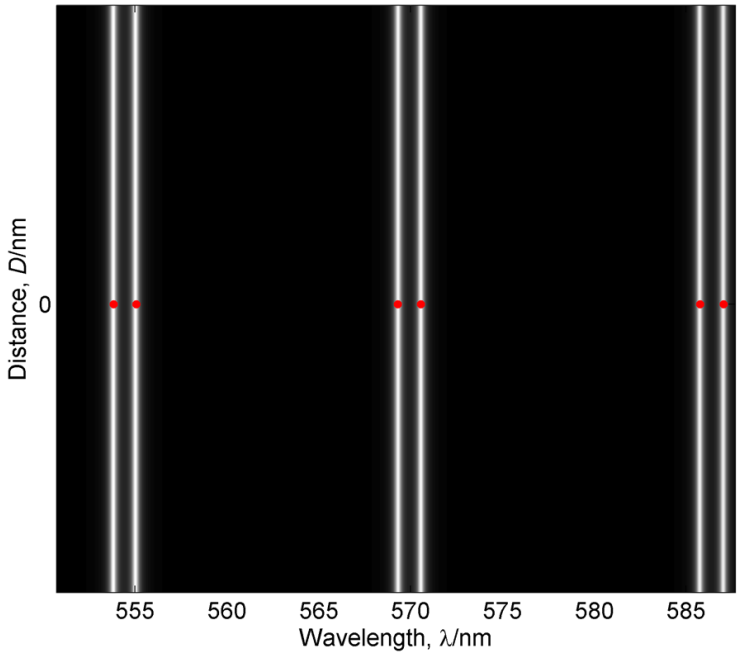

Figure 3.9 Simulation of fringes at mica-mica contact as a function of surface separation and wavelength. The red dots are wavelengths of the fringes from experiments shown in Fig. C.1. In the simulation, all the *x* axis has been converted into wavelength.

3.3.3 Equivalent isotropic simulation

Although the mica thickness Y and the intersection angle Ψ have been successfully extracted from the contact calibration and confirmed with simulation, the easy axis of the LCs deviates $\pm$ 30 ° from the index axis γ of mica depending on the alternate crystalline

facet[76, 174], which creates two possible configurations, shown in Fig. 3.10, for achiral nematics since the two surfaces face each other with the same facet. The twist angle Φ imposed to the LCs by the anchoring directions on mica could be either 13.2 ° or 73.2 ° which add difficulties and possibilities of errors for the simulation, thus, in the first instance, equivalent isotropic simulation is done to test distance profile and refractive index.

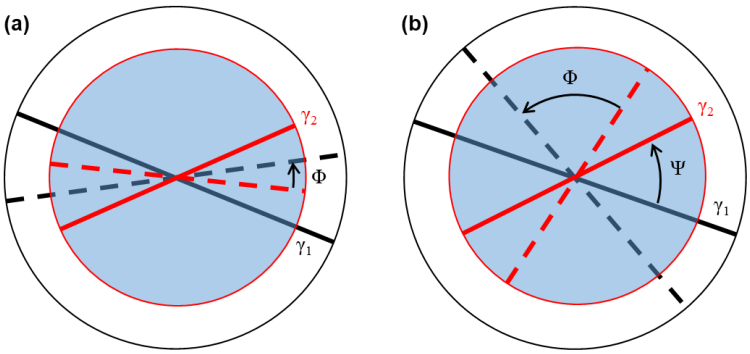

Figure 3.10 Two configurations of the anchoring easy axes in dashed lines with the intersection angle Ψ = 46.8 ° between index axes γ_1 and γ_2 in solid lines. Anchoring axes are (a) within or (b) outside angle Ψ forming twist angle Φ. The black and red lines are bottom and top mica respectively.

Equivalent isotropic simulation is based on the assumption that the average wavelength profile of a doublet fringe at a different distance is equivalent to the case where wavelengths form by isotropic media with average refractive indices of corresponding anisotropic media, regardless of number and orientation of layers. In the past study[151] dealing with the birefringence of mica, the average wavelengths and refractive indices have long been used to calculate the distance profile, but the accuracy of this assumption has not really been tested. More detailed discussion on this accuracy will be shown in section 3.3.11.

With the distance profile calculated in Fig. 3.3, the equivalent isotropic simulation is shown in Fig. 3.11a where red lines are overlaid average wavelengths from the experiment, which is in good agreement. Fig. 3.11b overlays the experimental and the isotropic spectrograms, where the isotropic wavelengths sit in the centre of experimental doublets, further confirming that the isotropic assumption is reasonable and practical for the test of the experimental data.

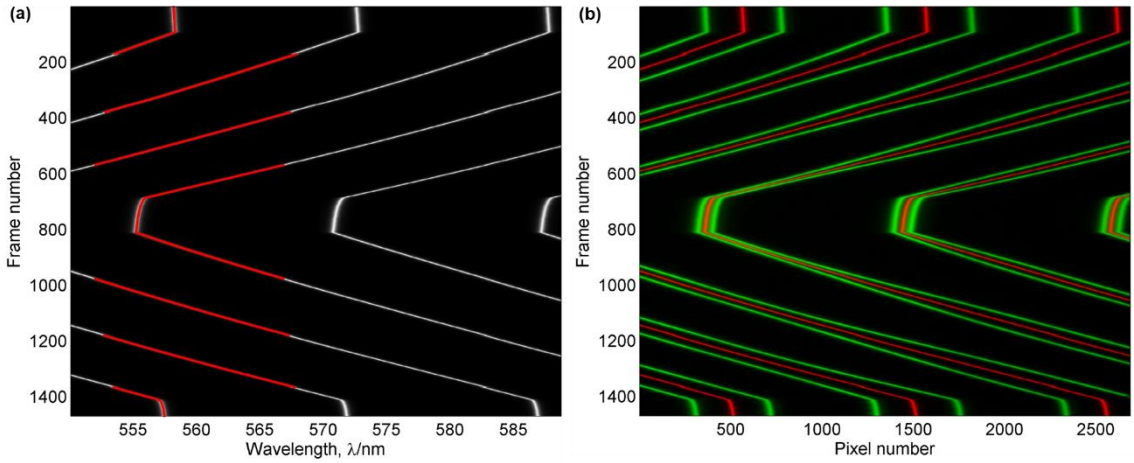

Figure 3.11 Comparison between experimental spectra and simulated spectra with equivalent isotropic simulation based on the distance profile shown in Fig. 3.3. (a) Isotropic spectrogram as a function of the frame number and the wavelengths, plotted with the average detected wavelength in red lines. (b) Overlay of the simulated isotropic (red) and experimental (green) spectrograms by the ImageJ.

One may doubt that, since the distance profile is calculated from the detected wavelengths assuming that refractive indices are known, then the inverted generation of wavelengths based on same refractive indices and distances will have a good match with the experimental values, even if wrong refractive indices are used. In the following sections, the refractive index and the sign of parity which affect distance calculation, will be discussed.

3.3.4 Effect of refractive index on isotropic equivalence

Wrong refractive index μ_o = 1.4, μ_e =1.5, rather than 5CB refractive index, are used for the distance profile which is adopted for the isotropic simulation shown in Fig. 3.12a with plotted experimental wavelengths in red lines. Although with some discontinuous steps in the same fringe, compared with smooth transitions in Fig. 3.11a, overall, the isotropic simulation is matched well with detected wavelengths. However, the overlaid isotropic and experimental spectrogram shows an obvious deviation in the wavelengths that are away from the detected region in Fig. 3.12b, where the isotropic wavelengths shift to smaller wavelengths owing to smaller average indices. In other words, the isotropic equivalence provides a simple way to indicate if the average refractive index has been correctly adopted, regardless of the birefringence.

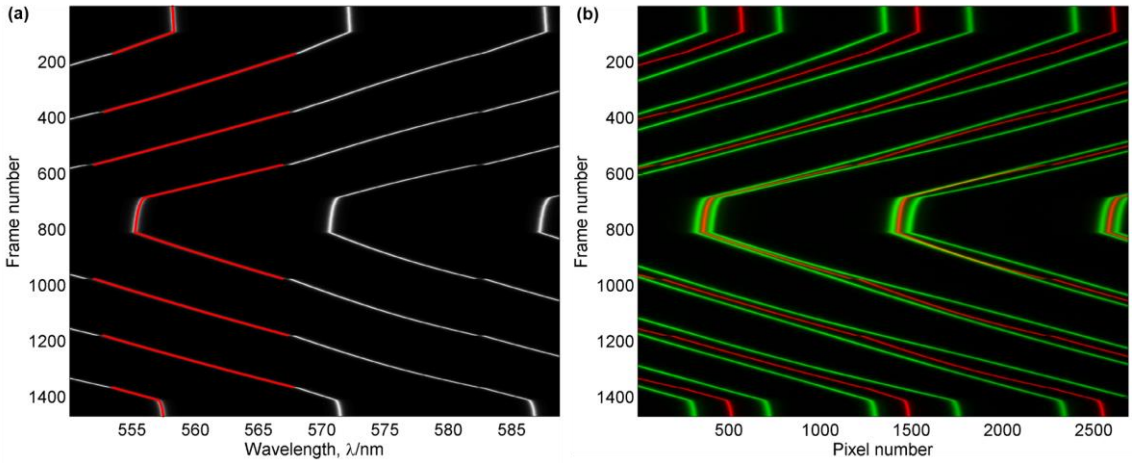

Figure 3.12 Spectrogram with the equivalent isotropic simulation based on Fig. 3.1a but with the wrong refractive index for distance profile, μ_o = 1.4, μ_e =1.5. (a) Isotropic spectrogram plotted with the average detected wavelengths in red lines. (b) Overlay of the simulated isotropic (red) and experimental (green) spectrograms.

3.3.5 Effect of chromatic order on isotropic equivalence

Fig. 3.13a shows the isotropic simulation based on the wrong sign of parity in Fig. 3.7a. Surprisingly, even the isotropic wavelength is different from the average detected one, which is because the generation of wavelengths does not take into account the sign of parity causing asymmetric inverted calculation. This isotropic simulation exactly reflects the abrupt shape of red distance profile in Fig. 3.7b, while Fig. 3.13b with the constant sign of parity shows significant match.

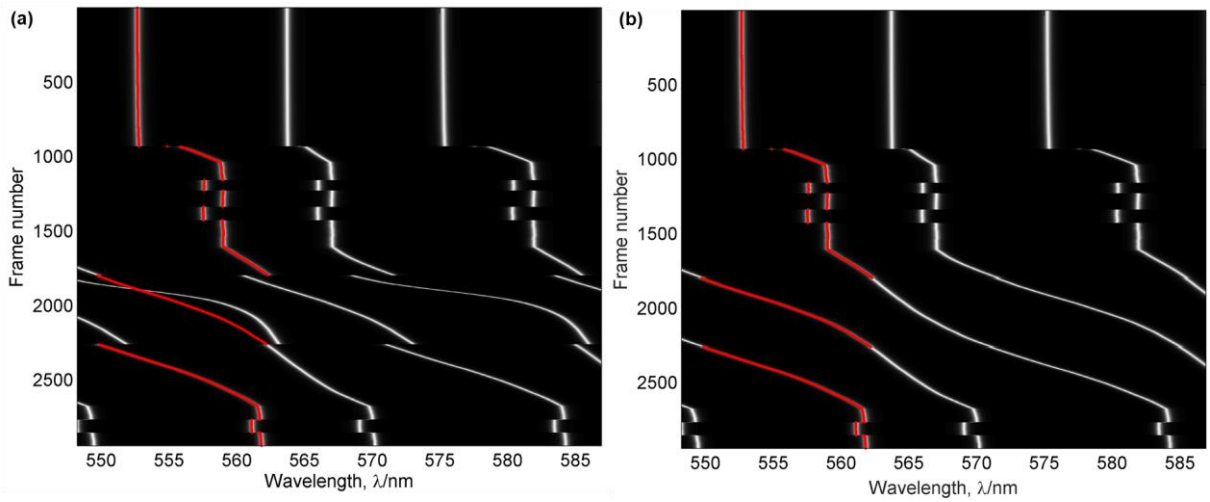

Figure 3.13 Spectrogram with the equivalent isotropic simulation based on Fig. 3.7b with different signs of parity for chromatic order. (a) Isotropic spectrogram with Fnum depending on the chromatic order, plotted with average detected wavelengths in red lines. (b) Isotropic spectrogram with Fnum = 1, plotted with average detected wavelengths in red lines.

3.3.6 Full-parameter simulation with isotropic medium

Given the difficulties mentioned in section 3.3.3 for the anisotropic medium, an isotropic medium is firstly used for simulation test only considering the birefringence of mica, shown in Fig. 3.14a, where the spectrogram shows a similar trajectory as the original data Fig. 3.6a with air medium. Further confirmation comes from the overlaid spectrogram in Fig. 3.14b by the simulation and experiment figures, where yellow thin lines sit in the

centre of thick green lines. This yellow colour is due to the mixture of red simulated lines and experimental green background, which means almost no deviation can be seen in the figure, thus the simulation for the isotropic medium works very well.

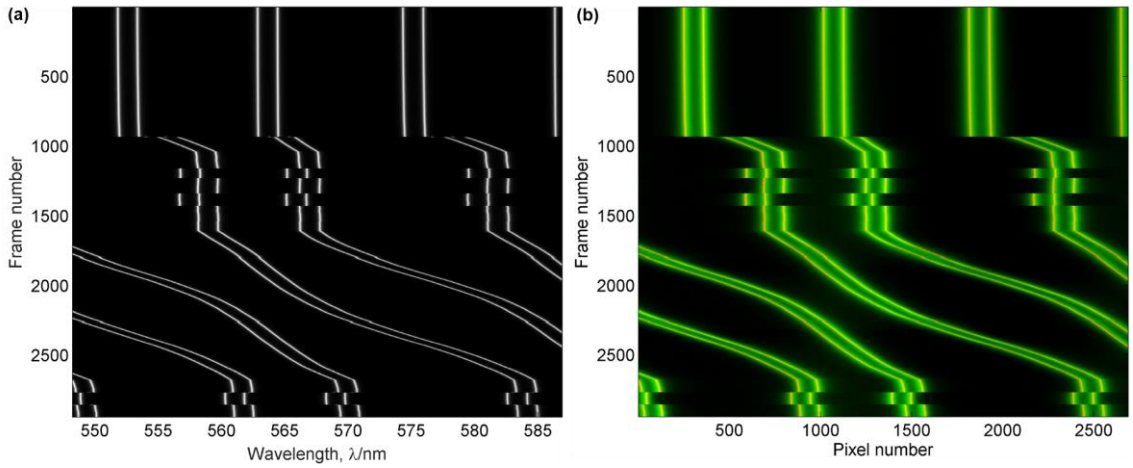

Figure 3.14 Full-parameter simulation for an experiment with air medium. (a) Simulation with the distance profile from Fig 3.10. (b) Overlay of simulation and experiment spectrograms with the ImageJ. The thick green line is experimental data from Fig. 3.6a, the thin red line is the simulation in (a), and the overlaid region shows yellow.

3.3.7 Full-parameter simulation with anisotropic medium

Finally the LC experiment in Fig. 3.3 is tested with a full-parameter simulation that takes into account the birefringence and rotational angles from both the mica and the LCs, as shown in Fig. 3.15a where the twist angle Φ = 13.2 °. The overlaid spectrogram by simulation and original data Fig. 3.1a is shown in Fig. 3.15b, where the green lines are from the experiment while the red lines are from the simulation. Yellow lines are the overlaid region, which is seen in most of the spectrogram. However, there are small deviations in the large distance both during the approach and retraction, which might be due to accumulated phase dispersion at the large distance or thermal fluctuations of the molecules that change either polar or azimuthal angles.

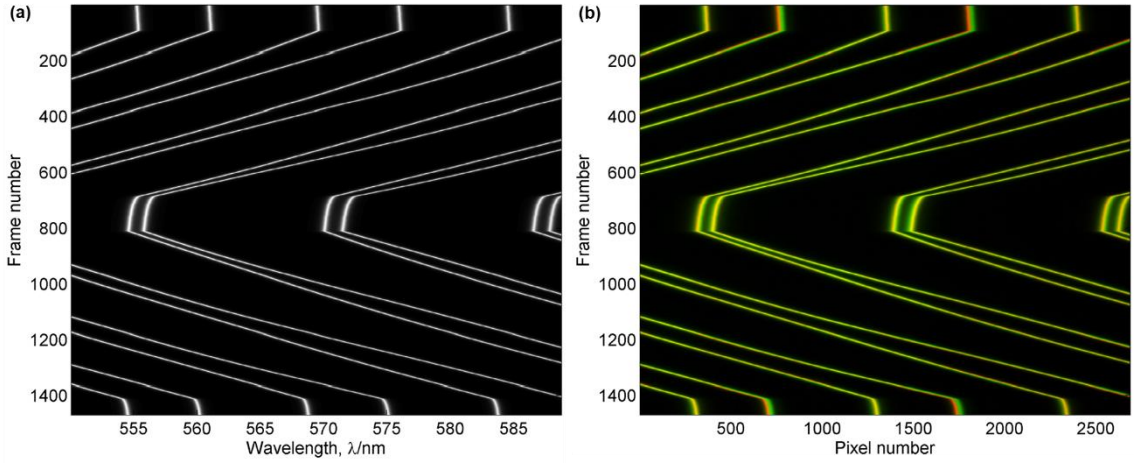

Figure 3.15 Full-parameter simulation for an experiment with the LCs. (a) Simulation with the distance profile from Fig 3.7, the twist angle of the LCs Φ = 13.2 ° with the configuration shown in Fig. 3.10a is adopted. (b) Overlay of the simulation and experiment spectrograms with the ImageJ. The thick green line is the experimental data from Fig. 3.6a, the thin red line is the simulation in (a), and the overlaid region shows yellow.

Fig. 3.16 shows a simulation with a different configuration shown in Fig. 3.10b where the twist angle of the LCs Φ = 73.2 °. There is a clear mismatch with experimental spectra, because crossings within doublets are produced at around frame 600, which is not the feature in Fig. 3.3. If Fig. 3.10 is carefully examined, one can find that the bisector of Φ is parallel with that of Ψ in Fig. 3.10a, while in Fig. 3.10b the bisector of Φ is perpendicular with that of Ψ. The splitting in these two configurations is consistent with the discussions in section 2.2.1. More detailed discussions about the effect of rotational angles among birefringent layers on the multiple-beam interferometry will be shown in section 3.3.8-3.3.12.

Overall, the full-parameter simulation well reconstructs the MBI spectra with different rotational angles of multiple birefringent layers confined in the SFA, which lays the foundation for the understanding of anisotropic optics.

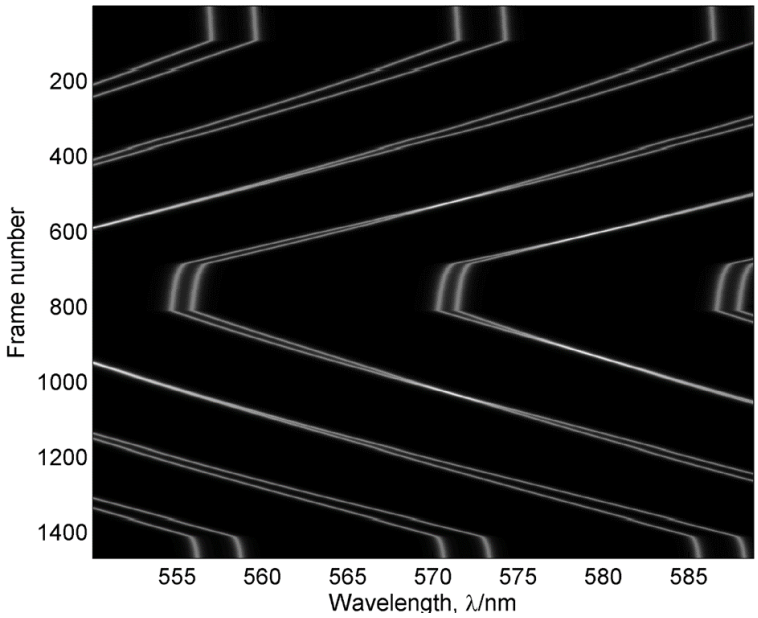

Figure 3.16 Full-parameter simulation showing the fringes as a function of frame number and wavelengths, with the distance profile from Fig 3.7. The twist angle of the LCs Φ = 73.2 ° with the configuration shown in Fig. 3.10b is adopted.

3.3.8 Effect of mica-mica intersection angle

Fig. 3.17a shows the spectrogram as a function of the intersection angle Ψ of the mica and wavelengths at zero surface separation, where more typical mica thickness Y = 3 μm and silver thickness 50 nm are used for the simulation. The prime fringe with the chromatic order q = 35 can be calculated with the method described in section C.3. Moreover, it can be seen that the splitting of the doublets maximize at Ψ = 0, minimizes to zero at $\Psi = \pm\frac{\pi}{2}$ and decreases with increasing the absolute value of Ψ, while the parity of the chromatic order does not affect the splitting behaviours. A magnified view of q-1 fringe is analyzed in Fig. 3.17b, where the dashed line is the average wavelength $\bar{\lambda}$ of doublet $\lambda_{q-1,1}$ and $\lambda_{q-1,2}$, also is the equivalent isotropic fringe based on the average refractive index. The solid lines follow the equation $\lambda = \bar{\lambda} \pm \frac{1}{2}\delta$ λc oΨs, or equation C.9

and 3.10 that are useful for calculating the intersection angle Ψ of the mica as well, where the maximum splitting $\delta\lambda = \lambda_{q-1,2} - \lambda_{q-1,1}$ when $\Psi = 0$. These calculations are consistent with previous analysis[170, 171].

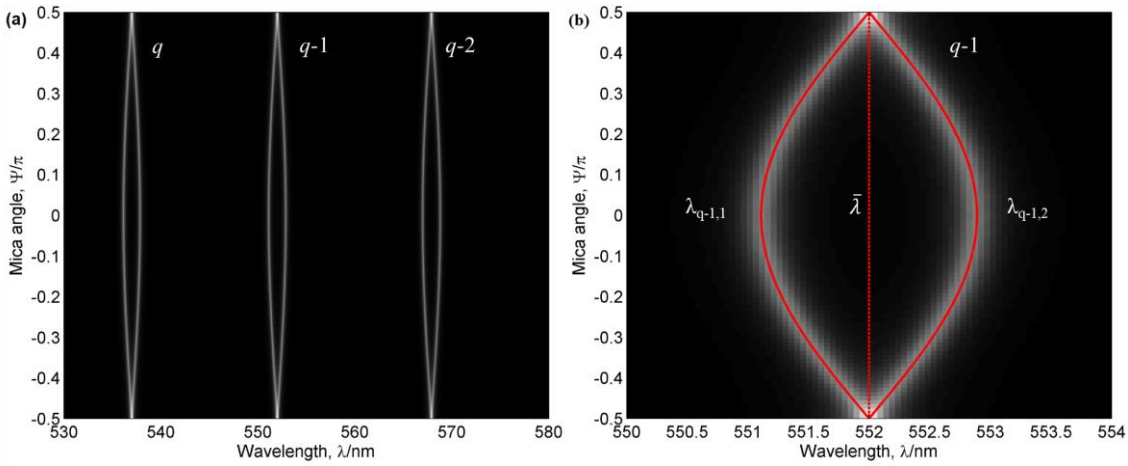

Figure 3.17 Simulation of spectra as a function of the intersection angle Ψ of the mica and wavelengths at the mica-mica contact. (a) Three fringes *q*, *q*-1, and *q*-2 at contact. (b) A zoom-in of *q*-1 fringe. The dashed line is the average fringe $\bar{\lambda}$ of the doublet $\lambda_{q-1,1}$ and $\lambda_{q-1,2}$, the solid lines are calculated with $\lambda = \bar{\lambda} \pm \frac{1}{2}\delta\lambda\cos\Psi$, where $\delta\lambda = \lambda_{q-1,2} - \lambda_{q-1,1}$ when Ψ = 0. Typical thicknesses of the mica and the silver layer, 3 μm and 50 nm respectively, are used for simulation.

With the injection of the LCs, the effect of the intersection angle of the mica is expected to be more complicated. Fig. 3.18 shows a simulation of fringes as a function of the surface distances and wavelengths for the confinement of the LCs in different setups of intersection angles Ψ of the mica and azimuthal angles φ. For simplicity, the most common LCs 5CB is used, special angles 0 or π/2 are applied, and the easy axis is fixed in one direction that will not cause any twist distortion of the molecules. Overall, three fringes *q*, *q*-1, and *q*-2 shift from contact position to longer wavelengths as the distance *D* is increased, with different splitting caused by the relative angles between the mica and the LC director. Fig. 3.18a,b correspond to the discussions of crossings within doublets

in section 3.3.7 due to parallel or perpendicular configurations, while in Fig 3.22c,d, equal-thickness mica surfaces cancel each other's birefringence leaving 0 splitting at contact. In this particular case, the azimuthal angle φ of the LCs is not important anymore and the effective birefringence of the whole system is purely from the LCs resulting in identical splitting behaviours φ. Particularly, odd fringes *q* and *q*-2 keeps the 0 splitting much further free from the influence of medium than even fringe.

3.3.9 Effect of azimuthal angle of liquid crystals

Here the intersection angle of the mica is fixed to $\Psi = \pi/3$ but changing the azimuthal angle φ of the 5CB without any twist shown in Fig. 3.19, where the overall splitting in Fig. 3.19a-c similarly increases with the distance while the splitting, for example, *q*, becomes smaller. The splitting depends on the parity of the chromatic order and the odd fringes are less affected by the medium at the small distance with increasing φ. Additionally, the crossing within doublet happens only in the case where the director is perpendicular to the bisector of Ψ. The effective birefringence of the mica is totally cancelled by birefringence of the LCs at the crossing point.

Fig. 3.19 gives an overview of how azimuthal angles affect the splitting behaviours, but it is difficult to compare this effect cross figures. In order to examine carefully, a few specific distances are selected to highlight the evolution of the doublet splitting as a function of the azimuthal angle for the odd and even fringes shown in Fig. 3.20, where the spectra are a function of the azimuthal angle φ and the wavelengths λ. On the whole, three fringes *q*, *q*-1, and *q*-2 move to longer wavelength and larger splitting at the further distance and therefore spectra at large D = 1000 nm show higher orders *q*+6, *q*+5, and *q*+4. Moreover, the average wavelength in the red dashed line is straight, which is

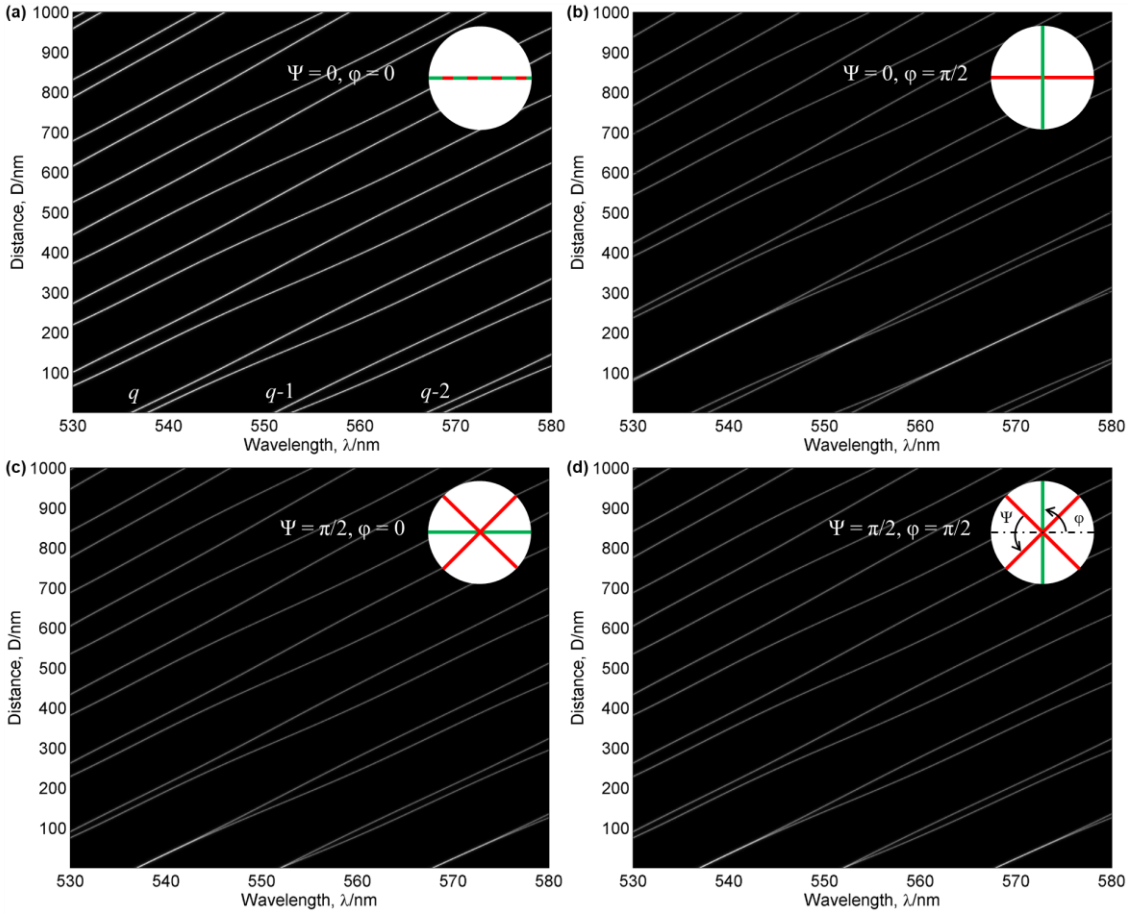

Figure 3.18 Simulation of fringes as a function of the surface distances and wavelengths with different intersection angles Ψ of the mica and azimuthal angles φ of the LCs. (a) Ψ = 0, φ = 0 (b) Ψ = 0, φ = π/2. (c) Ψ = π/2, φ = 0 (d) Ψ = π/2, φ = π/2. The inserted panels show the index axes of mica γ and the easy axis for molecular director **n**, in red and green line respectively, where Ψ is the acute intersection angle between the γ axes, φ is the azimuthal angle to the black centre line direction. The refractive indices of 5CB are used for the simulation assuming that only one easy axis without a twist is confined in the separation for simplicity. All other configurations are the same as the case shown in Fig. 3.17 with three fringes, *q*, *q*-1, and *q*-2 at contact.

consistent with the equivalent isotropic assumption without noticeable deviations. At *D* = 3 nm, the effective birefringence from the LCs is so small that the effect of the azimuthal angle cannot be clearly seen on the scale of the spectrogram, meaning the mica dominates the birefringence. At *D* = 10 nm, the odd fringes *q* and *q*-2 are not sensitive to

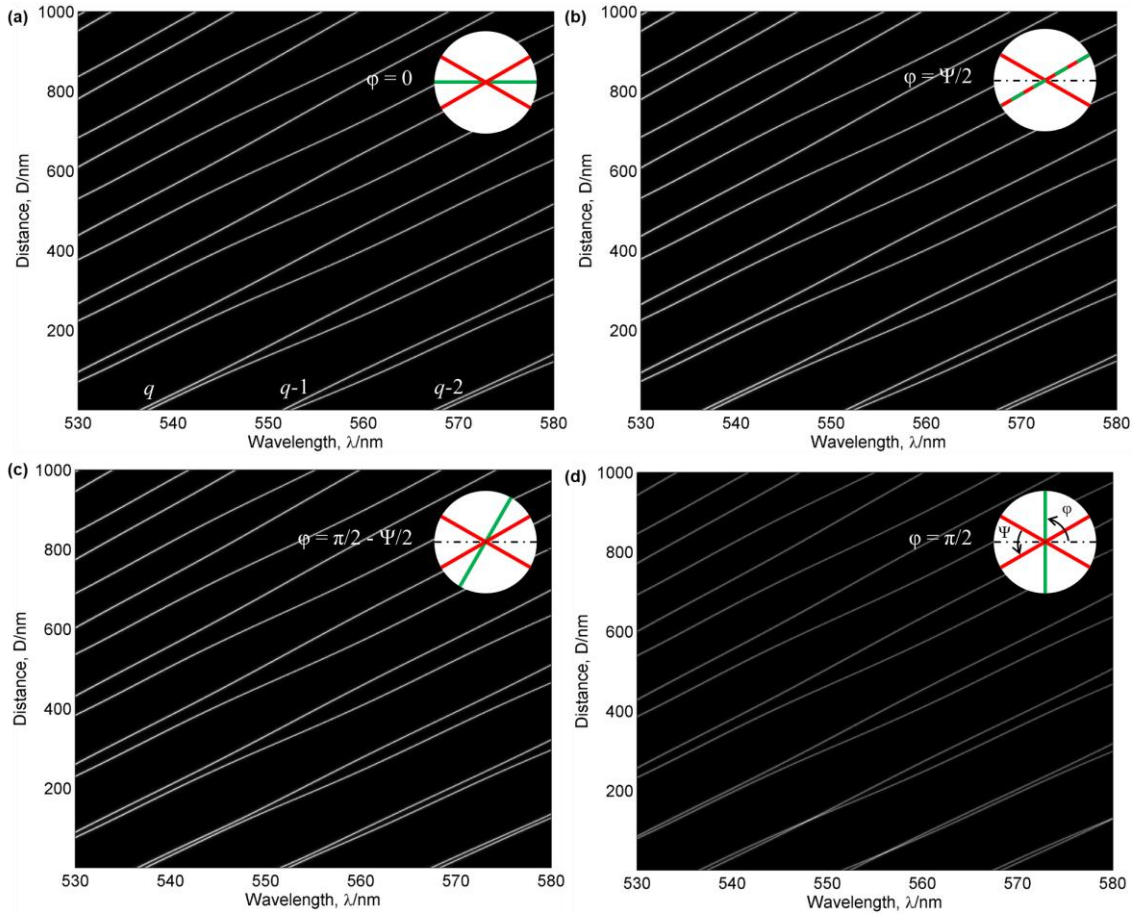

Figure 3.19 Simulation of spectra as a function of the surface distances and wavelengths with fixed intersection angle $\Psi = \pi/3$ of the mica and different azimuthal angles φ of the LCs. (a) $\varphi = 0$. (b) $\varphi = \Psi/2$. (c) $\varphi = \pi/2 - \Psi/2$. (d) $\varphi = \pi/2$. The inserted panels show setups of index axes of the mica γ and the easy axes for molecule direction **n**, in red and green lines respectively, where Ψ is the acute intersection angle between the γ axes, φ is the azimuthal angle to the black dot-dash line direction. All other configurations are the same as the case shown in Fig. 3.18 with three fringes, *q*, *q*-1, and *q*-2 at contact.

the rotation of medium whereas the splitting of even fringe *q*-1 starts to decrease with increasing the azimuthal angle φ. By contrast, at $D = 100$ nm, the splitting of all fringes are decreasing with the increase of the azimuthal angle φ, likewise, the even fringes are more sensitive than the odd ones. At $D = 1000$ nm, the splitting reduces at larger

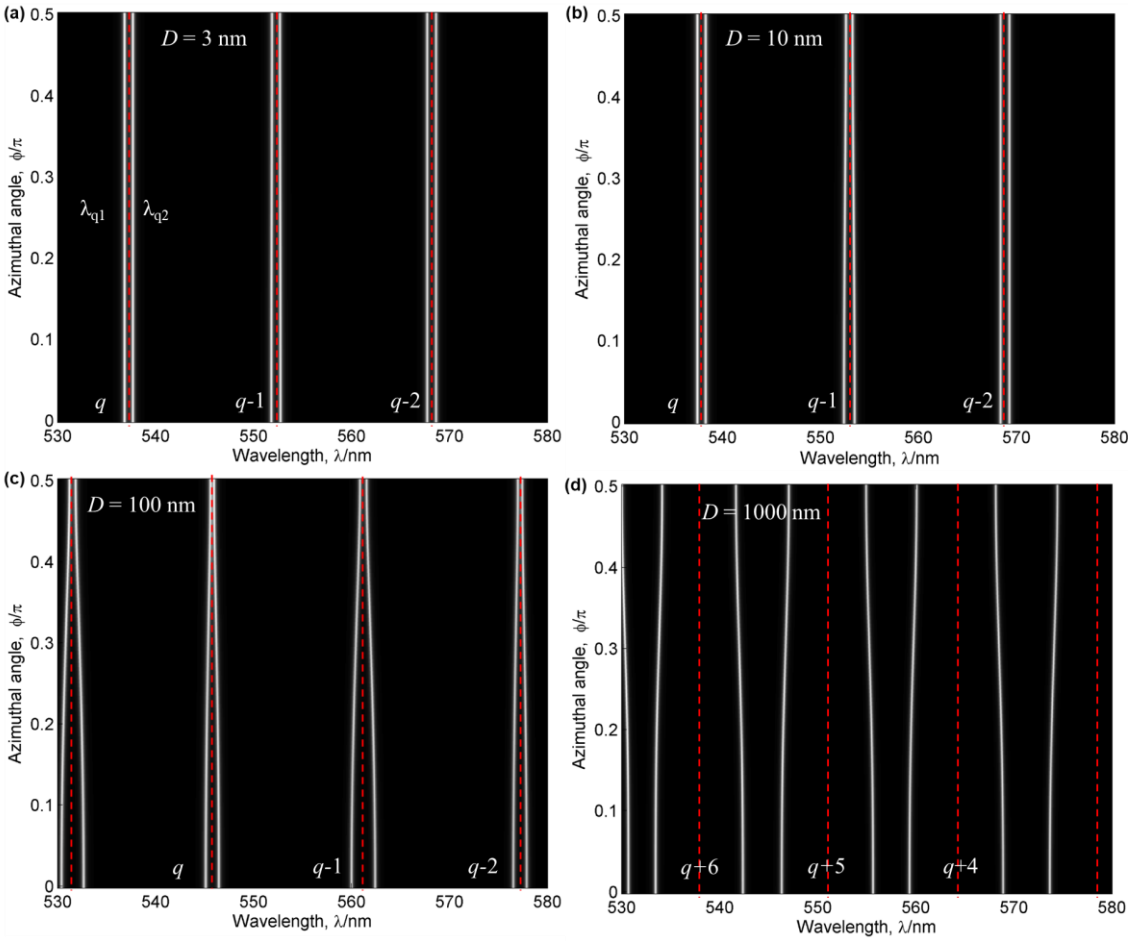

Figure 3.20 Simulation of fringes as a function of azimuthal angles φ and wavelengths λ at different distances. (a) D = 3 nm. (b) D = 10 nm. (c) D = 100 nm. (d) D = 1000 nm. Fringes at contact q, q-1, and q-2 shift to longer wavelengths with increasing distances, consequently at D = 1000 nm, fringes q+6, q+5, and q+4 are seen in the given wavelengths. Wavelengths λ_{q1} and λ_{q2} are the two wavelengths of the prime fringe q, the red dashed lines are the average wavelengths $\bar{\lambda}$ of the doublets. All other configurations are the same as Fig. 3.19.

azimuthal angle φ, which are similar in all fringes indicating the LCs dominate the effective birefringence.

3.3.10 Effect of twist angle of liquid crystals

In real experiments, the mismatch of easy axes between the bottom and top mica surfaces tends to create twist distortion of the LCs in the gap. Furthermore, some LCs, such as cholesterics, smectic C, and some chiral materials are naturally twisted and exhibit an optical rotatory power. Here we use a fixed intersection angle $\Psi = \pi/3$ of the mica and the azimuthal angle $\varphi = 0$ for the average director across the LC film but we vary the total twist angles Φ of the LCs to simulate spectra as a function of the surface distances D and the wavelengths λ shown in Fig. 3.21, with three fringes, q, q-1, and q-2 at contact. Overall, the increase of the twist angles Φ makes intro-doublet crossings in the spectra of both the odd and even fringes shown in Fig. 3.21a-c. These crossing events happen repeatedly at a larger distance and, as a result, the splitting is much smaller than that in Fig. 3.21a where the twist angle $\Phi = \Psi$ is smallest and no crossing is observed in the given scope. Interestingly, the optical bandgap appears between wavelengths $\lambda_o = 2\pi\mu_o D/\Phi$ and $\lambda_e = 2\pi\mu_e D/\Phi$, highlighted with red lines in Fig. 3.21 and becomes larger with increasing the twist angle.

More details about the effect of the twist angle Φ of the LCs on the fringe splitting at specific distances are shown in Fig. 3.22 where the spectra calculated are a function of the twist angles Φ and the wavelengths λ. Overall, fringes shift to larger wavelengths with q, q-1, and q-2 at small distances, fringes q+3, q+2, and q+1 at D = 500 nm and fringes q+6, q+5, and q+4 at D = 1000 nm in the given wavelength span. The splitting dramatically changes with increasing the twist angle especially at large distances 500 and 1000 nm where multiple crossings appear and more crossings are seen in odd fringes and at a later distance. In particular, at D = 10 nm, odd fringes q and q-1 are not sensitive to twist angles consistent with the previous analysis about the effect of the medium at small distances, while the splitting of even fringe q-1 decreases then keeps constant with

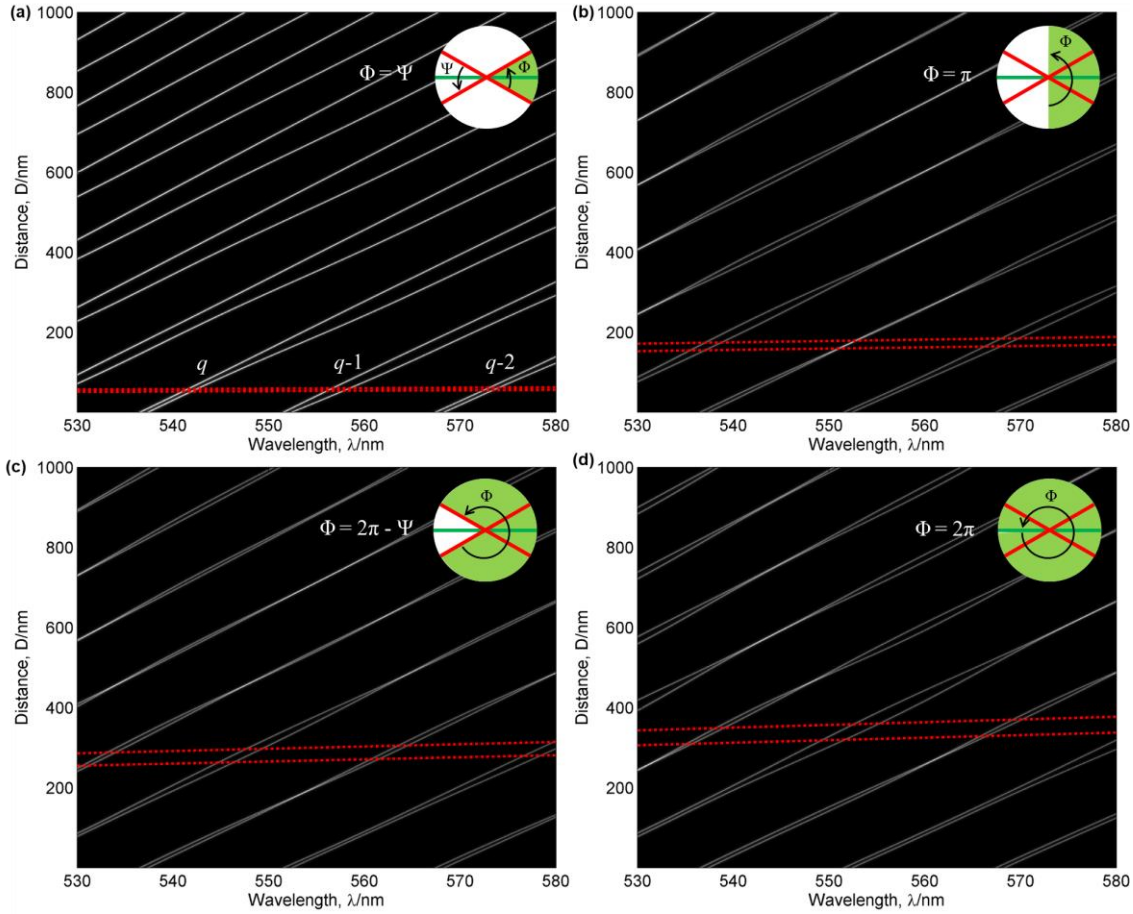

Figure 3.21 Simulation of spectra as a function of surface distances D and wavelengths λ with the fixed intersection angle $\Psi = \pi/3$ of mica, the azimuthal angle $\varphi = 0$ and different twist angles Φ of the LCs. (a) $\Phi = \Psi$. (b) $\Phi = \pi$. (c) $\Phi = 2\pi - \Psi$. (d) $\Phi = 2\pi$. The inserted panels show the setups of index axes of the mica γ and the bisector of shaded twist angle Φ, in red and green lines respectively. The regions between two dot-dash lines are optical bandgaps. All other configurations are the same as the case shown in Fig. 3.19 with three fringes, *q*, *q*-1, and *q*-2 at contact.

increasing the twist angle. At D = 100 nm, splitting of both the odd and even fringes varies with the twist angle, still, the even fringes are more sensitive to twist angles. At D = 500 and 1000 nm, multiple crossings appear without a clear periodicity, and the two fringes of a doublet start moving asymmetrically with respect to the centre on account of wavelength-dependent refractive index or phase change and dispersion. In other words, the average wavelength of a doublet varies with the twist at a large distance, indicating

visible deviations of isotropic equivalence. Additionally, the bandgap appears between red centre lines with the twisted LCs in Fig. 3.22a-c, whereas it falls outside the scope of given twist angles and wavelengths in Fig. 3.22d.

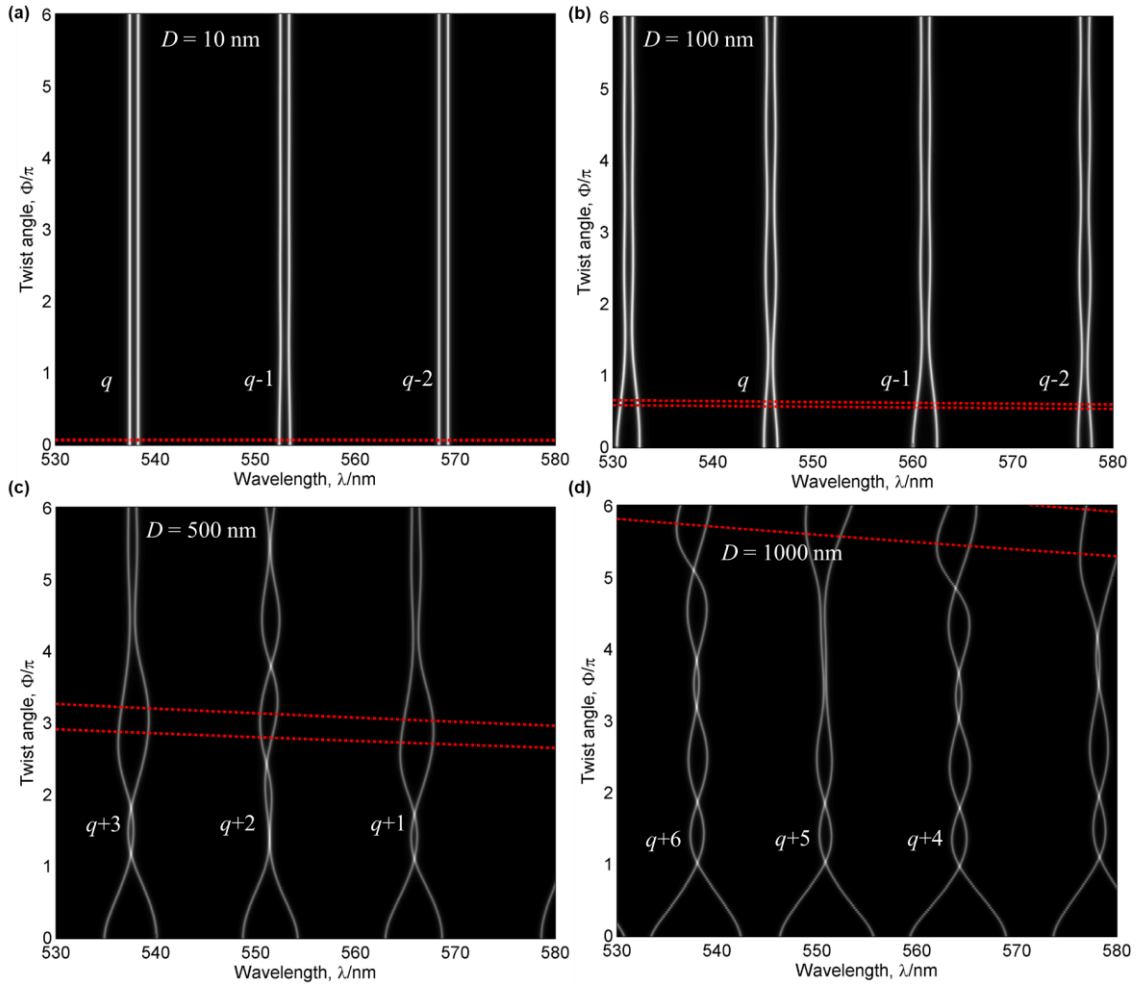

Figure 3.22 Simulation of fringes as a function of twist angles Φ and wavelengths λ at different distances. (a) D = 10 nm. (b) D = 100 nm. (c) D = 500 nm. (d) D = 1000 nm. The regions between the red centre lines are the bandgap. All other configurations are the same as Fig. 3.21.

3.3.11 Deviation of isotropic equivalence

As is mentioned above, the azimuthal angle φ causes non-noticeable deviations from isotropic equivalence in Fig. 3.20 but the twist angle Φ induces noticeable deviations to

the isotropic equivalence in Fig. 3.22. In this section, the quantitative comparison will be given to highlight the effect of the azimuthal angle φ and the twist angle Φ on the deviation. With the fixed intersection angle Ψ = π/3 of mica, deviation of average wavelength $\bar{\lambda}$ and equivalent isotropic wavelength λ_i is shown in Fig. 3.23 for various distances and azimuthal angles φ as a function of the wavelengths λ. Overall, the deviation of wavelengths is small but increases with increasing distances. Moreover, the deviations on the even and odd fringes are more or less symmetric but with the axis of symmetry fluctuating either positive or negative. Specifically, at D = 10 and 100 nm, twist angles Φ = π and 2π disturb the deviation largely with changing the azimuthal angle φ compared to the Φ = 0 case. To the contrary, at distance D = 1000 nm, twist angle Φ = π and 2π minimize the deviation.

In the equivalent isotropic simulation, the average refractive index of 5CB about 1.6 is very close to that of the mica and the silver mirror is assumed as a perfect mirror. As a result, the phase dispersion and phase change at the interfaces are negligible. The wavelength of fringes follows equation, $2\mu D + 4\mu_{mi\ c}Y_a = q\lambda_q^i$, where μ is the average refractive index of the medium, λ_q^i is the isotropic wavelength at the chromatic order q. The deviation of distance calculated by the average and isotropic wavelengths is $\delta D = \frac{\delta\lambda(\mu D + 2\mu_{mi\ c}Y_a)}{\bar{\lambda}\mu}$, where $\delta\lambda$ is the deviation of the average wavelength from the equivalent isotropic wavelength. In Fig. 3.23 at D = 10 nm, $\delta\lambda$ < 0.00 05 nm, δD < 0.005 nm, at D = 100 nm, $\delta\lambda$ < 0.005 nm, δD < 0.5 nm, at D = 1000 nm, $\delta\lambda$ < 0.2 nm, δD < 2.5 nm. All the errors $\delta D/D$ are in the order of 10^{-3}, showing that the isotropic equivalence for different azimuthal angles φ is accurate enough for the typical SFA experiments.

With the fixed mica intersection angle Ψ = π/3 of the mica and the azimuthal angle φ =

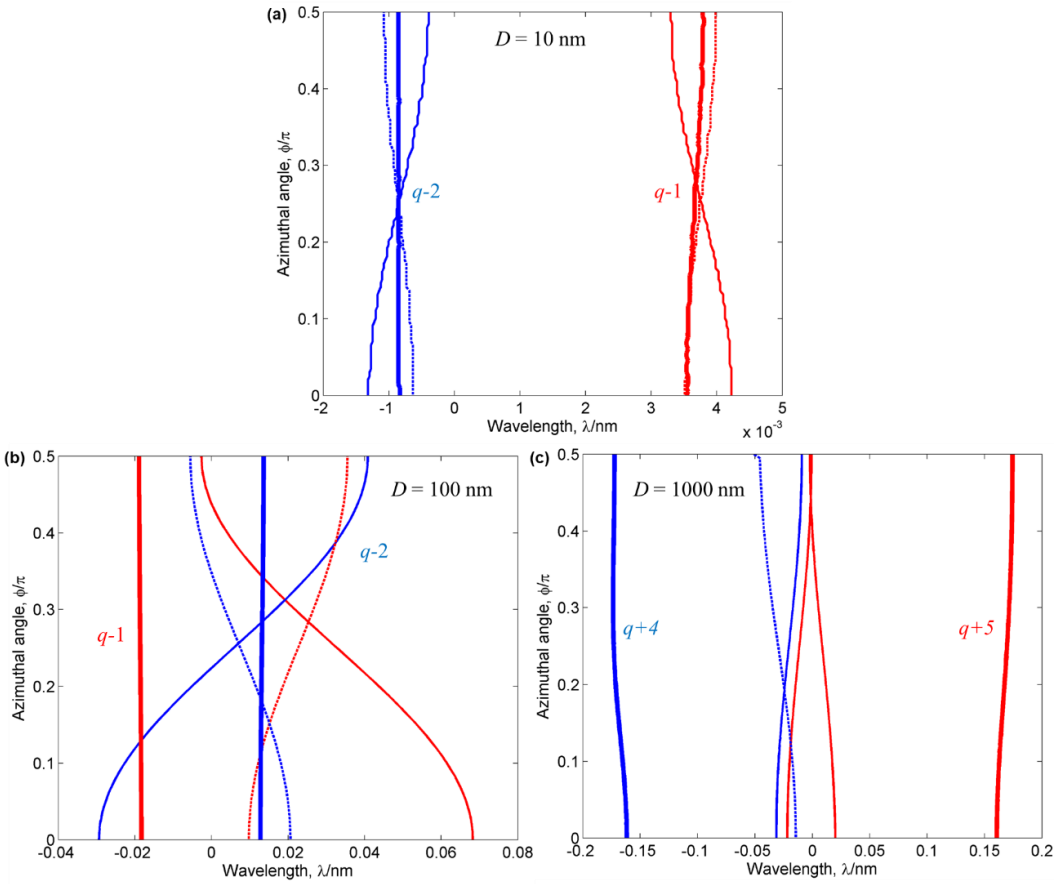

Figure 3.23 Deviation of the average wavelengths $\bar{\lambda}$ and the equivalent isotropic wavelengths λ_i as a function of the bisector of azimuthal angle φ and the wavelength λ with the fixed intersection angle $\Psi = \pi/3$ of mica, different distances D and twist angles Φ. (a) D = 10 nm, fringe q-1 and q-2 are compared. (b) D = 100 nm, fringe q-1 and q-2 are compared. (c) D = 1000 nm, fringe q+5 and q+4 are compared. The blue color is for odd fringes while the red color is for even fringes. The thick, thin and dot lines are corresponding to $\Phi = 0$, π and 2π respectively. All other configurations are the same as the case shown in Fig. 3.21.

0, the deviation of the average wavelengths $\bar{\lambda}$ from the equivalent isotropic wavelengths λ_i as a function of the twist angles Φ and wavelengths λ at two specific distances 100 and 1000 nm is shown in Fig. 3.24. Generally, the deviation is small but increases with increasing distance, which is very similar to the case shown in Fig. 3.23. However, the roughly symmetric deviation for the odd and even fringes fluctuates much more

dramatically with the increase of twist angle Φ than for the change of the azimuthal angle φ. Especially, the deviation maximizes in the bandgap regions at both distances shown in Fig. 3.24. At D = 100 nm, $\delta\lambda <$ 0.08 nm, $\delta D <$ 0.9 nm; at D = 1000 nm, $\delta\lambda <$ 0.8 nm, $\delta D <$ 10 nm, with errors $\delta D/D$ in the order of 10^{-2} which is acceptable in the SFA experiments.

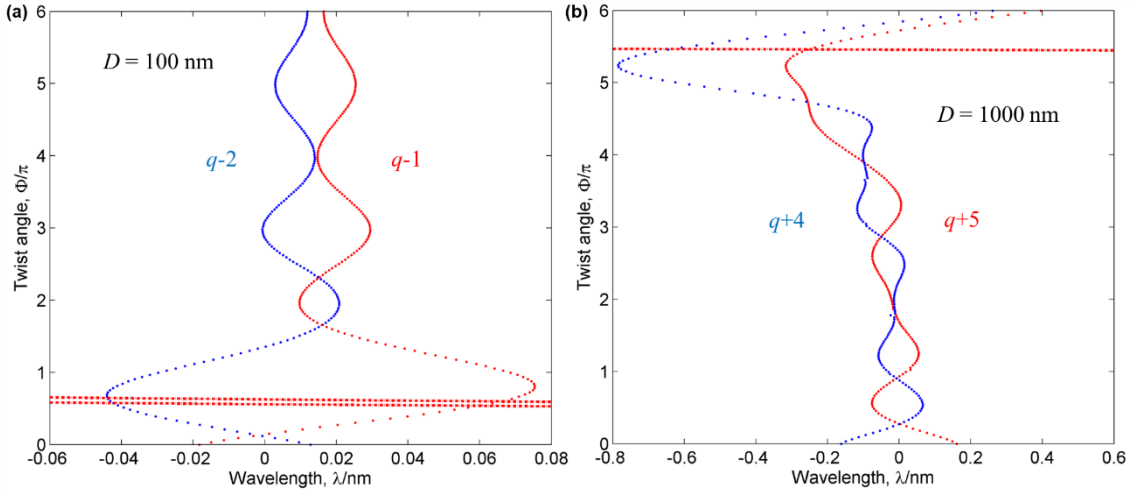

Figure 3.24 Deviation of the average wavelength $\bar{\lambda}$ from the equivalent isotropic wavelength λ_i as a function of twist angles Φ and wavelengths λ with the fixed intersection angle $\Psi = \pi/3$ of the mica, the azimuthal angle $\varphi = 0$ and different distances D. (a) D = 100 nm, fringe q-1 and q-2 are compared. The region between the red dot-dash lines is approximate bandgap. (b) D = 1000 nm, fringe q+5 and q+4 are compared. The region above the red dot-dash line is approximate bandgap. The blue dot line is for odd fringe while the red dot line is for the even fringe. All other configurations are the same as the case shown in Fig. 3.21.

When the twist angle is very small, in other words, the corresponding pitch of the twisted structure is much larger than the observed wavelength λ, the medium is similar to the nematics confined in the gap, called Mauguin limit[2], where the deviation of isotropic equivalence is the same as the case in Fig. 3.23 with small error $\delta D/D$ in order of 10^{-3}. By contrast, in the opposite limit, when the pitch is much smaller than the observed

wavelengths λ, the twisted structure is basically isotropic medium[2] and the deviation from isotropic equivalence is minimum. For instance, there is a trend of deviation decreasing in Fig. 3.24a, where the pitch is 33 nm with the twist angle 6π in 100 nm confinement. In the region where the bandgap exists, the medium cannot be seen as isotropic, bringing about the Bragg reflections, which induces large deviation $\delta D/D$ in the order of 10^{-2} with the isotropic equivalence shown in Fig. 3.24.

3.3.12 Resolution of MBI on molecular orientation

In order to examine how sensitive the MBI is to the molecular orientation, namely to what extent the SFA can be used to detect molecular orientation, we performed simulations of fringes as a function of the azimuthal angle φ or the polar angle θ at extreme confinement D = 3 nm with typical setup of the SFA shown in Fig. 3.25. Given that the odd fringe is not sensitive to the medium at such distance, only even fringe q-1 is simulated. Firstly, with the fixed polar angle θ = π/2 and different intersection angles Ψ of the mica, the effect of the azimuthal angle φ is shown in Fig. 3.25a-c, where generally the splitting of fringe decreases with increasing the intersection angle Ψ and the azimuthal angle φ, although the splitting is less sensitive to the latter angle. When Ψ = π/2, the splitting is zero and not affected by the azimuthal angle φ. Those changes of splitting with the azimuthal angle are small but still detectable with a standard spectrometer having a wavelength resolution of the order of 10^{-1} nm. Following this, with the fixed azimuthal angle φ = 0 and different intersection angles Ψ of the mica, the effect of the polar angle θ is shown in Fig. 3.25d-f, where the splitting of fringe decreases with increasing the intersection angle Ψ but with the decrease of the polar angle that only affects the ray experiencing the extraordinary index of 5CB changing with the polar angle. The change

of this ray, which is also in the order of 10^{-1} nm on the wavelengths, can be observed on the optics even when $\Psi = \pi/2$.

For 5CB that is uniaxial LC, refractive indices can be described by a geometric ellipsoid, called index ellipsoid[168], where the ordinary index will not change with the orientation of molecule either the azimuthal angle φ or the polar angle θ but the extraordinary index changes with the polar angle θ. The corresponding extraordinary index $\mu_e(\theta)$ follows,

$$\frac{1}{\mu_e^2(\theta)} = \frac{\cos^2\theta}{\mu_0^2} + \frac{\sin^2\theta}{\mu_e^2} \tag{3.1}$$

where $\theta = \pi/2$, $\mu_e(\pi/2) = \mu_e$ corresponding to the planar anchoring, while $\theta = 0$, $\mu_e(0) = \mu_o$ corresponding to the homeotropic anchoring.

3.4 Summary

In this chapter, the optics generated by multiple-layer birefringent materials through the multiple-beam interferometry is analysed based on the assumption that the average wavelengths of fringes are equivalent to the optics produced by the isotropic media with average refractive indices. Additionally, the simulation through a 4x4 matrix well reconstructs the experimental optics and confirms the isotropic equivalence assumption with negligible errors. Some conclusions are obtained as following,

(1) The fringe behaviours, such as the splitting, crossing and red-shift with the distances, are affected by the birefringence, refractive index and parity of chromatic order of medium as well as the relative angle between multiple layers.

(2) The distance profile at large distances can be calculated with the fringes in different chromatic orders by taking into account the relative chromatic order to the prime

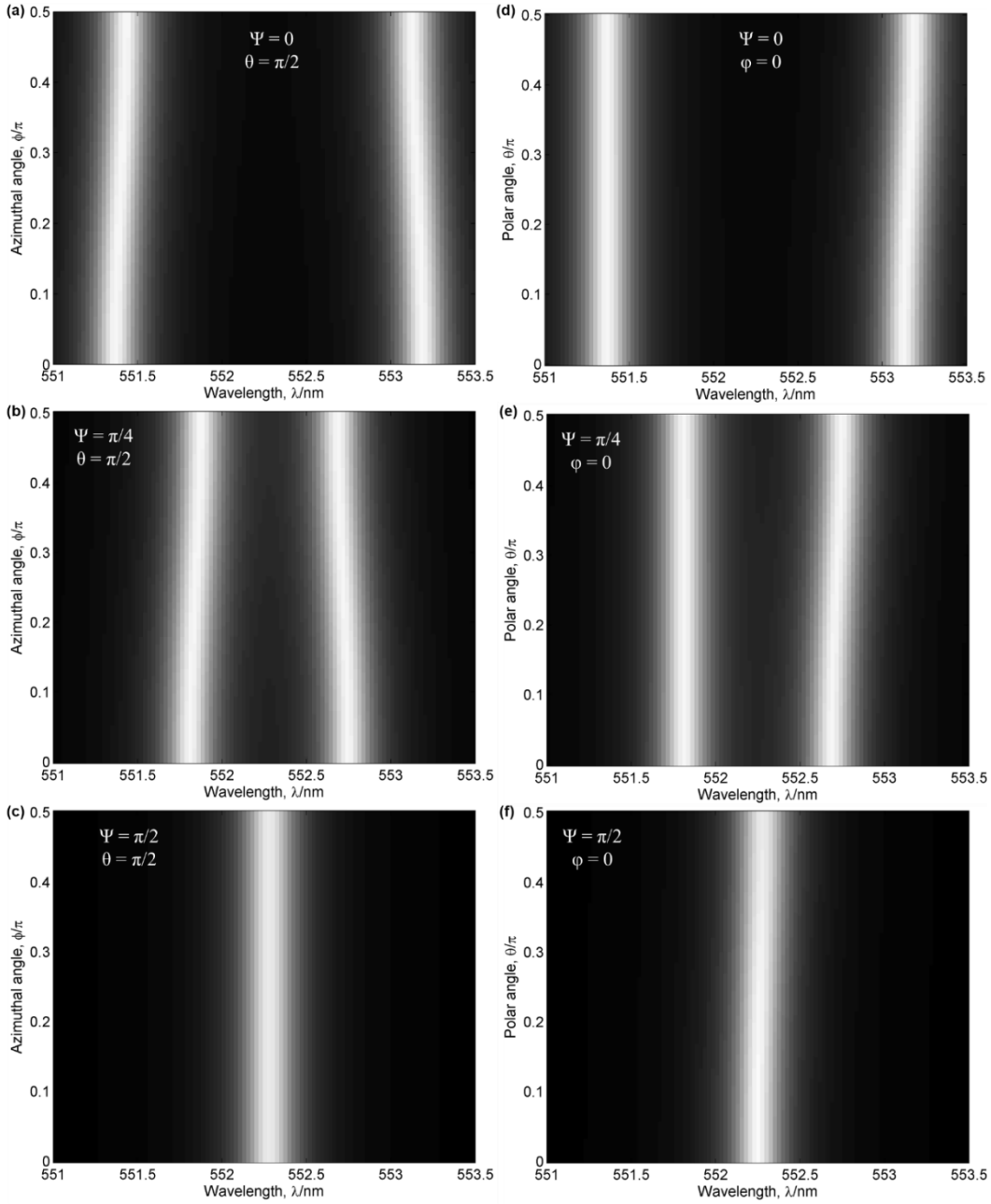

Figure 3.25 (a-c) Simulation of fringes as a function of the azimuthal angles φ and the wavelengths λ with the fixed polar angle θ = π/2, distance *D* = 3 nm and different intersection angle Ψ of the mica. (a) Ψ = 0. (b) Ψ = π/4. (c) Ψ = π/2; (c-f) Simulation of fringes as a function of the polar angle θ and the wavelength λ with the fixed azimuthal angle φ = 0, distance *D* = 3 nm and different intersection angles Ψ of the mica. (d) Ψ = 0. (e) Ψ = π/4. (f) Ψ = π/2. All other configurations are the same as the case shown in Fig. 3.19 with fringe *q*-1 at given wavelength range.

fringe, such that it narrows the analysis range of wavelengths decreasing the errors of wavelength-dependent refractive indices. The sign of chromatic parity in the calculation is only determined by the parity of the prime fringe.

(3) The refractive index mismatch between the medium and the mica magnifies the errors calculated by the wrong sign of chromatic parity.

(4) The adoption of the wrong refractive index of medium does not affect the isotropic equivalence of detected experimental fringes that are used for distance calculation, but affects the non-detected region. The larger refractive index shifts the simulated fringes to longer wavelengths compared with the experimental ones in this region, *vice versa*.

(5) When the intersection angle of the mica $\Psi = \pi/2$, the birefringence of mica is practically cancelled, as a result, the optics of the medium is not affected by the azimuthal angle φ.

(6) The crossing within a doublet happens only when the azimuthal angle of the nematic LCs $\varphi = \pi/2$, where the phase retardation between two rays experiencing the refractive index of the mica μ_β and μ_γ is zero, which is cancelled by the LCs. This crossing signature is used for determining the easy axis distribution of the LC anchoring.

(7) The twist angle of the LCs Φ induces repeated crossings within the doublets and forms the bandgap.

(8) The deviation of the equivalent isotropic simulation and the average wavelength is small and mainly affected by the twist angle Φ. For different azimuthal angles φ, the errors $\delta D/D$ are in the order of 10^{-3} with typical distances, while the errors $\delta D/D$,

maximizing at the bandgap region, are in the order of 10^{-2} with different twist angles Φ, which is acceptable in the SFA experiments.

(9) The resolution of the spectrometer is sufficient to detect the optics changed by the orientation of the molecules with different azimuthal angles φ or polar angles θ at the nano-confinement as small as 3 nm.

4 Twist transitions and equilibrium forces in cholesterics

4.1 Introduction

It has been shown in section 1.2 that cholesterics selectively reflect light causing bandgaps that are tuneable for numerous optical and thermal applications. The cholesteric-nematic transitions by magnetic, electric field or stress have attracted much attention, but how the anchoring influences the transition and how stresses deform cholesterics other than cholesteric elastomers[58] are still not well understood. This chapter is using the SFA to investigate the optical and mechanical responses during the retraction of the surface with a quasi-static velocity that is similar to equilibrium status. Under the SFA confinement, the geometry is described by equation 2.1 forming circular defects, as shown in section 2.3.5. The cholesteric layers with the period equal to half-pitch p with π rotation are integrally distributed in the SFA under planar anchoring shown in Fig. 4.1, where $h_{0,n} = np$ is the height of the relaxed n layers if there is no mismatch of the easy axes on top and bottom mica. Because of the integral transition a defect forms between n and n+1 layers at a surface separation distance $h_{d,n}$ corresponding to a lateral radius $r_{d,n}$. When the surfaces are retracted, those defects shrink towards the circular centre and eventually disappear one by one, during which the optics and forces can be analysed simultaneously.

4.2 Analysis of multiple-beam interferometry

As shown in section 3.3.10, the twist angle Φ affects fringe behaviours on the splitting

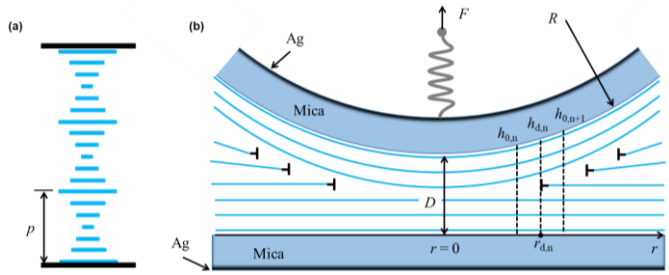

Figure 4.1 Schematic diagram of cholesterics under the confinement. (a) The periodical layers have half-pitch p, with molecules rotating by π, confined between two plates. (b) Cross-section of cholesterics confined between the two crossed cylinders with the radius R. One of the cylinders is connected with the spring experiencing force F. The contact position with the radius $r = 0$ is separated at distance D. The cholesterics form a defect at the distance $r_{d,n}$, where the distance separation is $h_{d,n}$, between two integer layers with the distance $h_{0,n}$ and $h_{0,n+1}$. The blue lines are the layers of cholesterics, the black "T" symbol indicates a dislocation defect.

and crossings, but it has been proved that the error $\delta D/D$ on the surface separation distance calculated by isotropic equivalence is within the order of 10^{-2}. Cholesterics, 62.4 wt% nematics QYPDLC-036 (similar to the BL036 with low temperature sensitivity from Merck) and 37.6 wt% chiral dopant R2011 purchased from Qingdao QY LC Co., Ltd (Chengyang China), confined in the SFA shows natural periodical twists and defects which may produce more intriguing phenomena. The fringes after injection of cholesterics are shown in Fig. 4.2. In Fig. 4.2a which is close the surface contact before the last layer of cholesterics being squeezed out, the fringes are not special compared with those in nematics shown in Fig. C.4b. After squeezing out the last layer, special transitions on even fringes q-1 and q-3, which are sensitive to medium, show up, corresponding to the first circular defect. This defect circle is usually non-integer layer of half-pitch with rotation angle less than π due to the mismatch of the easy axes for the anchoring on the mica surfaces, thus the intrinsic total twist angle $\Phi_0(n_0) = \alpha + n_0\pi$, where

α is the intersection angle of the easy axes, namely the non-integer layer; n_0 is the number of half-turns. When the intersection angle is acute, n_0 starts from 0, while it is an obtuse angle, α becomes a negative acute angle with n_0 starting from 1. Theoretically, all the defect circles can be seen from a single fringe, but at a far distance, the lateral resolution of the microscope is not enough to distinguish.

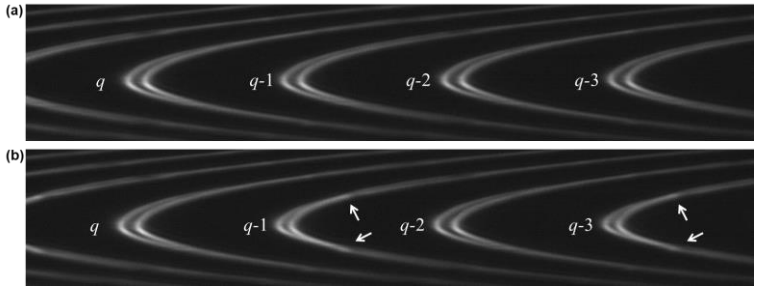

Figure 4.2 Snapshots of fringes *q*, *q*-1, *q*-2 and *q*-3 after injection of cholesterics near contact position. The fringe *q* is odd chromatic order selected as the prime fringe. The fringes (a) before and (b) after squeezing out of the last layer of cholesterics. The arrow indicates the position of the defect.

When the surfaces are retracted gradually, the layers of cholesterics are stretched until one more layer slips in, during which the defects are expected to shrink and the twist transitions happen. Fig. 4.3b shows the snapshot of the annihilation of the defect in the fringe *q*+3, appearing as the collapse of splitting compared with the fringes at the contact position in Fig. 4.3a. Fig. 4.3c is the spectrogram fringes during the retraction of the surface. During retraction with constant motor speed, the surface suddenly jumps out at frame 500 by overcoming the van der Waals attraction then moves almost linearly with some oscillations. The splitting of fringes increases and decreases periodically corresponding to the half-pitch length *p* but oppositely on the even and odd fringes as shown in the zoom-in the inserted panels and the related fringes in Fig. 4.3b, where the

transition is quite sharp and sometimes discontinuous, indicating sudden slip-in of a new layer.

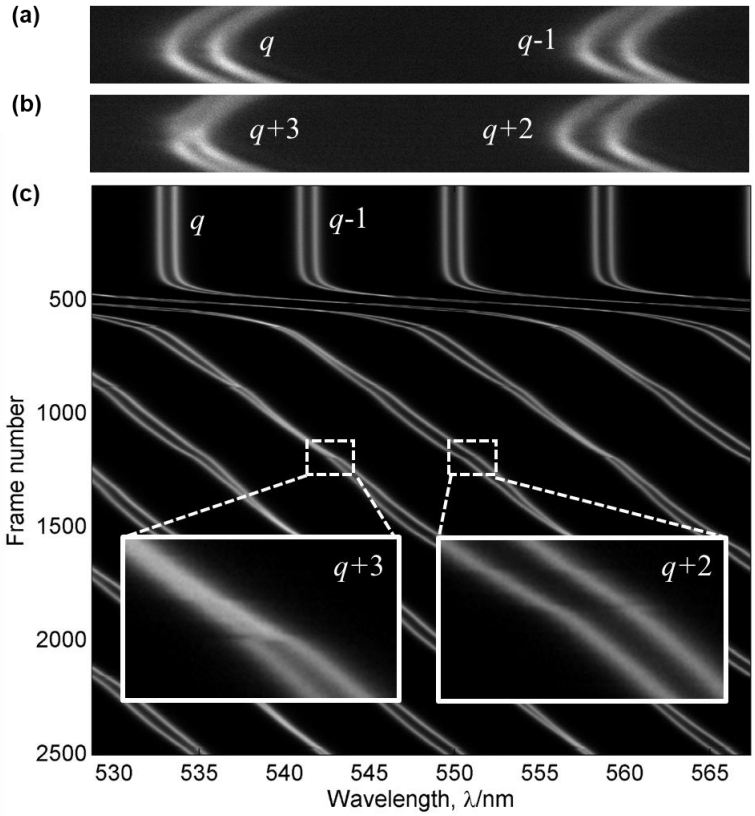

Figure 4.3 Behaviours of the fringes and the corresponding spectrogram with the cholesterics. (a) Snapshot of the fringe q and q-1 near the contact position. (b) Snapshot of twist transitions of fringe q+3 and q+2. (c) Spectrogram of fringes as a function of frame number and wavelengths during the retraction of the surface. The spectrogram with 4 fringes at the contact is processed by the method in Fig. 3.1. The inserted panels are the zoom-in of the fringes q+3 and q+2 during twist transitions that are shown in (b).

The behaviours of fringes are still consistent with the simulation in Fig. 3.21, which can be analysed using isotropic equivalence. The refractive indices of BL036 are known, μ_o = 1.5270, μ_e = 1.794, but the mixture of these nematics and chiral dopant R-2011 might change the refractive index. In order to improve analysis in the later simulation that

requires considerable accuracy, the average refractive index is estimated from one experiment with equation C.1 and C.2, shown in Fig. 4.4a where the average refractive index is a function of the surface separations *D*. The refractive index significantly fluctuates with the distance between 1.57 and 1.64, which is not surprising since those two equations only stand at the distances smaller than 30 nm[152], and at the distances close to contact, it disperses due to systematic errors[196]. Fortunately, the refractive index between 10 and 50 nm is quite constant around 1.595 that is used for further application. As a consequence, the distance profile for Fig. 4.3c is calculated in Fig. 4.4b where the distance is a function of the frame number. Indeed, this profile confirms the descriptions in Fig. 4.3c that the surface jumps out then moves constantly with some fluctuations by the reason of twist transitions.

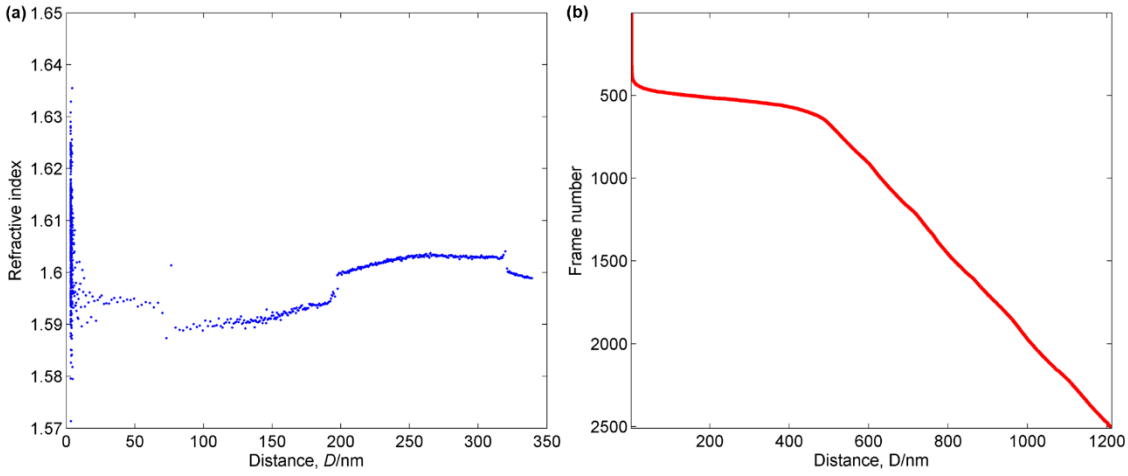

Figure 4.4 Refractive index estimation and distance calculation. (a) The average refractive index μ as a function of the distances *D* calculated by the simplified equations 3.1 and 3.2 from one experiment. (b) Distance profile for Fig. 4.3c as a function of the frame number calculated by the method described in Fig. 3.3 with the average refractive index μ = 1.595 adopted from (a).

The equivalent isotropic simulation is performed to check the accuracy of the refractive index shown in Fig. 4.5a. This simulation captures the movement of the surface and

matches the overlaid average wavelength from the detected experimental region. As is mentioned in section 3.3.4, the overlay between the isotropic simulation and the average detected wavelength might not exactly reflect the accuracy of the refractive index. Therefore, the overlaid spectrogram of the simulation and the experiment is shown in Fig. 4.5b where the isotropic red fringes sit in the centre of the green doublet from Fig. 4.3c for most frames. Visible but still acceptable deviations at large distances with frame number over 2000 are due to the accumulation of errors with the fixed refractive index that should be wavelength-dependent in reality.

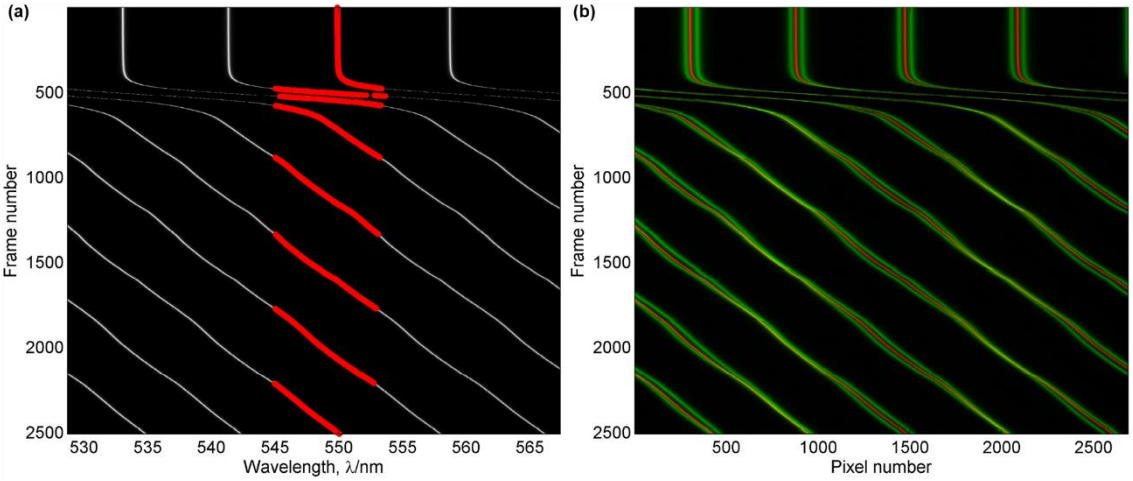

Figure 4.5 Equivalent isotropic simulation. (a) The spectrogram of fringes by isotropic equivalence as a function of the frame number and the wavelengths λ based on the distance profile from Fig. 4.4. The overlaid red lines are the detected average wavelengths from the experimental region for the distance profile. (b) The overlay of isotropic simulation and the experimental spectrogram as a function of the frame number and the pixel number. The red colour is the isotropic simulation from (a), the green colour is experimental spectrogram in Fig. 4.3c, the overlaid region appears yellow.

Given that the refractive index is calibrated above, the twist transitions are analysed subsequently. In Fig. 4.6a, the critical thickness D_c of the transitions from two

experimental setups is plotted as a function of the number of the half-turns n_0. The critical thickness is expected at $D_c = [\alpha/\pi + n_0 + 1/2]\ p$, considering that the transitions would occur at a quarter of pitch distance, namely the middle position of adjacent integer layers, independent from the anchoring strength or the material properties[140], such that the intersection angle α is roughly obtained for two different experiments, 62 ° and 15 ° respectively from the intercept of the *y* axis. The half-pitch p = 122 nm is obtained from the slope, which is consistent with the bandgap measurement by the spectrophotometer (Avaspec 2048-2 by Avantes). If the defects are also taken into account, the transition points might not be exactly in the middle position, which is derived for the planar confinement without the defects[140]. More details about the transition points under the crossed-cylinder confinement will be discussed in the next section 4.3.

With the intersection angle Ψ analyzed through the contact fringes, four possible configurations are drawn in Fig. 4.6b, where the experiment with fixed Ψ = 57.4 ° is used as an example. Unlike the nematic case without the chirality in Fig. 3.10, the cholesterics is chiral nematics with certain rotation direction called handedness resulting in two more configurations. With the intersection angle α = 62 ° obtained in Fig. 4.6a, only the right upper configuration matches the right-handed cholesterics, leading to more accurate intersection angle α = 62.6 ° calculated by Ψ. Likewise, the intersection angle in another experiment is calculated with α = 15.1 °.

4.3 Free energy and force calculation

4.3.1 Free energy of cholesterics confined between two planes

For simplification, the free energy of cholesterics confined between two identical parallel planes, where twist but not splay or bend distortion exists and there are no defects, is

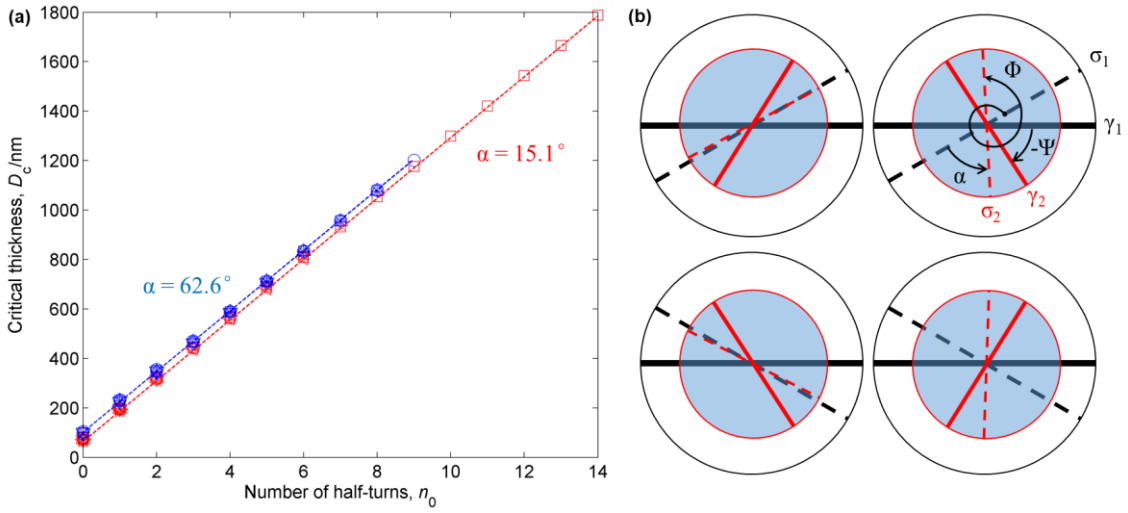

Figure 4.6 Determination of the easy axes for the surface anchoring on the mica. (a) Critical thickness D_c of the twist transitions as a function of the number of the half-turns n_0. The first non-integer layer is counted as 0. The blue and red symbols are from two different experiments with the intersection angle α = 62.6 ° and α = 15.1 ° of the easy axes respectively. Each measurement is represented with a different symbol. The dashed lines are guided lines for critical thickness. (b) Four possibilities of the mica setups with the same intersection angle Ψ = 57.4 ° of the mica and easy axes σ_1 and σ_2 at the ±30 ° from the index axes γ_1 andγ_2 bottom and top surfaces considering the right-handed cholesterics. The white disk with black lines and the blue disk with red lines correspond to the bottom and top mica respectively. The solid lines are the index axes while the dashed lines are easy axes. A counter-clockwise rotation corresponds to a right-handed cholesteric LC. The total twist angle Φ is an example of $\Phi_0(n_0)$ with n_0 = 1 showing the twist angle of cholesterics from the σ_1 to σ_2 easy axis.

analysed. The configuration of the easy axes σ_1 and σ_2 with the deviation δ_1 and δ_2 due to a weak anchoring is shown in the inserted diagram Fig. 4.7a. Typically, the mismatch of the easy axes causes non-integer layer of cholesterics with the intersection angle α, and the deviation δ decreases total the twist angle from intrinsic $\Phi_0(n_0)$ to Φ. Note that twist angles have a sign determined with the usual right-hand rule with respect to a *z* axis that is normal to the surfaces and points upwards from the bottom surface (with director $\mathbf{n}_1$ in

the inset of Fig. 4.7a) to the top surface ($\mathbf{n}_2$). When one of the surfaces is approached or retracted, the free energy per unit area G is formed by the twist elastic energy and the anchoring energy,

$$G = \int_0^h \frac{1}{2} K_{22} (\phi' - q_0)^2 dh + W \sin^2 \delta \tag{4.1}$$

$$\delta = \frac{1}{2}[\Phi_0(n) - \Phi] \in (-\frac{\pi}{2}, \frac{\pi}{2}) \tag{4.2}$$

where h is the surface separation, K_{22} is the twist elastic constant of the cholesterics, φ' = Φ/h is the molecule rotation rate at certain distance h, which is constant for a given distance. The intrinsic molecule rotation rate $q_0 = \pi/p$, W is anchoring strength. Here the Rapini-Papoular anchoring potential $\frac{1}{2} W \sin^2 \delta$ is used, which is valid only at the small deviation δ. Thus twist free energy density in equation 4.1 is integrated, becoming,

$$G = \frac{1}{2} K_{22} (\frac{\Phi}{h} - \frac{\pi}{p})^2 h + W \sin^2 \delta \tag{4.3}$$

When the anchoring energy on the surface is infinite, the deviation δ = 0, meaning that the surface can hold the intrinsic twist angle $\Phi_0(n_0)$, while the opposite limit with zero anchoring energy, molecules can freely rotate on the surface. In between, the molecules deviate from the easy axis to minimize the free energy, namely the twist angle Φ decreases during the compression of layers, but increases during the retraction. During the twist transition from n_0 layers to n_0+1 layers, G_{n0} (h_c) = G_{n0+1}(h_c) would be satisfied when the critical thickness is h_c/p = (n_0+1/2) with an infinite strong anchoring. It has also been proved that this critical thickness is always in the center of two layers, independent of anchoring potential used in the free energy model with finite anchoring[140].

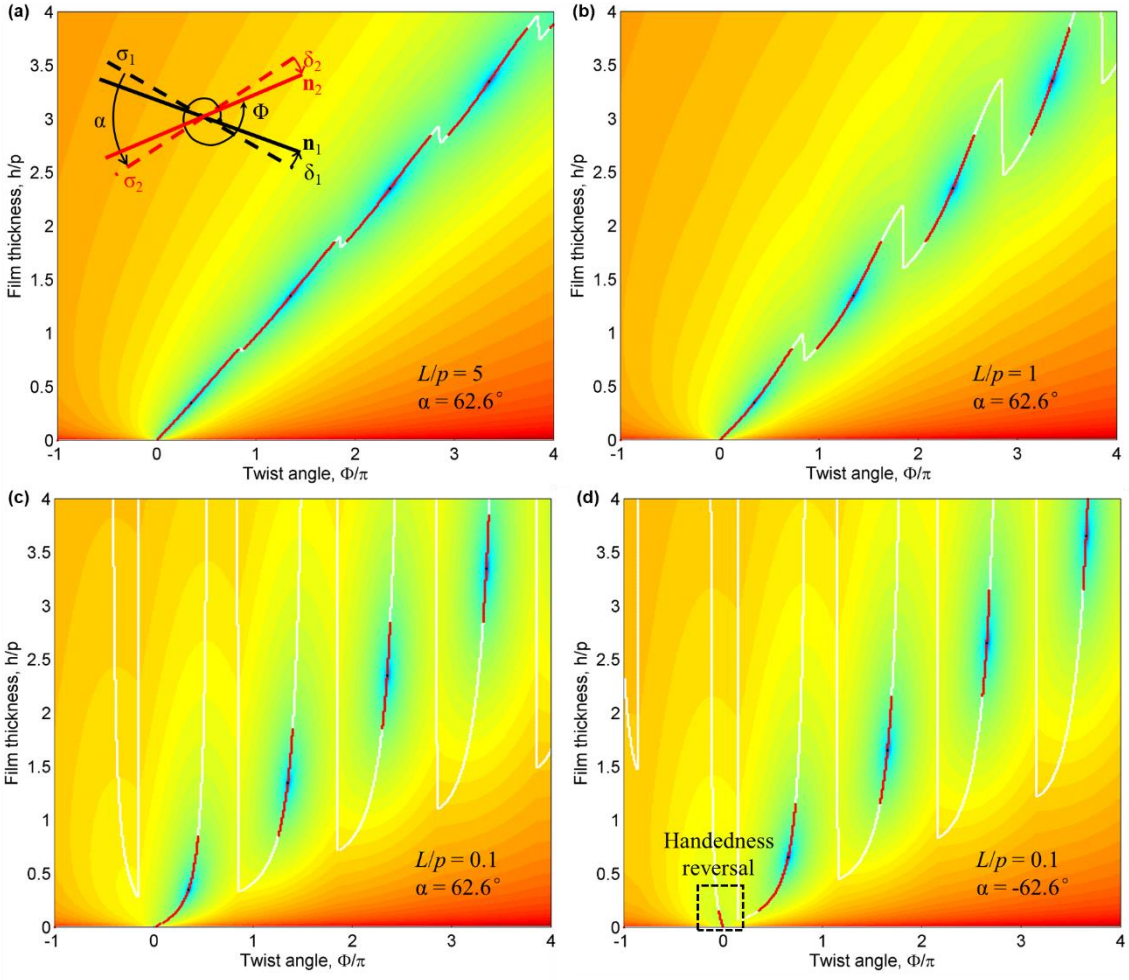

Figure 4.7 Colour-map of the logarithm of the free energy per unit area confined between two planes as a function of the film thickness h/p and the twist angle Φ, with different extrapolation lengths L/p and fixed intersection angle α, p is the half-pitch length. (a) L/p = 5, α = 62.6 °, the inserted diagram shows the configuration of the easy axes σ_1 and σ_2 (dashed lines), deviation angle δ_1 and δ_2, and director $\mathbf{n}_1$ and $\mathbf{n}_2$ (solid lines); the black and white colours correspond to the bottom and top surfaces respectively. (b) L/p = 1, α = 62.6 °. (c) L/p = 0.1, α = 62.6 °. (d) L/p = 0.1, α = -62.6 °. The dashed box highlights the region of the handedness reversal. For the free energy, white and red lines are energy extrema and minima respectively, while the black dots are energy zero.

Fig. 4.7 shows the logarithm of the free energy G as a function of the film thickness h/p and the twist angle Φ with different intersection angles α and extrapolation length L/p. Overall, the twist angle becomes more continuous and smooth during the twist transitions

as the extrapolation length increases, while the twist angle undergoes discontinuous jumps at the same critical thickness with one more layer slipping in. Specifically, in Fig. 4.7a with large extrapolation length L/p = 5, the layers are slightly deformed around energy zero points and the deviation of twist angle Φ is very large since surface anchoring is too weak to hold the molecules. Notably, at smaller film thickness, the twist transition is more continuous. In Fig. 4.7c with small extrapolation length L/p = 0.1, the layers are largely compressed and stretched before and after zero points respectively without much deviation of the twist angle Φ. Interestingly, when the intersection angle α= -62.6 ° is negative, the handedness of the first non-integer layer that is obtuse angle is frustrated and reversed becoming left-handed, shown in Fig. 4.7d, which has also been observed in the highly compressed cholesteric elastomer[203].

The free energy minimum G as a function of the film thickness is further compared in Fig. 4.8 for various extrapolation lengths L. The energy minimum decreases as L increases at a given thickness. In other words, at the smaller anchoring condition, the molecules rotate more freely to change the twist angle that minimizes the free energy. When the anchoring strength is infinite, the free energy G is maximum almost similar to the case L/p=0.01, namely L = 1.22 nm, which holds the twist angle Φ unchanged before twist transitions.

4.3.2 Effect of dislocation defects confined between crossed cylinders

In the SFA, the dislocation defects inevitably form between the crossed cylinders, therefore, the total free energy is the sum of the twist elastic energy and the defect energy, which might affect the critical thickness D_c of the twist transition. For the twist elastic energy, the Derjaguin approximation[18] is assumed, since the typical working distance in

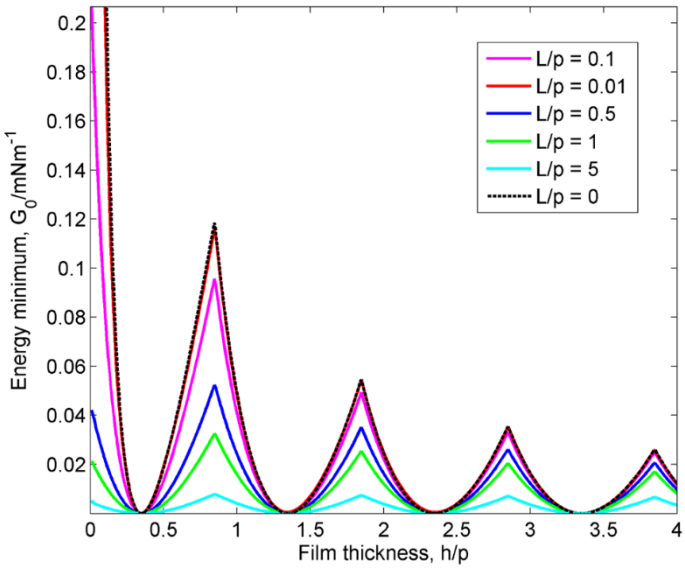

Figure 4.8 Energy minimum G per unit area as a function of the film thickness h/p with fixed α = 62.6 °, different extrapolation lengths L/p ranging from 0 to 5, p is the length of half-pitch. Different colours show different values of the extrapolation length L/p, the black dashed line is for L/p = 0.

the SFA experiments is less than 1 μm that is much smaller than radius R = 1-2 cm of the cylinder and it has been shown that Derjaguin approximation also works in the long-range elastic systems[178, 182]. Regarding the defect energy, it is the sum of line tension energy for all circles of defects. Total free energy E considering infinite strong anchoring from surface separation D_1 to D_2 can be written by calculating the work,

$$E = \int_{D_1}^{D_2} 2\pi R \times \frac{1}{2} K_2 \left(\frac{\Phi}{D} - \frac{\pi}{p}\right)^2 D \, dD + \sum_{i=1}^{n} 2\pi r_d(i) T_d \qquad (4.4)$$

where $r_d(i)$ is the radius of the i^{th} defect, T_d is line tension of dislocation. The elastic energy can also be equivalently calculated from the product of energy per unit area by the area, which is calculated step by step of different loops, as shown in the published paper[204].

When the surfaces separate from the distance D_n of relaxed n layers to the twist transition of n+1 layer, the defects shrink and the smallest dislocation finally annihilates at a critical distance D_c when the new layer slips in, meaning that the twist transition will occur before, i.e. at a smaller distance than the middle position between D_n and D_{n+1}. The free energy change at the distance D_c between D_n and D_{n+1} is $\Delta E = E_{n+1} - E_n$, where E_n is the free energy of n layers moving from D_n to D_c and the total defect energy change from D_n to D_{n+1} is $2\pi r_d(1)T_d$ considering that $(n+1)^{th}$ defect replaces the n^{th} defect. In other words, the effective change of defect energy is due to the defect with the smallest radius. As a consequence, the free energy change ΔE at distance D_c between D_n to D_{n+1} is,

$$\Delta E \approx \int_{D_c}^{D_{n+1}} \pi R^2 K_2 \left(\frac{\Phi}{D} - \frac{\pi}{p}\right)^2 D\, d\, D - \int_{D_n}^{D_c} \pi R^2 K_2 \left(\frac{\Phi}{D} - \frac{\pi}{p}\right)^2 D\, d\, D - 2\pi r_{d,n}(D_c) T_d \qquad (4.5)$$

where $r_{d,n}(D_c)$ is the radius of the smallest defect with n layers at the distance D_c, assuming that the height of the smallest defect position is constant.

At infinite strong anchoring, $\Phi = \Phi_0 = q_0 D_0$ unchanged during deformation, where Φ_0 is relaxed twist angle at D_0, therefore the elastic free energy at distance D in equation 4.3 can be written as,

$$G = \frac{1}{2} K_2 q_0^2 \frac{(D_0 - D)^2}{D} \qquad (4.6)$$

Thus the free energy change ΔE in equation 4.5 is,

$$\Delta E \approx \int_{D_c}^{D_{n+1}} \pi R^2 K_2 q_0^2 \frac{(D_{n+1} - D)^2}{D} - \int_{D_n}^{D_c} \pi R^2 K_2 q_0^2 \frac{(D_n - D)^2}{D} - r_{d,n}(D_c) T_d \qquad (4.7)$$

This free energy change taking into account the defect energy during the transition from 3 layers to 4 layers is compared with the energy change without the defect energy plotted

in Fig. 4.9, where the energy change decreases monotonically with increasing distance but the difference with or without defect energy is barely seen from Fig. 4.9a. If a region of zero energy change is zoomed in, the twist transition can be seen smaller than middle position 3.5*p*. Without the defect energy, the transition also happens at the distance smaller than the middle position due to the crossed-cylindrical geometry. At the distance larger than 3.5*p*, the radius of defect is zero, so there is no difference of energy change.

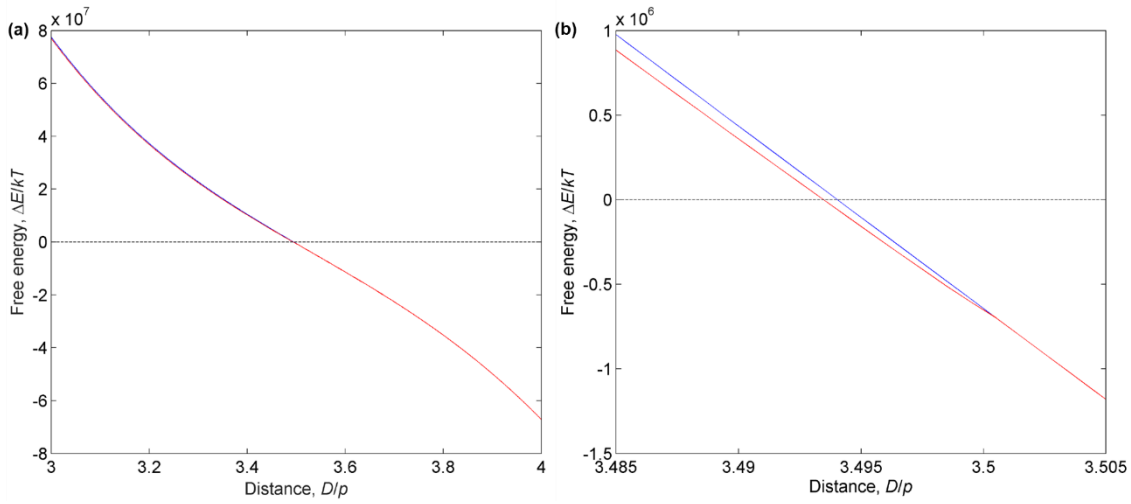

Figure 4.9 Free energy change ΔE normalized by the thermal energy kT at temperature 298 K for the transition from 3 layers to 4 layers as a function of the surface separation D/p with the intersection angle $\alpha = 0$, p is the length of half-pitch. (a) The free energy change without and with the defect energy is shown in the blue and red lines respectively. (b) The zoom-in view of (a). The centre line is $\Delta E = 0$.

4.3.3 Force calculation

The force at the distance D moving from the relaxed distance D_0, experienced by the surface can be obtained by differentiating the free energy in equation 4.4 with respect to the surface separation distance D, shown in equation 4.8,

$$\frac{F}{2\pi R} = \frac{1}{2} K_{22} q_0^2 \frac{(D_0 - D)^2}{D} + \sum_{i=1}^{n} \frac{1}{r_d(i)} T_d \quad (4.8)$$

where the first term is the twist elastic energy per unit area at equation 4.6, while the second term is the defect energy per unit area generated by the defect[204, 205]. At the relaxed integer layers D_0, $r_d(1) = \sqrt{pR} = \sqrt{1.2 \times 2 \times 1.2} \approx 3.5 \mu m$, the corresponding force generated by the first defect that produces largest force $F/(2\pi R)$ is 2.8E-4 mN/m, considering that the line tension T_d is in the same order[41] of the typical twist elastic constant K_{22} = 10 pN. As a result, compared with the oscillating elastic energy in Fig. 4.8, those defects generate negligible non-oscillating background forces.

4.4 Effect of surface anchoring on simulation

The equivalent isotropic simulation in Fig. 4.5 has shown that the refractive index is accurate. By adopting the intersection angle α = 62.6 °, Ψ = 57.4 ° from analysis in Fig. 4.6, the twist angle Φ from Fig. 4.7, the full-parameter simulation is performed to test the extrapolation length, namely the anchoring energy. Three extrapolation length values 0.1, 1 and 5 are used to compare spectrogram results that are overlaid with experimental spectrogram in Fig. 4.10 where the fringes are a function of frame number and wavelengths λ. Overall, the overlay of spectrograms with different extrapolation lengths is quite good without large deviation except during the twist transitions. The regions of twist transitions are zoomed in to show clear deviation in spectrograms with large extrapolation lengths. Only when L/p = 0.1 can one get the best overlay with the experimental figure, indicating that full-parameter simulation is able to well reconstruct the molecule distribution and rotation during the twist transitions, and that the anchoring strength is very large so that the surface can hold the twist angle unchanged before a new layer slipping in. With L/p = 0.1, one can calculate that the extrapolation length L is

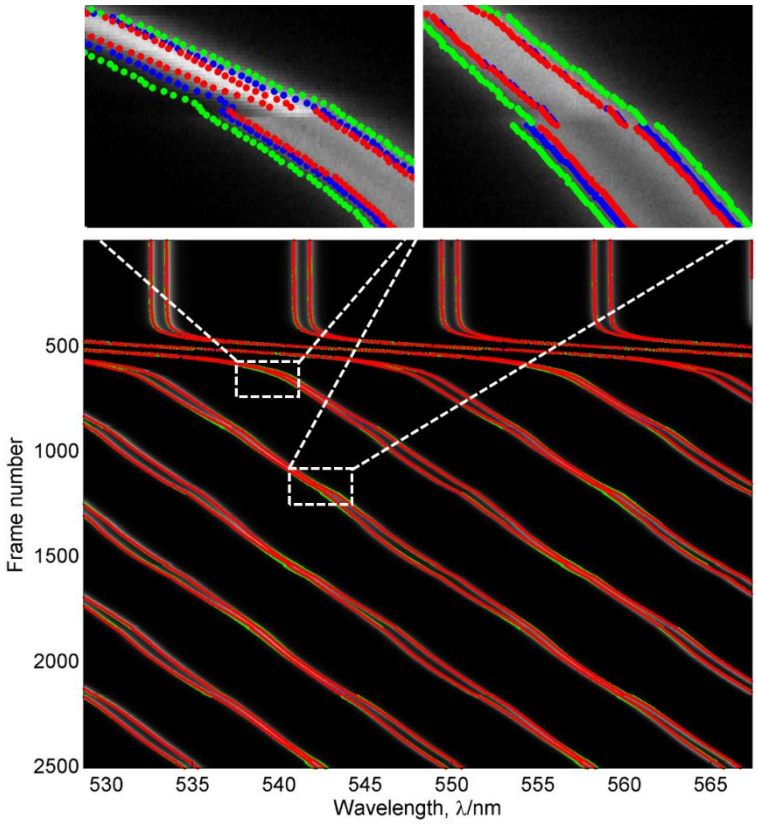

Figure 4.10 Overlaid spectrogram of the cholesteric fringes by the full-parameter simulation and experiment as a function of the frame number and the wavelengths λ. The twist angle Φ as a function of the distance is determined from the calculation shown in Fig. 4.7 with different extrapolation lengths L/p = 0.1, 1 and 5, which correspond to red, blue and green dots, respectively, in the overlaid spectrogram. The white colour of fringes is from the experiment. The inserted panels are zoom-in of twist transitions.

smaller than 12.2 nm, namely anchoring strength $W = K_{22}/L$ = 0.8 mJ/m^2 considering typical twist constant K_{22} = 10 pN. Such anchoring strength is in the upper limit of the typical azimuthal anchoring[72] range from 10^{-7} to 10^{-3} J/m^2. However, there is also a limitation that whether the anchoring deviation is following the Rapini-Papoular anchoring potential cannot be examined in this experiment since anchoring is so strong.

4.5 Equilibrium forces in cholesterics

The forces experienced by the surface during the twist transitions can be measured at the free end of the cantilever when the fixed end was moved by the motor at a constant speed. Firstly, the speed deviation of the surface motion to the motor speed as a function of the distance D is plotted in Fig. 4.11a. The deviation is smaller than 2 nm/s and fluctuates with period pitch p after the initial strong jump-out of the surface from adhesive contact due to van der Waals attraction. This indicates that the twist transitions indeed cause periodic stretch and compression of layers, and that the forces are measurable. The corresponding forces F normalized by the cylinder radius R as a function of the distance D are plotted in Fig. 4.11b,c with different zooming, where the maximum forces around 0.2 mN/m that are one order higher than the resolution of the SFA are obtained during the twist transition points.

It is worth noting that these structural forces can be fitted with equation 4.3 with K_{22} = 17 pN and L/p = 0.1, which produces a large anchoring strength W = 1.4 mJ/m^2, meaning that basically anchoring is consistently strong and the anchoring potential plays a small role in this experiment, but the value of anchoring strength could be artificial due to systematic errors like the spring constant or the radius of the cylinder. The anomalous high value of the twist constant K_{22} = 17 pN that is used to fit the forces might be due to the fact that data is noisy and the calibration of zero forces may prevent the detection of a linear force background, although with cholesterics the elastic forces may exist everywhere during surface retraction. In this experiment, the calibration relies on the assumption that the force minima are around zero. Last but not the least, the speed during the twist transition is going to the maximum that produces non-negligible viscous forces reported in the SFA community[206].

4.6 Summary

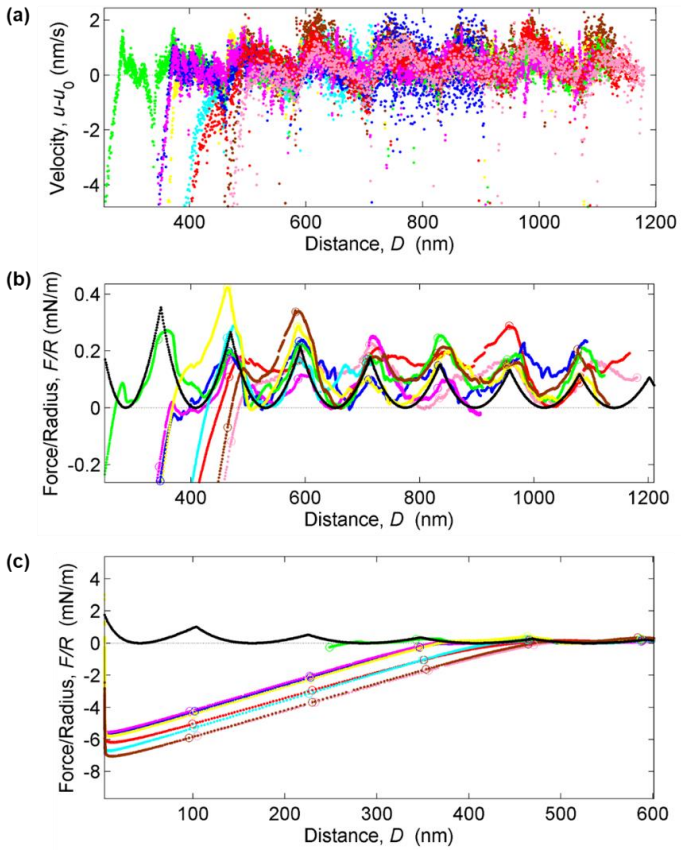

Figure 4.11 Speed and force during surface retraction measured in the SFA. (a) Velocity u-u_0 of the surface movement during the retraction as a function of the distance D, u is the instant speed of surface, which is set as negative, u_0 is the speed of the motor. (b) The zoom-in and (c) zoom-out of surface forces F normalized by the radius R as a function of the distance D, the black curves are forces calculated with K_{22} = 17 pN and L/p = 0.1. The circular points are positions during the twist transitions in each retraction experiment. The forces are calibrated assuming that the force minima sit on the 0. The different colours are used to indicate different retractions in the same setup.

In this chapter, the cholesterics are confined in the SFA during the retraction of the surface, where the twist transitions and the equilibrium forces are characterized and analysed. The simulation tool based on 4x4 matrix is used to reconstruct the optics during the twist transitions and the free energy based on the twist elastic energy and the anchoring energy is applied to explain the structural forces encountered at the quasi-equilibrium movement. Some conclusions are drawn as following,

(1) The cholesterics form layers, which produce splitting changes in fringes during the twist transitions, and the circular dislocation defects that are similar to the defects generated in the Grandjean-Cano wedge.

(2) The periodical twist transitions and the splitting changes are due to slipping-in of a new layer equal to half-pitch p that changes the total twist angle at the middle positions between two consecutive integer layers.

(3) The equivalent isotropic simulation stands using the average refractive index calculated from the odd and even fringes.

(4) The half-pitch length p = 122 nm and the mismatch intersection angle α = 62.6 ° of the easy axes are obtained through the analysis of the critical thickness of the twist transitions as a function of the number of the half-turns n_0.

(5) The free energy from the twist elastic energy and the Rapini-Papoular anchoring potential is calculated to estimate the equilibrium forces. The stronger anchoring energy is, the higher free energy gains during the twist transitions, but at strong anchoring, the Rapini-Papoular anchoring potential is small and cannot be tested. Meanwhile, the dislocation defects make negligible contributions to the free energy and the position of the twist transitions.

(6) The full-parameter simulation well reconstructs the optics during the twist transitions taking into account the instant molecule rotation angle, which estimates a strong anchoring strength W = 0.8 mJ/m^2 that is in the upper limit of reported values.

(7) The equilibrium forces during the twist transitions are oscillating with the period p and are measurable in the SFA. These forces are noisy with the force peak one order

higher than the resolution of the SFA, which are fitted by the free energy model with anomalous K_{22} producing artificial anchoring strength as a result of systematic errors.

5 Anchoring-mediated stick-slip winding of cholesterics

5.1 Introduction

In broad soft mater areas, including turbulence[207], micro/nanofluidics[208] and yield stress materials[209], boundary conditions are of importance for material properties and performances. Similarly, in LCs, surface anchoring also plays a crucial role on the order parameter, the temperature of the nematic-isotropic phase transition[17], as well as the responses of molecules to the external fields[2], especially in confined geometry such as LC displays. During the cholesteric-nematic unwinding by external fields, there is a controversy on the role of the surface anchoring that might induce stick-slip behaviours, despite well-known continuous transitions observed in experiments, which has been discussed in section 1.4.3.

Here we use the SFA to measure the responses of desiccative cholesterics during surface approach under various boundary conditions, whereas in Chapter 4 we presented the results obtained during surface retraction. As we will see, the behaviours are very different in the two cases. In the beginning, a strong anchoring was obtained, but anchoring strength decayed with time mainly due to the adsorption of the water from the ambient environments[76, 174], as such, different regimes were observed during the approach of experiments as a result of the decayed anchoring. The surface torque that is analogous to friction torque in static rotational friction is adopted to explain these regimes and the retardation of twist angles among them. Both anchoring deviation and retardation are

unified with fracture mechanics. It is the fracture energy that hinders the nucleation of a new defect loop, given that the calculation of defect energy is negligible in Chapter 4.

5.2 Three regimes

Fig. 5.1 gives an overview of the normalized force profile F/R as a function of distance D obtained in three regimes. In the first regime shown in red, the force generated by constrained cholesterics initializes from zero then increases with increasing surface compression to 65%, maximizing at 14 mN/m before the surface jumps into contact and all the cholesteric layers (n = 11) are squeezed out from the contact region. In the second regime observed after exposure to air in the SFA, shown in pink line, a stick-slip jump of the surface, resembling the stick-slip motions observed in frictions[18], occurs after the force is accumulated to 1.5 mN/s with more than 30% compression, and finally surface jumps to contact. The number of jumps corresponding to a non-integral and 5 integral (n = 5) cholesteric layers, although some of them jump consecutively. In the last regime, shown in blue, surface jumps periodically with a period equal to the half-pitch without a large deformation of the cholesterics and the last few layers are difficult to squeeze out. Additionally, there is a background force showing in the third regime, such that the force minima are not sitting on zero and some parts of the forces are even larger than the forces in the second regime.

The compression that cholesterics can sustain decreases with time from the first regime to the third regime, indicating the decrease of anchoring strength after the adsorption of water from the ambient environment[76, 174]. In the third regime, surfaces are difficult to be compressed to contact, which supports the assumption that surfaces are changing with time. There are several reasons why a harder wall is encountered before contact. Firstly,

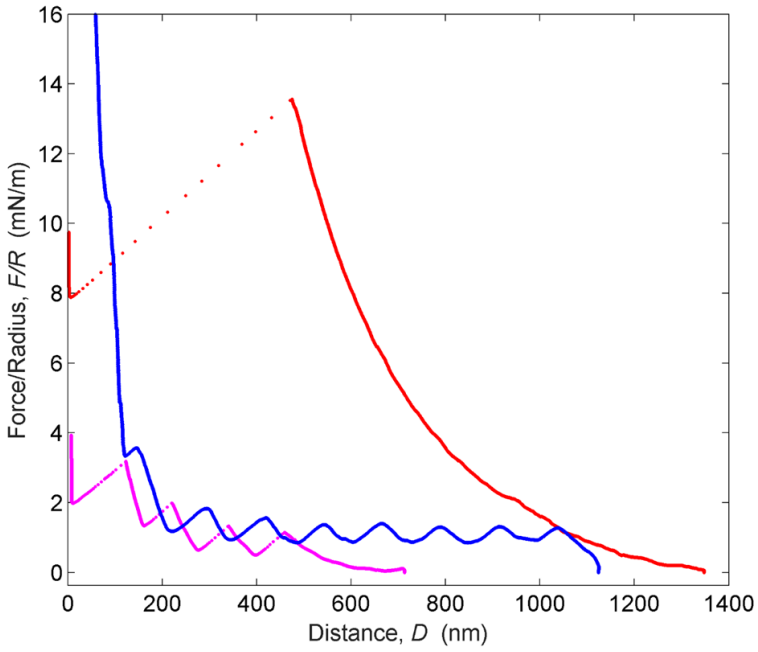

Figure 5.1 Normalized force F/R as a function of distance D in three regimes. Red, pink and blue force profiles are in the first, second and third regimes approaching from certain distances, respectively, with decreasing anchoring strength. All the forces are calibrated with only one fit parameter, the speed of the motor, to match the twist elastic deformation.

the adsorbed water dissolves and accumulates potassium ions from the mica surfaces to contact position leading to electrostatic repulsion between the surfaces. Secondly, LC molecules grow epitaxially with time[69]. Thirdly, contaminators from ambient air adsorb to the surface.

5.2.1 Constrained regime

Fig. 5.2 shows the theoretical fit by equation 4.6 with K_{22} = 3.8 pN for force profile in the first regime. The match between experiment and theory is quite good indicating that anchoring strength in the first regime is strong. The slope of jump-in is similar to the spring constant $dF/dD \approx k$, which manifests the spring instability, mechanical instability

of the SFA setup occurring in regions of the force curve where $dF/dD > k$, dominants the jumping process.

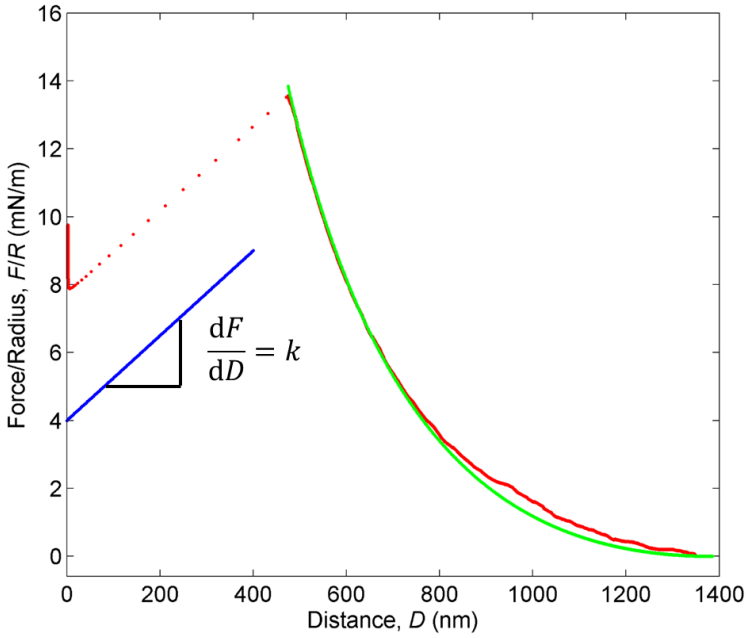

Figure 5.2 Force profiles in the first regime approaching with motor speed 1.7 nm/s, the green line is theoretical fit by equation 4.6 with K_{22} = 3.8 pN. The slope of the blue line is spring constant $\frac{dF}{dD} = k = 1.2$ mN/m.

Fig. 5.3 shows force responses as a function of time in the first regime with 50% compression but before reaching the critical distance. At $t = 20$ min, the motor stops and re-approaches at $t = 90$ min, between which surface distance is sustained by the cholesterics with a deviation less than 40 nm mainly due to mechanical and thermal drifts, as shown in Fig. 5.3b. After re-approach, cholesterics are further compressed before all layers jumping into contact. The long-time study demonstrates that the surfaces experience elastic forces rather than dissipative viscous forces.

5.2.2 Stick-slip regime

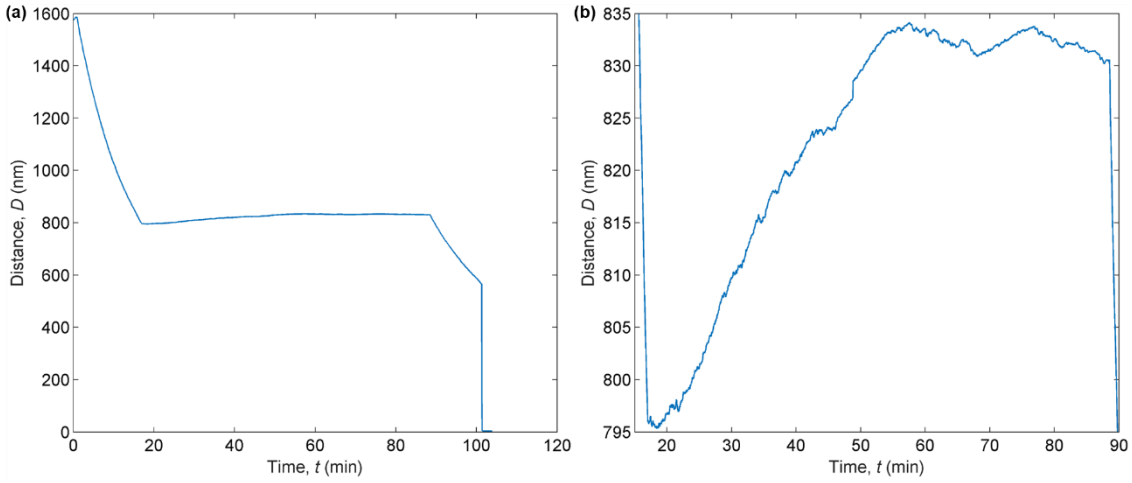

Figure 5.3 (a) Distance profile *D* as a function of time *t*. (b) Zoom-in of distance profile.

Fig. 5.4a shows the crossing points of force profiles calculated by equation 4.6 with various layers of cholesterics, which fall on the distance equal to the integral number of the quarter pitch. Notably, the calculated slope of force profiles is similar to the spring constant, indicating that the jumping process is a balance of the visco-elastic forces and the spring force rather than a pure spring instability, which is shown in Fig. 5.4b, where jumping distances are smaller than the theoretical values. This can be due to the effect of dislocation defects, which has been discussed in section 4.3.2. The force profile in the second regime is well fit by theoretical calculation if the number of layers at the contact position is manually reduced during a jump, shown in Fig. 5.4c, indicating that anchoring strength is still strong in this regime.

Fig. 5.5 shows more force profiles in the first and second regimes. These force profiles see similar slopes of jump-in to the spring constant. Interestingly, multiple-layer events of jump-in are also observed in the second regime, indicating that the second regime possesses features from both first and third regimes. During experiments, the SFA experienced the first regime then the second regime, but reentry of the first regime also

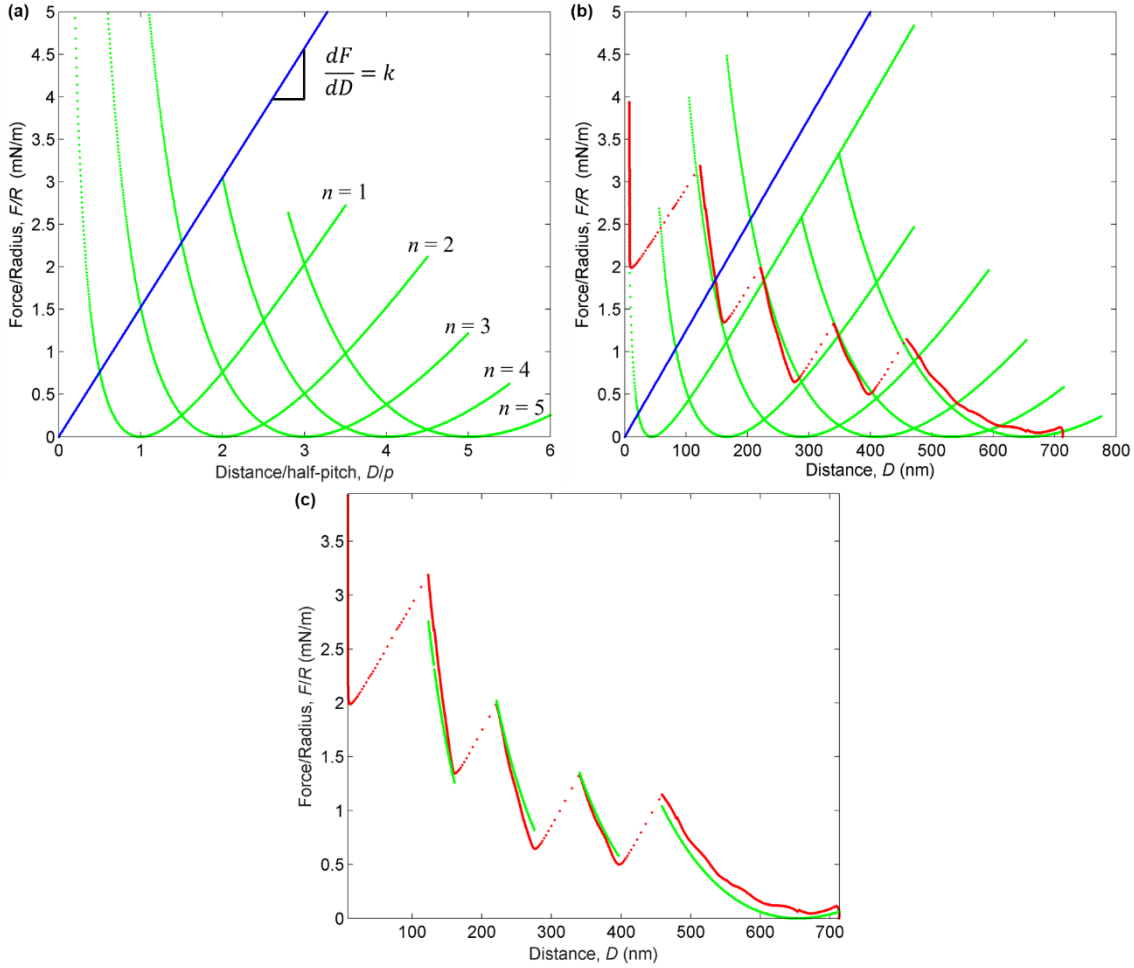

Figure 5.4 Force profiles in the second regime. (a) The normalized force F/R as a function of normalized distance D/p by equation 4.6 with n layers of cholesterics, p is half-pitch, and slope of the blue line is spring constant k. (b) Overlay of force profile (red line) of the second regime with calculated force profiles (green lines) by equation 4.6 with various layers of cholesterics, the slope of the blue line is spring constant, and the red line is calculated with K_{22} = 6 pN (c) Force profile (red line) of the second regime fit by equation 4.6.

occurred. This implies for future the possibilities of controlling the regime and therefore compression responses by controlling water content.

5.2.3 Sliding-slip regime

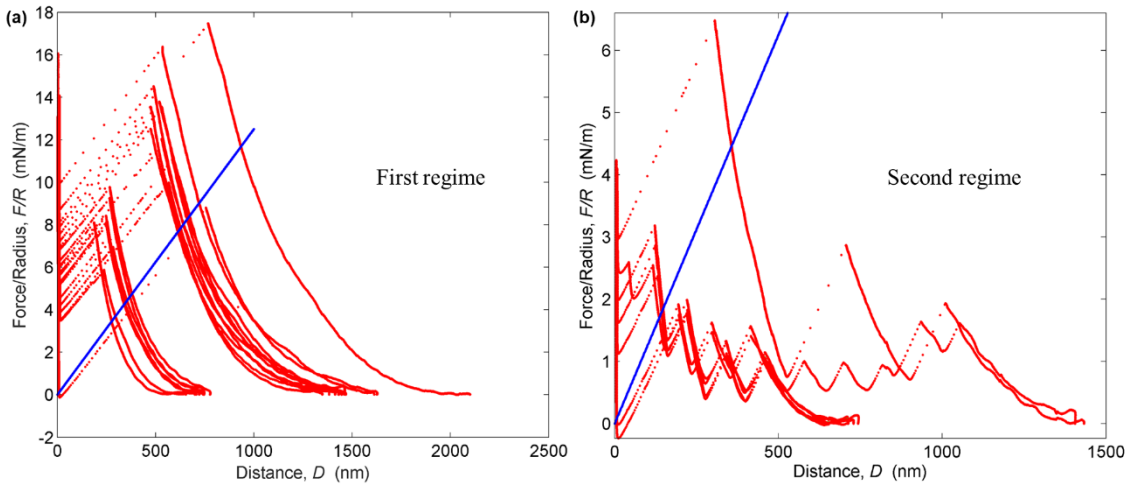

Figure 5.5 Force profiles in (a) first regime and (b) second regime, the slope of the blue line is spring constant.

Likewise, the third regime could be analysed with the method for the first two regimes. Although in this regime the anchoring is expected to be small and the elastic force will be small because of deviation anchoring direction from the easy axis, the defects move and interact with the surface at such small anchoring[24], which may cause strong pinning with surface and stabilize the layers. Besides, molecules may slide at the surfaces with increasing the surface viscosity. Therefore, the fitting of the force profile in this regime will be complicated.

These three regimes emerge with time and, most likely, decrease of anchoring strength. Considering the longer time scale, more regimes might appear. For example, if the adsorbed water changes the direction of the easy axis of mica surface[76, 174], the behaviours can be different. Finally, if the mica surfaces become totally homeotropic, the pitch axis will be parallel with surface causing fingerprint textures and more isotropic-like optics.

5.2.4 Burgers vector

According to a study of cholesterics in a wedge-shaped cell[210], Burgers vector b, characterizing the layer mismatch around a dislocation line, increases from half-pitch $b = p$ to pitch $b = 2p$ at a critical distance $h_{b\,c}$ with a given wedge angle ranging $5\ \mathrm{mrad} < \alpha_w < 20\ \mathrm{mrad}$, meaning that the number of cholesteric layer changes by one (thickness change of $2p$) around a dislocation at large film thickness. The critical distance $h_{b\,c}$ is estimated,

$$h_{b\,c} = \frac{0.08 \times 2p}{\alpha_w} \tag{5.1}$$

considering the SFA geometry in Fig. 2.1c with cylindrical radius $R = 0.01\ \mathrm{m}$, effective wedge angle α_w is obtained,

$$\alpha_w = \sin^{-1}\frac{r}{R} = \sin^{-1}\frac{\sqrt{2Rh_{b\,c}}}{R} \tag{5.2}$$

The critical distance is calculated combining equation 5.1 and 5.2, $h_{b\,c} \approx 1.2379\ \mathrm{nm}$, with which wedge angle $\alpha_w = 1.57\ \mathrm{mrad}$, within the valid range of equation 5.1. This critical distance is around 10-11 layers that are typical experimental distances. Some experimental data may need to be calibrated the change of Burgers vector, however, no evidence has been found in the data. Probably, this is due to the deviation of the equation 5.1 in different geometries or more careful examination of data is necessary, which might decrease the errors in the fitting of force profiles, but the effect of Burgers vector on calculation will be small at such large distances.

5.2.5 Strain-stiffening

With strong anchoring, the force per unit area Π, namely disjoining pressure, and Young's modulus E_y are calculated from equation 4.6,

$$\Pi = -\frac{d\,G}{d\,D} = \frac{1}{2}K_{2\,2}q_0^{\,2}\left(\frac{D_0^{\,2}}{D^2} - 1\right) \tag{5.3}$$

$$E_y = \frac{\Pi}{(D_0 - D)/D_0} = \frac{1}{2}K_{2\,2}q_0^{\,2}\left(\frac{D_0^{\,2}}{D^2} + \frac{D_0}{D}\right) \tag{5.4}$$

Fig. 5.6 shows that both pressure and Young's modulus are not linear as a function of distance, indicating a strain-stiffening[211] relationship. The Young's modulus $E_y \approx$ 1 0 P aunder 70% compression, which is larger than the Young's modulus of aqueous foam and granular bed[212], showing that a large amount of energy can be stored in the twist configurations[213].

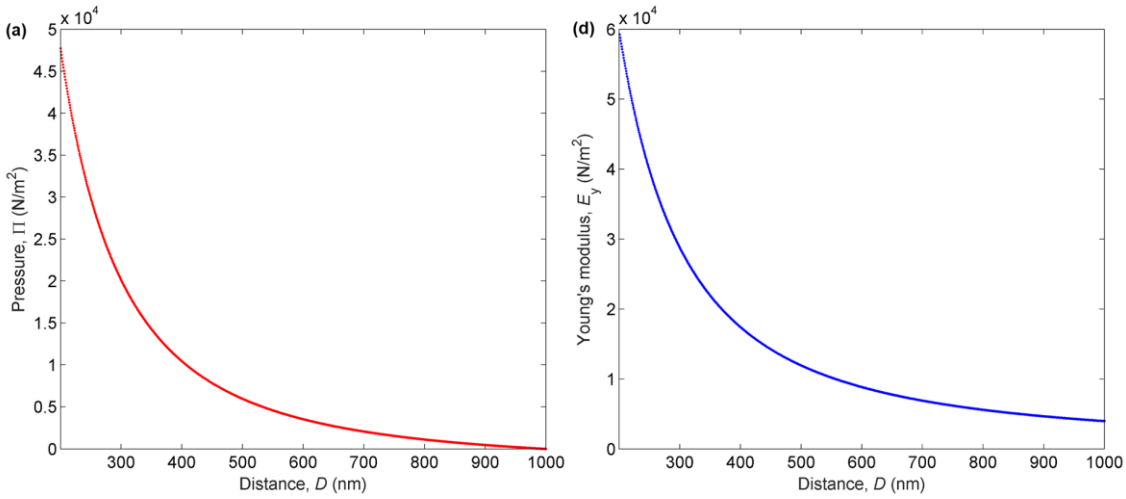

Figure 5.6 Strain-stiffening of cholesterics. (a) Pressure as a function of distance D, calculated by equation 5.3. (b) Young's modulus E_y as a function of distance D, calculated by equation 5.4. $K_{2\,2}$= 6 p Nand $p = 1\ 2$ n2 mare used for calculation.

5.3 Surface torque

The measured forces follow this equation very well with manual input of twist angle, but three different regimes varying with anchoring strength are measured, namely

constrained, stick-slip and sliding-slip. How do we understand the critical threshold of jump in different regimes?

When cholesterics are confined between two plates, the elastic torque is balanced by the surface torque that is generated by surface anchoring and surface viscosity[141-143]. For strong anchoring, molecules deviate very slowly from the easy axis, thus torque from surface viscosity is negligible, while at medium anchoring, molecules slide to deviated angle with larger speed, therefore, both surface anchoring and surface viscosity balance with elastic torque.

$$K_{22}\left(\frac{\partial\Phi}{\partial D}-q_0\right)=W\frac{\Phi_0-\Phi}{2}+\gamma_s\frac{\partial\Phi}{\partial t} \tag{5.5}$$

where W is anchoring strength, Φ_0 is original twist angle, γ_s is the surface viscosity, and t is the time.

5.3.1 Strong anchoring

With strong anchoring, surface viscosity is neglected here. The elastic torque Γ_e is mainly balanced by the anchoring torque Γ_a,

$$\Gamma_e=K_{22}\left(\frac{\Phi}{D}-q_0\right)=\Gamma_a=W\frac{\Phi_0-\Phi}{2} \tag{5.6}$$

$$\Gamma_e\approx K_{22}q_0\left(\frac{D_0}{D}-1\right) \tag{5.7}$$

Fig. 5.7 shows that there exists a threshold constant of critical jumping distance D_c over original distance $\frac{D_c}{D_0}$, about 35% and 75% for first and second regimes respectively, for the surface to sustain the elastic stress at certain anchoring conditions, no matter how many layers are compressed. This means there is a threshold torque Γ_c that is analogous

to breakaway friction torque [214] that is a term in rotational friction. When the anchoring is large, larger friction torque can sustain elastic torque, such that cholesteric layers will not jump until the threshold is reached. Once the layers jump, stick-slip happens.

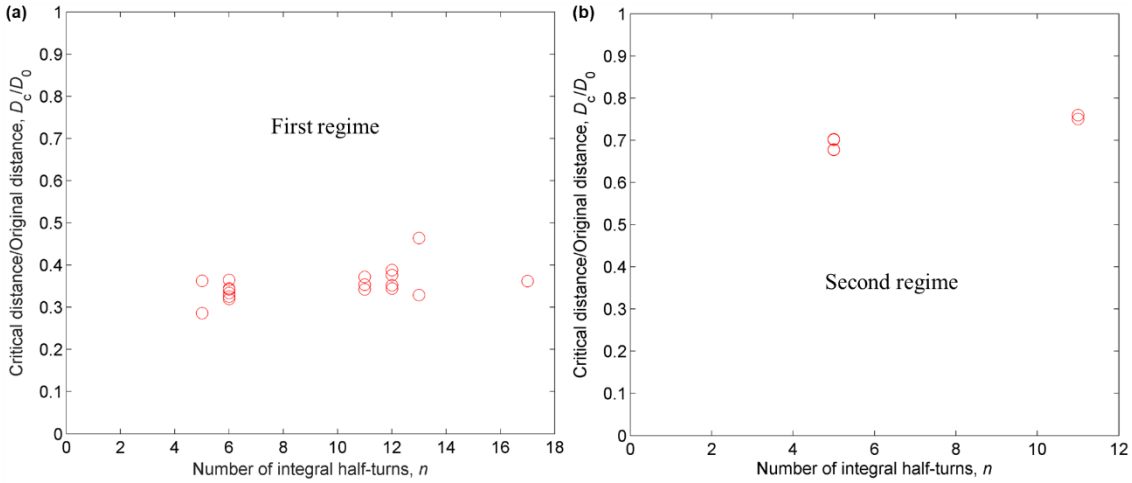

Figure 5.7 Normalized critical jumping distance $\frac{D_c}{D_0}$ as a function of the number of integral half-turns n. (a) First regime. (b) Second regime.

The anchoring torque in first and second regimes is plotted in Fig. 5.8, scattering around 1.9×10^{-4} and 0.7×10^{-4} mN/m respectively. The first regime and second regime fall on different slopes of calculation based on equation 5.7 with K_{22}= 3.8 and 6 pN. If the force profile in Fig. 5.2 is carefully examined, one can see that the slope at small compression is actually higher than calculation with K_{22}= 3.8 pN. This may be because mica surfaces on lenses are not large enough, such that at large compression, forces are responded by the area larger than the mica coverage. Outside the mica coverage, the glue produces negligible forces. While at small compression, the forces mainly generated near the contact position are free from the effect of mica areas. From the fitted elastic constant, we can estimate the effective coverage of mica on lenses is 2/3.

For more rigorous calculation considering anchoring deviations, the surface distance D in equation 5.6 is calculated as,

$$D = \frac{K_{2\ 2}\Phi}{K_{2\ 2}q_0 + W\frac{\Phi_0 - \Phi}{2}} \tag{5.8}$$

At the critical torque threshold Γ_c, the critical twist angle Φ_c and the critical surface distance D_c are calculated,

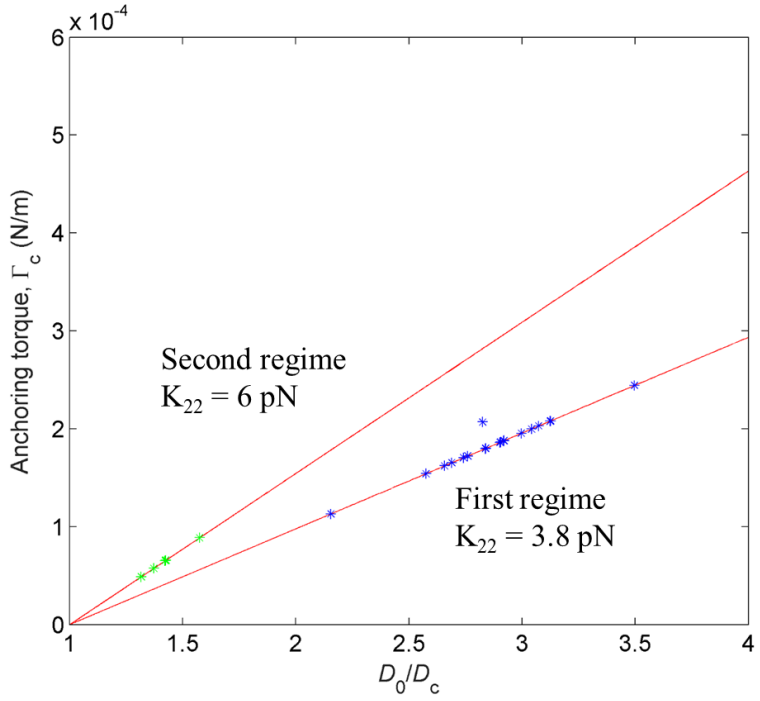

Figure 5.8 Anchoring torque $_c$ as a function of normalized critical jump distance D_0/D_c, the red line is theoretical prediction according to equation 5.7 with $K_{2\ 2}$= 3.8 and 6 pN, blue dots are calculated with critical jump distance from the first regime and green dots are calculated with first critical jump distance from the second regime. All data are using fitted twist constants $K_{2\ 2}$to calculate anchoring torque.

$$\Phi_c = \Phi_0 - \frac{2\Gamma_c}{W} \tag{5.9}$$

$$D_c = \frac{K_{22}(\Phi_0 - \frac{2\Gamma_c}{W})}{K_{22}q_0 + \Gamma_c} = \frac{D_0 - \frac{2\Gamma_c}{q_0 W}}{1 + \frac{\Gamma_c}{K_{22}q_0}} \tag{5.10}$$

From Fig. 5.9, the slope and intersection of critical distance as a function of original distance in the first regime are obtained from the trend line, although the Burgers vector[210] may need to be considered to calibrate the data, minimizing scattering, thus,

$$\frac{1}{1 + \frac{\Gamma_c}{K_{22}q_0}} = 0.3\ 9\ 6\ 8 \tag{5.11}$$

$$\frac{-\frac{2\Gamma_c}{q_0 W}}{1 + \frac{\Gamma_c}{K_{22}q_0}} = -4\ 7\ 7\ 4\ 8\ 1\ 0^{-9} \tag{5.12}$$

$\Gamma_c \approx 0.2\ 3$m N/m, $W \approx 0.1\ 5$m N/m with $K_{22} = 6$ p N and half-pitch $p = 1\ 2\ 2$ m The anchoring energy is similar to the value by dimensional estimation[215] $W \approx K_{22}q_0 \approx 0.1\ 5$m N/m. The deviated angle on one surface can be calculated $\frac{\Phi_0 - \Phi}{2} \approx 0.4\ 9$rad, which means the molecules on each surface deviate 90° from easy axis at the jump threshold. Perhaps this is a maximum intrinsic angle of deviation, which could potentially be observed by polarized microscope to prove the prediction. Notably, with the Rapini-Papoular potential[2], no solution can be found. Certainly, anchoring potential with other forms may also be feasible. For example, if the anchoring torque is $\frac{1}{2}W\frac{\Phi_0 - \Phi}{2}$ differentiated from parabolic potential, the anchoring strength will be 0.3 mN/m, but the critical torque and deviated angle are still the same.

From equation 5.8, twist angle Φ is a function of surface distance D,

$$\Phi = \frac{\Phi_0 + \frac{2K_{22}q_0}{W}}{1 + \frac{2K_{22}}{WD}} \tag{5.13}$$

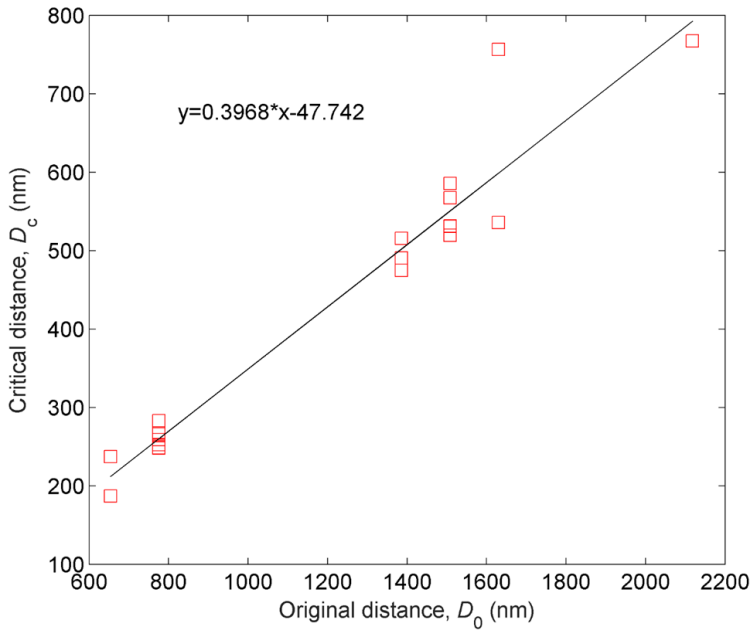

Figure 5.9 The critical jump distance D_c as a function of the original distance D_0 in the first regime, the black line is the linear trend line.

With parabolic anchoring potential, free energy can be calculated,

$$G = \frac{1}{2}K_2\frac{(\Phi - q_0 D)^2}{D} + W\left(\frac{\Phi_0 - \Phi}{2}\right)^2 = \frac{1}{2}K_2\frac{\left(\frac{\Phi_0 + \frac{2K_2 q_0}{W}}{1+\frac{2K_2}{WD}} - q_0 D\right)^2}{D} + W\left(\frac{\Phi_0 - \frac{\Phi_0 + \frac{2K_2 q_0}{W}}{1+\frac{2K_2}{WD}}}{2}\right)^2 \quad (5.14)$$

and the corresponding force profile is compared with the profile in the infinite anchoring case, shown in Fig. 5.10 where the deviation is small, but indeed the additional anchoring energy decreases total forces, and the obtained elastic constant $K_2 = 4.2$ pN is closer to the molecular property.

5.3.2 Medium anchoring

For the second regime, all the stick-slip jumping points except those within spring

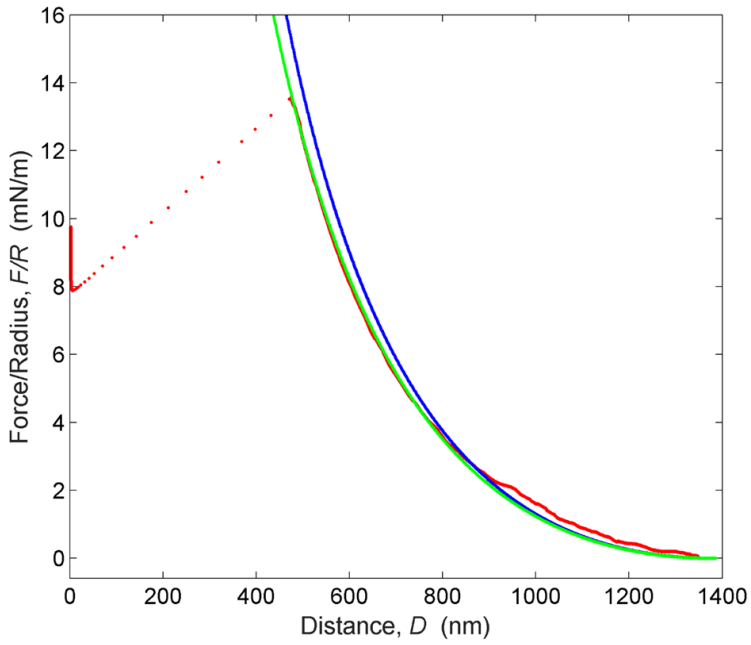

Figure 5.10 Normalized force $\frac{F}{R} = 2\ G$ as a function of distance D in the first regime, the red line is from the first regime in Fig. 5.1, blue and green lines are calculated based on equation 5.3 and 5.13 respectively, with $K_{2\ 2} = 4.2$ p N

instabilities are plotted as a function of original distance, as shown in Fig. 5.11. Similarly, the critical torque $\Gamma_c \approx 0.0\ 1\ 4$ mN/m, anchoring strength $W \approx 0.0\ 0\ 7$ mN/m and $\frac{\Phi_0 - \Phi}{2} \approx 1\ 1.4°$ for the second regime are calculated from the slope and intersection at the large distance in Fig. 5.11.

The anchoring strength in the second regime is not strong compared with the first regime, and the deviation of force profile is large from the infinite anchoring force profile, shown in Fig. 5.12.

The anchoring torque and strength calculated from Fig. 5.11 are used to predict the positions where consecutive jumps occur, shown in Fig. 5.13. The critical jumping distances fit the experimental data very well. However, the odd thing is that force profile is fit by the infinite anchoring case where anchoring energy does not contribute to the

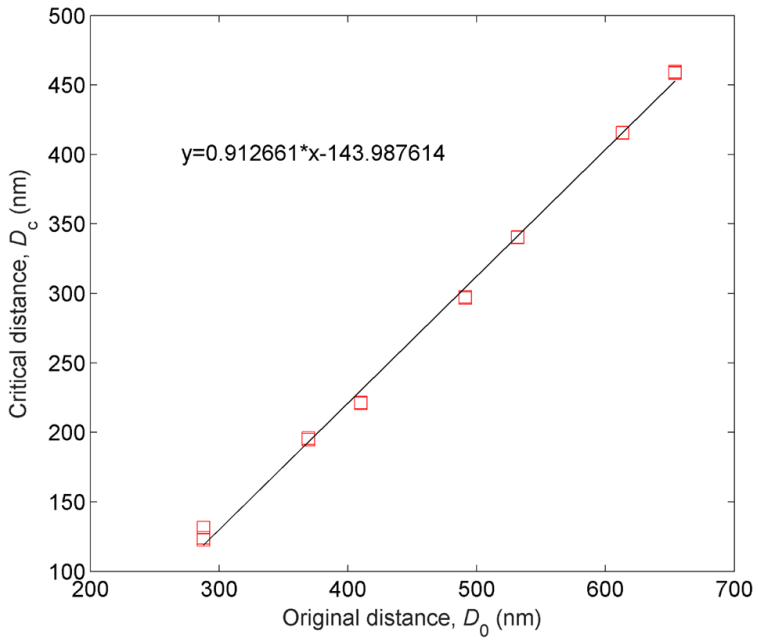

Figure 5.11 The critical jump distance D_c as a function of the original distance D_0 in the second regime. Data fit by the linear trend line, only data with determined layers is used, and the anchoring transition that is discussed in section 5.3.4 has been taken into account.

free energy. It is like that the surface torque is correct but the composition of the torque is not pure anchoring. Possibly, the surface viscosity may start to be important in this regime. Alternatively, the 2/3 coverage of mica on the lenses may cause slip on this regime after water adsorption, since the critical compression rate is similar to the compression rate where $K_{2\ 2}$changes from 6 pN to 3.8 pN in the first regime, shown in Fig. 5.2.

In the second regime, either during approach or retraction, no defects are observed stretching on the surface, indicating that defects are in the bisector of surfaces and the polar anchoring energy[24] is larger than $2\sqrt{\frac{3}{8}K_{3\ 3}B} \approx 0.4$ m N/m, where $K_{3\ 3}$is bend

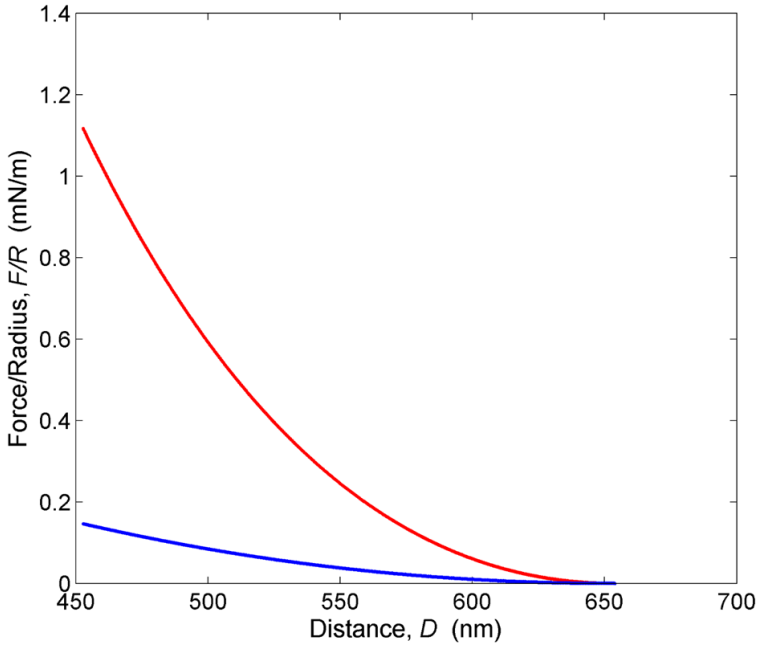

Figure 5.12 Normalized force $\frac{F}{R} = 2\ G$ as a function of distance D in the second regime, red and blue lines are calculated based on equation 4.6 and 5.14 respectively.

constant, $B = K_2\ q_0^2$ is compression modulus of cholesterics. It seems reasonable that the azimuthal anchoring energy is one or two orders smaller than polar anchoring[72]. Then the polar anchoring energy in the first regime would be very large.

5.3.3 Weak anchoring

For very weak anchoring, the anchoring torque is negligible[142], therefore, the elastic torque is mainly balanced by the surface viscosity.

$$K_2\left(\frac{\Phi}{D} - q_0\right) = \gamma_s \frac{\partial \Phi}{\partial t} = \gamma_s \omega \tag{5.15}$$

$$\frac{\partial D}{\partial t} = v \tag{5.16}$$

$$\frac{\partial \Phi}{\partial t} = \omega \tag{5.17}$$

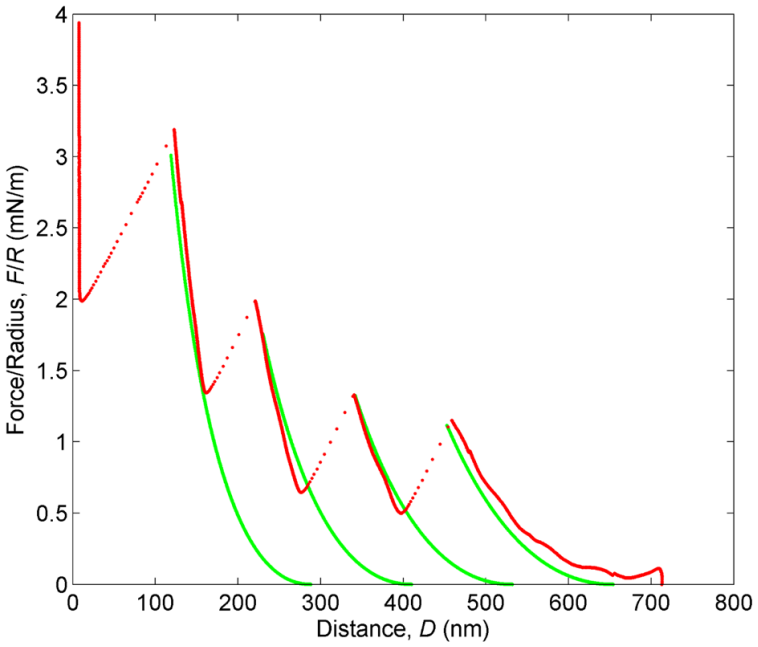

Figure 5.13 Force profile in green calculated by equation 4.6 based on the anchoring torque and strength obtained in Fig. 5.11, red lines are experimental results.

$$\gamma_s = \eta_s l_s \tag{5.18}$$

where η_s is boundary material viscosity, l_s is interaction length on boundary materials, ω is instant molecular rotation rate on surface, v is instant surface velocity.

From equation 5.16 and 5.17, $\omega = \frac{\partial \Phi}{\partial D} v$, thus equation 5.15 becomes,

$$K_{22}\left(\frac{\Phi}{D} - q_0\right) = \gamma_s \frac{\Phi}{D} v \tag{5.19}$$

In the third regime, the layers are squeezed one by one. Therefore, $\Phi \approx \Phi_0 = q_0 D_0$ at a large distance. Equation 5.19 becomes,

$$K_{22}(D_0 - D) = \gamma_s v D_0 \tag{5.20}$$

$$\gamma_s = \frac{K_{22}(D_0 - D)}{v D_0} \tag{5.21}$$

$$D = \frac{(K_{2\ 2} - \gamma_s v) D_0}{K_{2\ 2}} \tag{5.22}$$

Surface viscosity is estimated $\gamma_s = 1.8\ 3 \times 1\ 0^{-4}$ P a s · m, by equation 5.21 with typical $K_{2\ 2} = 6$ p N, $D_0 = 1\ 0\ 0$ n0m, $D_0 - D = 6\ 1$n m, $v = 2$ n m/s. If the interaction length on boundary materials is around 10 nm, then boundary material viscosity $\eta_s = 1.8\ 3 \times 1\ 0^{6}$ P a s, which is very large.

The surface viscous torque in equation 5.19 is integrated over Φ to calculate the surface viscous free energy $G_{s\ v}$ and surface viscosity γ_s is estimated by equation 5.21 at a large distance,

$$G_{s\ v} = \gamma_s \frac{\Phi^2}{2D} v \approx \frac{1}{2} K_{2\ 2} D_0^{\ 2} \frac{(D_0 - D) D_0}{D} \tag{5.23}$$

The force induced by surface viscosity is estimated about 0.8 mN/s at $D_0 = 1\ 0\ 0$n0m, which is very close to the background force in the third regime in Fig. 5.1. As a result, surface viscosity stretches cholesteric layers and the defects, in addition to the regular elastic forces. In some studies[183, 185-188] with smectics confined in SFA, defects also escaped to the surfaces under homeotropic anchoring that is typically weaker than planar anchoring. Given that the critical anchoring $2\sqrt{\frac{3}{8} K_{3\ 3} B}$ for surfaces to expel defects to the bisector plane[24] is larger for smectics than for cholesterics, defects in smectics were pinned on the surfaces. Those studies[186-188] explained the avalanche events by the stretch of screw dislocations pinned on surfaces. However, for cholesterics, defects are smaller amount with large layers compared to smectics. The pinned defects cannot be the only viscous force counted for the large background force. The sliding of whole cholesteric planes has to be taken into consideration. This may shed light on the commonly observed background forces in past studies[167, 178] with LCs.

5.3.4 Anchoring transitions

In more aged force profiles in the second regime, the forces cannot be fit very well with equation 4.6. However, when the water-induced anchoring transition on mica surfaces are taken into account, namely the intersection angle between anchoring axes changing 60 ° from 64.8 ° to 4.8 °, the force profiles can be fit very well. This indicates that the easy axis of mica changes discontinuously in the second regime after absorption of water, and that the third regime will be affected more by this anchoring transition after longer time evolution. However, the exact configuration of new easy axes could be many possibilities, if two surfaces are not changing symmetrically.

This reduction of anchoring angle α could be also due to the surface viscosity that hinders the anchoring deviation at weak anchoring to a certain angle, but this deviation, on average 30 ° on each surface, is rather small and happens to be similar to the angle of the anchoring transition. This anchoring deviation should also be continuous. Under such condition, the surface viscosity $\gamma_s = 2 \times 1\ 0^{-4}$ can be estimated by equation 5.19 with 10 integral layers, $K_{2\ 2} = 6$ p N, and $v = 2$ n m/s. This is consistent with the estimation in section 5.3.3.

5.4 Retardation of twist transitions

Fig. 5.14a-c show that the retardation of twist angle between retraction and approach exists in all the three regimes and decreases with the time evolution. Multiple-layer jumping events occur during approach in the first and second regime, and upon retraction in the third regime. Fig. 5.14e shows that the retardation during approach decreases with the time evolution. However, the retardation during retraction is the same in the first two regimes and a retardative jump is observed in the third regime, shown in Fig. 5.14f.

Notably, the twist angle profile during approach in the third regime is consistent with profiles during retraction in the first two regimes, shown in Fig. 5.14d. Most of the jumping points occur on quarter-pitch distances, but at the small distances, more uncertainties are observed.

In Fig. 5.14, all the non-integral layer has been deducted in order to eliminate the difference of the intersection angle between the easy axes among different experiments. The retardation among retractions results from viscous torque but the retardation among approaches varies with regimes. The anchoring torque hinders the jump during approach in the first regime, but the jump in the second regime might be due to both anchoring and viscous torque in addition to the incomplete coverage of mica and anchoring transitions. While in the third regime, viscous torque and anchoring transitions dominate the retardation.

Fig. 5.15 shows one example of anchoring transitions considering only the easy axis clockwise rotating 60 °on the top surface after water adsorption, which will be based for 4x4 matrix simulation. Other possibilities may also be feasible, as has been discussed in the last section.

Fig. 5.16b and 5.17b show the overlaid image of simulation and experiment spectrograms in the third regime, with twist angle profiles in Fig. 5.14c. During retraction, no anchoring transitions are considered while anchoring transitions with the configuration in Fig. 5.15b is considered during the approach. This indicates that bi-stable easy axes exist after water adsorption, and the new easy axis is another axis in addition to the possibilities shown in Fig. 2.14. The twist angle Φ either increases or decreases during retraction and approach respectively to minimize the elastic energy. Notably, there are some deviations between

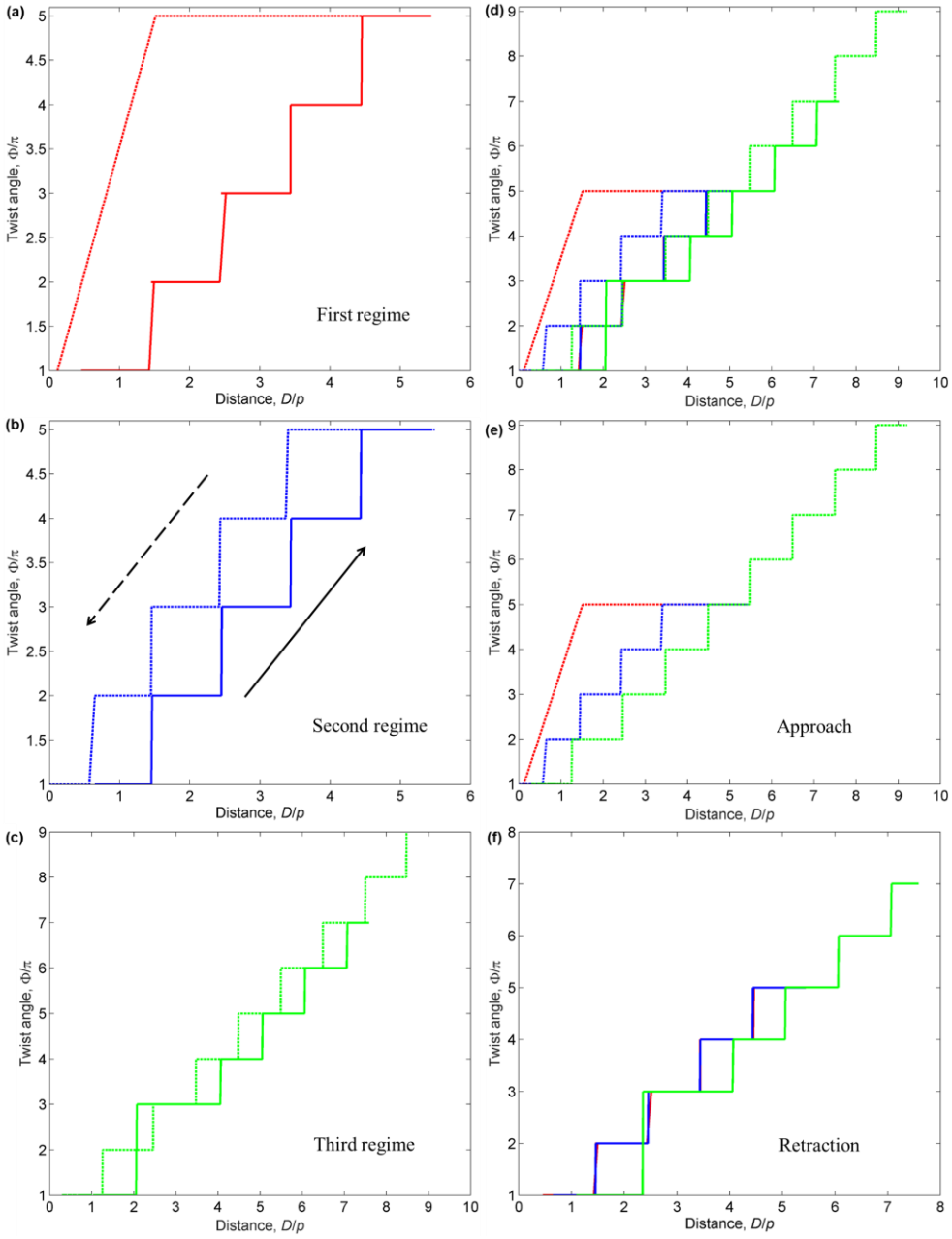

Figure 5.14 The retardation of the twist angle / as a function of distance *D*/*p* in three regimes, *p* is half-pitch and first non-integral layer has been deducted, and the deviation of anchoring angles is ignored. (a) First regime. The twist angle during the jump process is assumed to keep constant compression rate as the critical distance but decrease the total twist angle. (b) Second regime (c) Third regime, anchoring transitions are considered. (d) Three regimes (e) Approach profiles of three regimes (f) Retraction profiles of three regimes. Dash and sold lines are approach and retraction profiles of the twist angle respectively. Red, blue, green lines are first, second and third regimes respectively.

simulation and experiment, such as at frame 1500 and 2300, in Fig. 5.17b during the approach, manifesting that the deviation of anchoring angles occurs at small distances, which is reasonable since twist angle profiles in Fig. 5.14 are irregular at small distances. Apart from these deviations at small distances, the whole simulations in both Fig 5.16b and 5.17b seem to indicate a strong anchoring, which is not true. A possible reason would be that the anchoring strength deviates a small amount of the twist angle, such that the simulation always works with strong anchoring assumption.

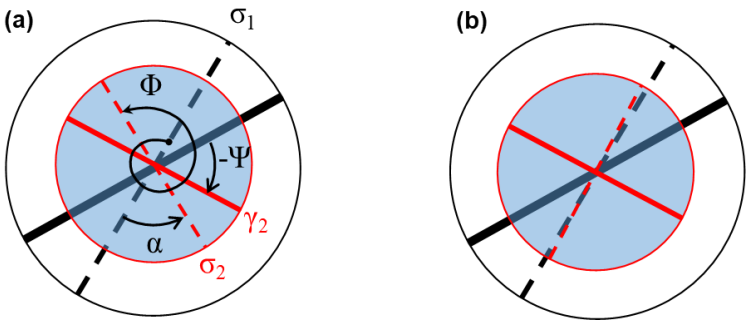

Figure 5.15 Two configurations of the mica setups with the intersection angle $\Psi = 57.4°$ of the mica. (a) Dry condition. The 30 ° easy axes bottom σ_1 and top σ_2 of surface anchoring to the index axes bottom γ_1 and top γ_2 of mica surfaces considering the right-handed cholesterics. (b) A possible configuration with the easy axis σ_2 of the top surface clockwise rotating 60 ° after water adsorption, leading to the anchoring angle $\alpha = 4.8$. The white disk with black lines and the blue disk with red lines correspond to the bottom and top mica respectively. The solid lines are the index axes while the dashed lines are easy axes. The counter-clockwise direction is positive. The total twist angle Φ is an example of $\Phi_0(n_0)$ with $n_0 = 1$ showing the twist angle of cholesterics from the σ_1 to σ_2 easy axis.

The simulations are compared with different twist angle profiles in Fig. 5.14c by subtracting or adding one or two layers, as shown in Fig. 5.16 and 5.17. Overall, the simulation changes significantly after one layer is subtracted, but makes small differences during the retraction and negligible differences during the approach by adding one or two

layers. Additionally, the simulation during approach in first and second regimes is also found not sensitive to the change of twist angle, because the layers are largely compressed, which is similar to the isotropic limit discussed in section 3.3.11. This indicates that with multiple twisted layers, the 4x4 matrices may not exactly reflect correct twist angles.

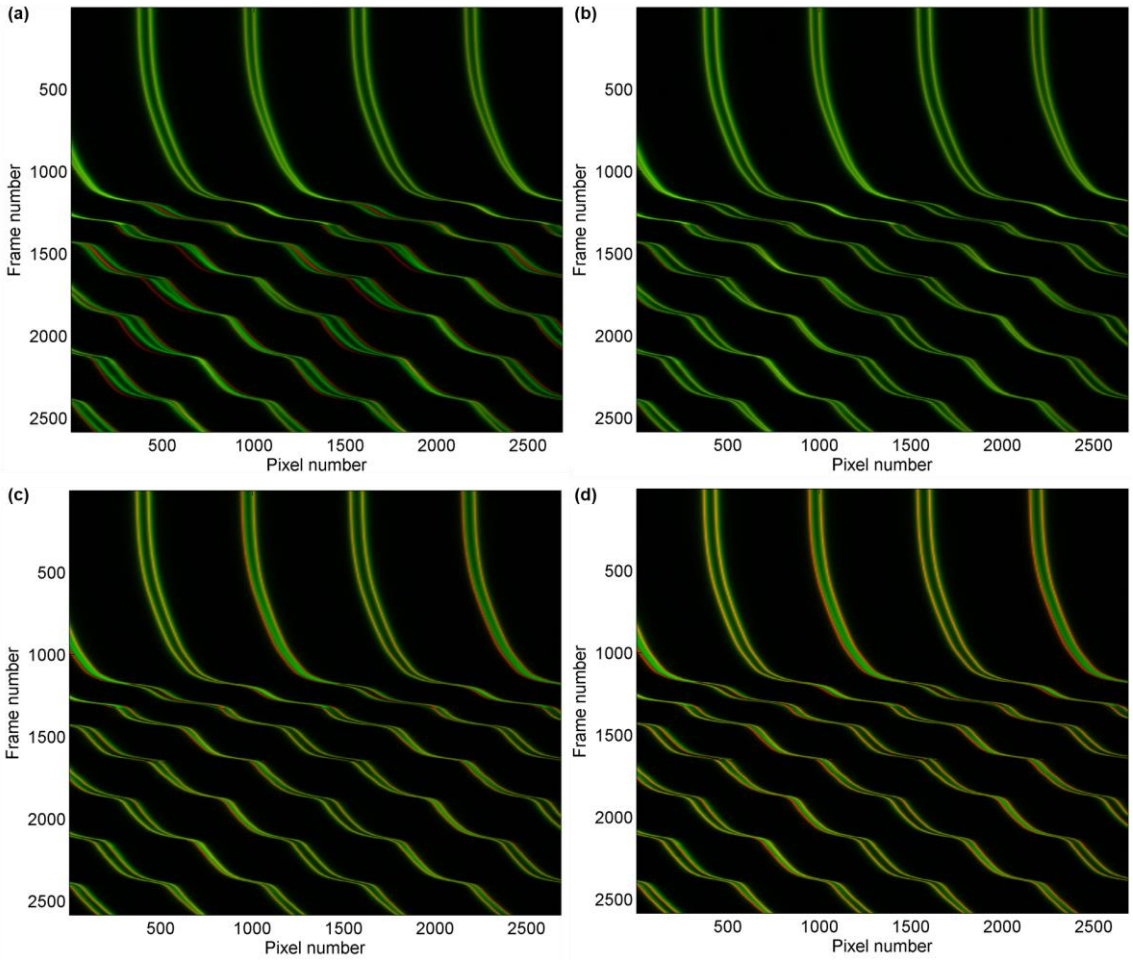

Figure 5.16 Overlay of simulation and experiment spectrograms during retraction in the third regime with the ImageJ, the configuration is based on the Fig. 5.15a. The twist angle in simulation is the corresponding twist angle profile in Fig. 5.14c (a) by subtracting π, (b) with no change, (c) by adding π and (d) by adding 2π. The frame number is proportional to the time, the thick green line is experimental data, the thin red line is the simulation data by, and the overlaid region shows yellow.

Certainly, the anchoring transitions could be just continuous anchoring deviation by the surface viscosity, as discussed in 5.3.4, and the simulation is still the same. More experiments are needed to see if the anchoring deviation is due to anchoring transition or surface viscosity.

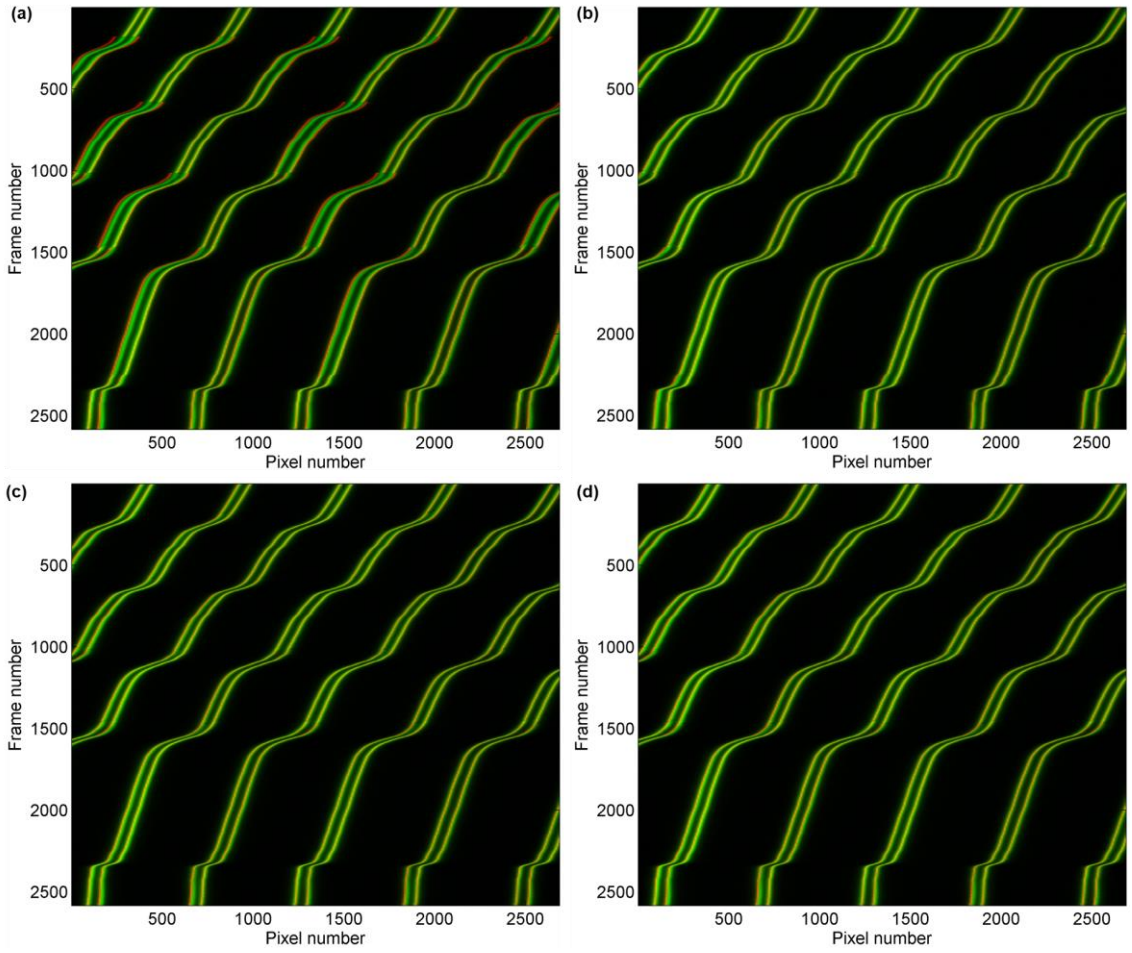

Figure 5.16 Overlay of simulation and experiment spectrograms during approach in the third regime with the ImageJ, the configuration is based on the Fig. 5.15b. The twist angle in simulation is the corresponding twist angle profile in Fig. 5.14c (a) by subtracting π, (b) with no change, (c) by adding π and (d) by adding 2π. The frame number is proportional to the time, the thick green line is experimental data, the thin red line is the simulation data by, and the overlaid region shows yellow.

5.5 Fractures and cracks in liquid crystals

During retraction and approach, the mechanical responses are very different, which can be understood by analogy to the fracture in solid materials. In order not to mix up the crack and defect in LCs, here only the defect that induces fracture is referred to the crack. During retraction, the innermost defect shrinks serving as a crack that finally breaks the

LCs, which is analogous to the opening mode in fracture mechanics, while in approach, defects move to a larger radius, such that they never become crack, but the whole layers are under shear stress that induces sliding or tearing mode in fracture mechanics, and the crack happens on either surface or interlayer.

The surface torque is analogous to the friction torque in rotational friction, which is consistent with the slip morphology on frictional substrates[216]. Recently a new paradigm[217-220] based on fracture mechanics is used to explain the transition between static and kinetic frictions. The energy dissipation during ruptures of lubricants is very high[220], such that most elastic energy is released by the heat and the rest of elastic energy is transferred to a new circle of the defect after jump events. As a result, the energy of defects is negligible to influence the position of jump and the force calculation, during both approach and retraction that is shown in section 4.3.2. This fracture energy that hinders the nucleation of a new defect loop is estimated, 10^{10} kT, by integrating the force profile over the working distance 300-1000 nm in the first regime, which is much larger than the defect energy, 10^{5} kT, with radius 3 5μm and line tension 10 pN.

In three regimes, the deviation of the anchoring axis provides evidence of interfacial ruptures during static rotational frictions. Therefore, both surface torque and retardation are unified within the framework described by ruptures and cracks in fracture mechanics.

There has been a lasting debate[18, 221] on the mechanism of stick-slip motions during friction. Three scenarios, one-layer or whole-layers melting and interlayer slip, are proposed[18]. It is difficult to distinguish the melting and the slip because the heat dissipation is high enough to melt molecular layers during stick-slip. However, from the anchoring deviation before slip, it might be more favourable to the scenario of interlayer slip that is also a signature of interfacial ruptures.

5.6 Summary

The stick-slip phenomenon widely exists in contact mechanics from the macroscale to the nanoscale. Here we observe three regimes, namely constrained, stick-slip and sliding-slip, with retardation during twist transitions under mechanical winding with different anchoring conditions, and measure corresponding forces by the SFA. The surface torque is adopted to analyze the threshold of the jump in different regimes and to estimate anchoring strength and surface viscosity. Both the surface torque and the retardation phenomena are discussed with fracture mechanics. Some conclusions are drawn as following,

(1) Compression rate of cholesteric layers before jumps decreases with the time evolution in three regimes. The forces experienced by surfaces in three regimes are mainly contributed by twist elastic energy but there exists a background force in addition to the oscillating elastic forces of the third regime.

(2) In the constrained regime, all the layers are compressed around 65 % before they are squeezed out together. There is almost no viscous dissipation under stress as the surface move quasi-statically. The effective coverage of mica on lenses is around 2/3, which decreases total elastic forces to 2/3 under large compressions.

(3) During jumping events, the slope of the force results from the balance of spring instabilities, twist elastic forces and bulk viscous forces in the first two regimes. On top of this, surface viscous forces share the balance in the third regime, and perhaps in aged second regimes.

(4) In the stick-slip regime, one or multiple layers jump at the distances slightly lower than the crossings among elastic forces of integral layers calculated with infinite anchoring, after about 30 % compression.

(5) In the sliding-slip regime, the layers jump one by one with a half-pitch period at a small compression rate, but large forces are encountered below 100 nm.

(6) Burgers vector may need to be taken into account at the distance larger than 10 integral cholesteric layers.

(7) All the measured forces are calibrated by single fitting parameter, velocity, which reasonably varies with runs among different experiments. Strain-stiffening is found to be natural especially in large compressions.

(8) All the jump behaviours in three regimes are results of a balance of twist elastic torque and surface torque, but the surface torque is consist of different factors. The critical jump threshold in the first regime is dominated by anchoring torque generated by anchoring strength $W = 0.1\ 5\text{m N/m}$ with the deviated angle $0.4\ 9\pi$ on one surface. However, in the second regime, the surface torque is attributed to both the anchoring torque and the viscous torque, anchoring transitions and coverage of mica, without a determined medium anchoring strength. In the third regime, the anchoring is weak and the viscous torque dominates jump threshold that is adapted by anchoring transitions.

(9) The deviated twist angle in the aged second regime and the third regime is due to either the discontinuous anchoring transitions after adsorption of water or the continuous anchoring deviation impeded by surface viscosity. The deviated twist angle with one possible configuration is analysed by 4x4 matrix simulation.

(10) The retardation of twist transitions in three regimes originates from the same mechanisms of jump threshold. Both the surface torque and the retardation are described within the framework of ruptures and cracks in fracture mechanics. The bulk crack as the opening mode in the bisector plane between two surfaces is mediated by the innermost defect and the interfacial ruptures as sliding or tearing mode are mediated by the surface torque. The ruptures determine the onset of slip from static rotational frictions to kinetic frictions, which are evidenced by the anchoring deviation and viscous retardation.

6 Conclusions and outlook

The Surface Forces Apparatus is used to simultaneously and precisely measure optics and mechanics of LCs under crossed-cylindrical confinement. As a result of the competition among surface anchoring, LC elasticity and confinement, rich morphologies of LCs are observed in both optical fringes and mechanical winding. Therefore, the index ellipsoid and 4x4 matrix are used to understand the optical interaction of multiple birefringent layers; the surface frictional torque and fracture mechanics are adapted to analyse twist transitions and stick-slip forces in this thesis.

LC status is found to be unstable during experiments and many studies in SFA, including anchoring transitions, background forces and the repeatability, discussed in Chapter 2, mainly on account of the sensitivity of LC molecules to the boundary conditions induced by the surface alignment and adsorption from ambient environments. As a consequence, examinations on anchoring transitions and careful cleaning and desiccated procedures are discussed in the experimental setup in Chapter 2, such that stable anchoring conditions are obtained and utilized to test the time evolution of samples.

The splitting of fringes generated by the MBI at contact positions in the SFA results from the birefringence and the intersection angle Ψ of the muscovite mica. The splitting changes linearly with $\cos\Psi$ at the contact, which depends on the phase retardation maximizing at the parallel configuration and minimizing at the perpendicular configuration. However, anisotropic LCs add more possibilities to the splitting of fringes. If the long axis of index ellipsoid of LCs is parallel with the bisector of the acute intersection angle of mica, the splitting of fringes keeps increasing and crosses with fringes generated by other chromatic orders, while in the perpendicular case, the phase

retardation is cancelled firstly resulting in a crossing within the same chromatic order before it increases. For random angle configurations, the crossing event within the same chromatic order is not observed and the behaviours of fringes can be intuitively understood by the composition of phase retardations with parallelogram rule that is similar to the geometrical composition of forces but with double intersection angle, discussed in Chapter 2. For chiral LCs, multiple crossings within the same chromatic order and bandgaps are observed with the separation of surfaces, simulated by 4x4 matrices.

Typically, average wavelengths in the same chromatic order and average refractive indices are used to calculate the surface separation for simplification, as if average wavelengths are generated by an isotropic medium with average refractive indices, referred as isotropic equivalence. In Chapter 3, 4x4 matrices are used to reconstruct the MBI from analysed data and to compare the deviation of isotropic equivalence, which produces the errors $\delta D/D$ in the order of 10^{-2}, acceptable for typical SFA measurements. It is shown that the resolution of the spectrometer is able to distinguish the differences of optics generated by LC molecules with different azimuthal angles and polar angles as small as 3 nm.

Under the confinement of crossed cylinders that is equivalent to a sphere approaching a flat plate, circular dislocation defects are formed. During quasi-equilibrium retraction of surfaces, cholesterics slip into the gap layer by layer with a period equal to half-pitch, producing twist transitions and structural forces. The 4x4 matrices are used to simulate the optics after analysis of the twist structures, with a fitting strong anchoring strength W = 0.8 mJ/m^2. The free energy is calculated with twist elastic energy and the Rapini-Papoular anchoring potential to fit structural forces. Although the innermost defect serves

as a bulk crack that breaks necks of cholesteric layers, the energy of defects is negligible compared with the change of elastic energy. An anomalous twist elastic constant K_{22} = 17 pN is used to fit the measured forces, which is attributed to the systematic errors, including viscous forces and the calibration of the motor speed.

Three regimes with the time evolution are observed in cholesterics during mechanical compression in the SFA. In the constrained regime, 65 % of layers are compressed before they are squeezed out altogether, and the deformation is mainly due to the strain-stiffening elasticity that sustains the compression without viscous dissipation, but the 2/3 effective coverage of mica decreases the total elastic forces. In the stick-slip regime, 30 % of layers are compressed before they are squeezed out layer by layer. In the sliding-slip regime, small compression is needed to squeeze out layers one by one and a background force is observed on top of oscillating elastic forces. The slope during jump results from a balance of spring instabilities, elastic forces and viscous forces.

The frictional surface torque that is analogous to friction torque in rotational friction is adopted to analyze the onset of three regimes. In the constrained regime with strong anchoring, the anchoring torque dominates while viscous torque dominates in the sliding-slip regime with weak anchoring. In the stick-slip regime, both the anchoring torque and viscous torque, as well as coverage of mica and anchoring transitions are possible to affect the stick-slip. The retardation of twist angles originates from the balance of twist elastic torque and surface torque.

Both the surface torque and retardation are within the paradigm of interfacial ruptures and cracks in fracture mechanics that are used to explain the onset from static frictions to kinetic frictions. During retraction, the innermost defect serving as a bulk crack of the

opening mode of fractures breaks the neck in the middle plane of integral layers. During the approach, the deviation of anchoring and viscous retardation serving as interfacial ruptures of tearing or sliding mode of fractures determine the critical jump threshold.

This thesis provides a new method based on the critical surface torque to measure strong anchoring that is usually difficult to measure the anchoring deviation under the polarized microscope. The twist elastic constant can be extracted preciously from the force measurement provided that the motor speed is *a priori* known. The time evolution of anchoring suggests that surface viscosity is measurable and may play big roles in the LC morphologies at weak anchoring or after adsorptions of external molecules especially water from ambient environments. This study reveals the importance and complexity of boundary conditions on LCs and sheds light on the puzzles in past studies such as anchoring transitions, background forces, the repeatability and permeative flows[190, 222]. It would be also interesting to study how the ions, water or other molecules on mica affect the surface physics and the corresponding anchoring[154], given that the computational chemistry[77, 78] is becoming a useful tool to predict the energy interaction between surfaces and external molecules. For example, the nitrogen with controlled humidity could be purged to test the effect of water adsorption on the three regimes and the surface anchoring could be modified with various methods described in section 1.4.1 and 2.2 to reach other possible regimes in the future. Similarly, the cholesteric-nematic unwinding could show discontinuous transitions with various surface anchoring under external fields, such as temperature, stress, light, electric and magnetic fields, which opens new possibilities for the design of tuneable self-healing laser. Apart from LCs, boundary conditions are crucial to yield stress materials[209, 223], frictions[18], adhesions[224], nanoparticle additives[225] and biomechanics[226]. For example, the time scale and wall slip

change the rheology measurement of the apparent viscosity in yield stress materials as much as a few orders[209, 223].

The surface anchoring increases the order parameter of LC molecules and the temperature of nematic-isotropic transitions[17], which may generate repulsive order-parameter-related forces[178]. It is intriguing to see the nature of parameter-related forces, and if the boundary layer will melt into bulk transition[17] during nematic-isotropic transitions in the SFA by measuring the order parameter with precise control of temperature. The application of electric fields adds further controllable constraints to the LCs, which opens up new possibilities on the tuneable optics and frictions with the analysis of 4x4 matrix simulation.

Overall, three regimes mediated by the fracture mechanics offer new insight into avalanches[183], earthquakes[217-220] and the design of materials with new properties, such as blue phases[227], lubricants[220], nanomotors[228, 229], lasing[59], anisotropic diffusion[103-106] and strain-stiffening[211]. The controllable position of defects changing with anchoring strength[24] provides a new understanding of crack-free materials. The geometrical understanding of phase retardation with multiple birefringent layers helps the comprehension of topological photonics[230].

Publications

1. ***Zheng W.***, *Perez-Martinez C S, Petriashvili G, Perkin, S., Zappone, B.* Direct measurements of structural forces and twist transitions in cholesteric liquid crystal films with a surface force apparatus. ***Soft matter***, 2019, **15**: 4905-4914 (Chapter 4).

2. *Zappone B,* ***Zheng W.***, *Perkin S.* Multiple-beam optical interferometry of anisotropic soft materials nanoconfined with the surface force apparatus. ***Review of Scientific Instruments***, 2018, 89(8): 085112 (Chapter 3).

3. *Barbero G,* ***Zheng W.***, *Zappone B.* Twist transitions and force generation in cholesteric liquid crystal films. ***Journal of Molecular Liquids***, 2018, 267: 242-248 (Chapter 4).

Acknowledgements

I am grateful that my family supports my abroad study in different countries and understands me, as my most powerful backing. And I didn't let them down during the PhD, as a person they educate me to be. My little nephew always accompanies me and I am watching him grow up, as if I am catching a glimpse of my own childhood and my own personality before memory began.

I would like to thank Bruno's training on the SFA, especially on the MATLAB programming and the 4x4 matrix simulation. I am grateful that he revised the papers and this thesis, and that he provided me an opportunity to visit and collaborate with Perkin group at the University of Oxford, where Susan offers a lab with freedom, equality and respect. Susan allows me to think boldly and crazily and helps me to realize those ideas that finally become valuable. In my most difficult times during the PhD, she trusted me and guided me to get through. I also appreciate her revisions on the papers and the thesis.

I also would like to thank my colleagues who constantly helped me during my PhD. Carla trained me on the SFB and helped me on experiments even after midnight. Romain always provided constructive advice and mathematical skills on experiments and theories. James revised the first chapter of the thesis and I always bothered him questions in the office and during lunchtime. Hannah provided the figure of the silvered mica and allowed me to occupy the SFB for a whole week during the time evolution. Because of Tim's revision, my thesis now is full of posh articles, "a", "an" and "the", which generously contribute lots of words for me. Alfredo helped me to translate the abstract into Italian. Roberto had a discussion with me on a piece of old literature. Meanwhile, I am very grateful for other wonderful colleagues who helped me during my PhD. I quite enjoyed

different homemade cakes by colleagues, such as Brownie, which turned the bitter PhD to be so sweet.

I have been very fortunate to be an Early-Stage Researcher of the “NANOTRANS” Marie-Curie network during my last year of PhD hosted by Perkin group, and I enjoyed the workshop with those students and professors in the network.

Lots of people, including friends, administrative staff and technicians, in Italy, the UK and China have been providing very useful supports and advice for my PhD. Chiara always patiently and kindly helped me on the administrative paperwork. Maria supported materials and equipment for my experiments. Without their understanding and generosity, I could not accomplish my PhD.

Appendix

A Symbols

n	Liquid crystal director
S	Order parameter
δ	Deviation angle between molecular axis and the director or easy axis
G	Free energy per unit area
$K_{1\ 1}$	Splay elastic constant
$K_{2\ 2}$	Twist elastic constant
$K_{3\ 3}$	Bend elastic constant
P	Pitch
λ	Wavelength
λ_o	Ordinary wavelength
λ_e	Extraordinary wavelength
μ_o	Ordinary refractive index
μ_e	Extraordinary refractive index
D	Surface separation distance
δ_0	Deviation angle at zero distance
δ_y	Deviation angle at distance y.
δ_D	Deviation angle at distance D.
L	Extrapolation length
W	Anchoring strength or anchoring energy coefficient
a	Distance within which molecules are affected by the wall
G_s	Surface free energy per unit area
θ_0	Polar angle of molecules at the easy axis

φ_0 Azimuthal angle of molecules at the easy axis

θ Polar angle

φ Azimuthal angle

$G_s(\theta_0, \varphi_0)$ Free energy function at the easy axis

$W(\theta - \theta_0, \varphi - \varphi_0)$ A function that describes anchoring strength at deviated polar angle θ and azimuthal angle φ

$G_s(\theta)$ Free energy of polar anchoring

W_0 Anchoring coefficient that is not related to angle

W_p Polar anchoring coefficient or polar anchoring strength

$\mathbf{n}_0$ Director on the easy axis

a_m Molecular dimension

W_a Azimuthal anchoring coefficient or azimuthal anchoring strength

θ_x Projecting angle of director on *x* axis

θ_y Projecting angle of director on *y* axis

G_c Critical surface energy potential

S_c Critical order parameter

G_d Free energy density

ε_0 Dielectric constant of vacuum

$\Delta\varepsilon$ Dielectric anisotropy of LCs

E Electric field strength

E_c Critical electric field strength

V_c Critical voltage threshold

H_c Critical magnetic threshold

$\Delta\chi$ Diamagnetic anisotropy

P_0 Original pitch

n Integral number

R Radius of cylinder

r	Lateral radius from the minimum surface separation point
h	Height of surfaces
μ	Average refractive index of medium
λ_n^0	Wavelength of the n^{th} fringes at $D = 0$
$\mu_{mi\ c\ \alpha}$	Average refractive index of mica
$\bar{\mu}$	Ratio of average refractive index of mica and average refractive index of medium
α	Refractive index axis of mica at α axis
β	Refractive index axis of mica at β axis
γ	Refractive index axis of mica at γ axis
t	Time
F	Surface force
$F(t)$	Surface force at time t
k	Spring constant
D_0	Original surface distance
$D(t)$	Surface distance at time t
v	Motor speed
R_1	Radius of first cylinder
R_2	Radius of second cylinder
T	Thickness of mica
R_t	Phase retardation
R_{t1}	Phase retardation of the first layer
R_{t2}	Phase retardation of the second layer
λ_β	Optical polarization by β index axis of mica
λ_γ	Optical polarization by γ index axis of mica
Ψ	Acute intersection angle between longest index axes of two birefringent layers.
ε	Acute intersection angle between complex ellipsoid and first-layer ellipsoid

σ	Easy axis
$T_{C\ T\ A\ B}$	Thickness of CTAB coating
$\delta\lambda$	Deviation of two wavelengths
Φ	Twist angle of LCs
B	Compression constant
l_n	Relaxed length of integral n layers
l	Length of integral n layers after stretch or compression
Δl_n	Compression length of integral n layers
δD	Distance deviation
η	Viscosity
ν	Oscillating frequency
A_0	Applied amplitude
A	Measured amplitude
σ_1	First easy axis
σ_2	Second easy axis
$r_{d,n}$	Radius of n^{th} defect
q	Prime fringe, an odd chromatic order of fringe at contact position
Fnum	Sign of chromatic order for calculation, odd (Fnum = 1) or even (Fnum = -1)
γ_1	Longest index axis of first mica surface
γ_2	Longest index axis of second mica surface
u	Projected molecular director on *x*-*y* plane
λ_i	Equivalent isotropic wavelength
$h_{0,n}$	Height of the relaxed *n* layers
$h_{d,n}$	Height of the defect between n^{th} and n+1th layers
n_0	The number of half-turns or half-pitches or layers
p	Half pitch

α	Intersection angle of the easy axes
$\Phi_0(n_0)$	Total twist angle of n_0 half-turns
D_c	Critical thickness of the twist transition
φ’	Molecule rotation rate at certain distance
q_0	Intrinsic molecule rotation rate
h_c	Critical height of twist transition
D_1	First surface position
D_2	Second surface position
D_n	Surface separation of n layers
$r_d(i)$	The radius of i^{th} defect
T_d	Line tension of dislocation
E_n	The free energy of n layers moving from D_n to D_c
ΔE	Free energy change
$r_{d,n}(D_c)$	The radius of smallest defect with n layers at the distance D_c
b	Burgers vector
$h_{b\ c}$	Critical distance of Burgers vector changing from $b = p$ to $b = 2p$
α_w	Wedge dihedral angle
Π	Force per unit area, pressure
E_y	Young’s modulus
γ_s	Surface viscosity
Γ_a	Anchoring torque
Γ_e	Elastic torque
Φ_0	Original twist angle
Γ_c	Critical torque threshold
ω	Instant molecular rotation rate on surface
η_s	Boundary material viscosity

l_s Interaction length on boundary materials

$G_{s\ v}$ Free energy by surface viscosity

F_n A factor for correcting the dispersion of refractive index and phase change of silver mirrors

Y_δ Apparent reduction of thickness

B Abbreviations

AFM	Atomic Force Microscope
Cd-arachidate	Cadmium arachidate
C T A B	Cetyltrimethyl Ammonium Bromide
DHDAA	Dihexadecyldimethyl ammonium acetate
FECO	Fringes of Equal Chromatic Order
GSFB	Graphene Surface Force Balance
I	Isotropic
ITO	Indium tin oxide
LC	Liquid crystal
MBI	Multiple-beam interferometry
MEMS	Micro Electro Mechanical Systems
N	Nematic
OTS	Octadecyl-trichloro-silane
SmC	Smectic C
SmA	Smectic A
SDL	Screw dislocation line
SFA	Surface Forces Apparatus
SFB	Surface Force Balance
TOC	Total organic carbon

C Mica-mica contact calibration

C.1 Mercury lines and FECOs at contact position

Mercury lines with known wavelengths are recorded as a reference to the FECOs after bringing the mica surfaces into the contact position. The mercury lines used are shown without the FECO in Fig. C.1a, where the bright line is the Hg green line with wavelength 546.075 nm, and the faint yellow lines have wavelengths of 576.961 and 579.067 nm respectively. Usually, the green and farther yellow lines are used for calibration assuming that the grating is linear. In a real experiment, one of the odd fringes selected as prime fringe q is roughly moved to position 300 pixels by changing grating, to maximize its moving range, as shown in Fig. C.1c. Consequently, the new reference is recorded in Fig. C.1b after moving grating. Each of the fringes is split into a doublet as a result of the birefringent nature of mica that depends on the intersection angle of mica surfaces. More details about how mica intersection angle influences splitting of the doublet are discussed in sections C.3 and 3.3.8.

In Fig. C.1c, the flattened area of the fringes indicates flattened contact of mica surfaces where surface separation $D = 0$ shown in Fig. 2.1c. However, the shape of fringes outside the contact region in different chromatic orders are not the same, depending on the parity of chromatic order which can be distinguished by simplified formulas of distance calculation. In equation 2.2, for a small distance, $\sin[\pi(1-\lambda_n^0/\lambda_n^D)/(1-\lambda_n^0/\lambda_{n-1}^0)] \approx \pi(1-\lambda_n^0/\lambda_n^D)/(1-\lambda_n^0/\lambda_{n-1}^0)$, $\cos[\pi(1-\lambda_n^0/\lambda_n^D)/(1-\lambda_n^0/\lambda_{n-1}^0)] \approx 1$, and $\tan(2\pi\mu D/\lambda_n^D) \approx 2\pi\mu D/\lambda_n^D$, thus equation 2.2 becomes,

$$D = n(\lambda_n^D - \lambda_n^0)/2\mu_{mica} \quad \text{for odd } n, \tag{C.1}$$

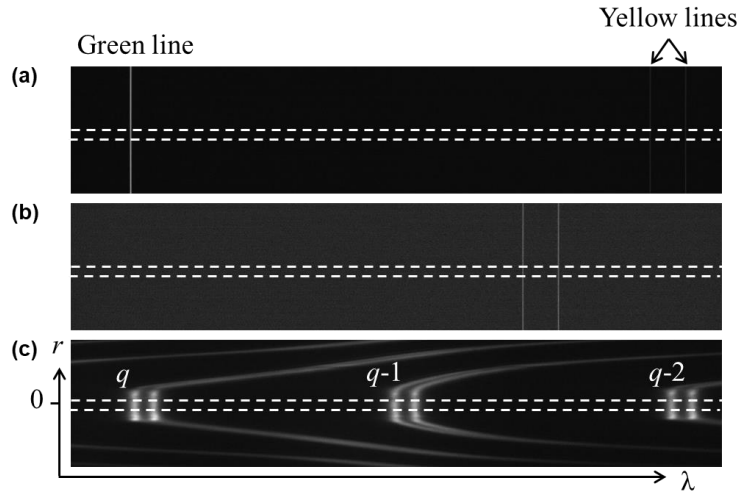

Figure C.1 Mica-mica contact calibration: (a) Hg green and yellow lines before moving grating. The slit of the spectrometer is slightly open to make sharp mercury lines, such that yellow lines are very faint. (b) Hg yellow lines and (c) FECOs *q*, *q*-1 and *q*-2 after moving grating, λ is wavelength and r is the radius from the closest surface separation point in Fig. 2.1c. Dashed lines indicate the cropped region for analysis.

$$D = n(\lambda_n^D - \lambda_n^0)\mu_{mica}/2\mu^2, \quad \text{for even } n, \tag{C.2}$$

The above equations show that at a small distance the odd fringes do not depend on the refractive index of the medium, while the even ones are affected by the medium. Equation C.2 can be used to estimate the refractive index μ of an unknown medium used in the SFA and also reveals the origin of the shape difference of fringes. For odd fringes, the wavelength change is proportional to $2\mu_{mica}D/n$, but for even ones, it is proportional to $2\mu^2/n\mu_{mica}$. If $\mu < \mu_{mica}$, for example, in the air with $\mu = 1$, the slope of the wavelength $d\lambda/dr$ in odd fringes will be much larger than in even fringes, which is exactly the case in Fig. C.1c where odd fringes are much sharper than even ones. Only when $\mu = \mu_{mica}$ can one get the same shape of fringes at small separations.

C.2 Peak detection

The centre area with a height of 30 pixels between the dashed lines in Fig. C.1 is the surface contact region where each image is cropped for analysis. Hg lines are narrow and sharp enough for a direct plot of grey value after being averaged with 30 pixels by MATLAB, as shown in Fig. C.2 where images are left-right flipped before detection to allow comparison between the SFA and the SFB using different arrangements of the spectrometers.

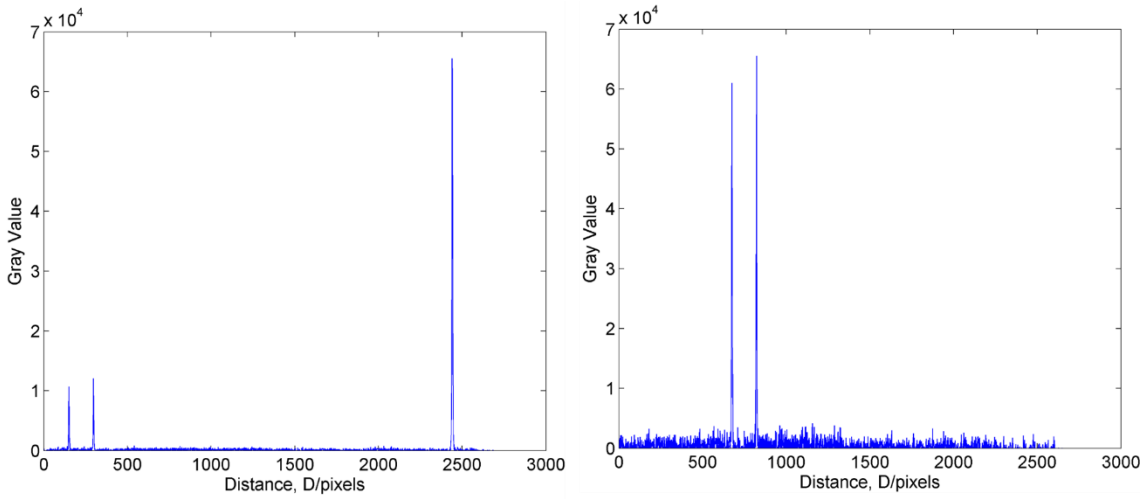

Figure C.2 Peak detection of Hg lines (a) before and (b) moving grating. The images are cropped, averaged and left-right flipped before detection.

The observed fringes are much broader than the Hg lines, so position detection is not so direct. In multiple-beam interferometry, the fringe can be sharp by coating thick mirrors on the back of mica, but some trade-off is considered between the balance of light width and intensity that can be detected by the camera with reasonable exposure time. Therefore, a double Lorentzian function is applied to detect the peak, i.e. position of maximum intensity peak of the FECO line by line, before which the image is left-right flipped. Also, uninterested regions are tagged and excluded by foreground colour before detection. The tagged regions in Fig. C.3 limit the peak detection of different fringes to certain areas,

which also decreases the error when the intensity of the fringes changes as a result of fringe crossing or non-symmetry. After detection, all the peak positions of the fringes are highlighted with red dots, of which values are saved to an Excel file for the next stage of the analysis.

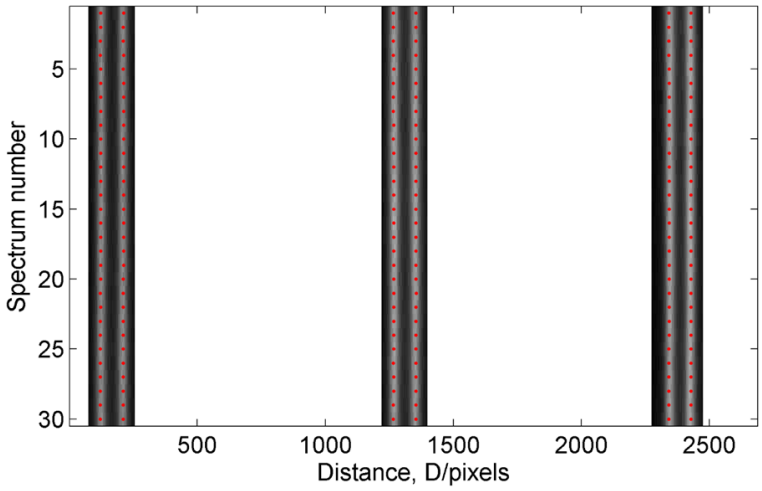

Figure C.3 Peak detection of FECO in Fig. C.1c by double Lorentzian function, where red dots are the peak positions of each line. The image is left-right flipped and tagged by foreground colour before detection.

C.3 Thickness and intersection angle of mica surfaces

The detected data in Fig. C.2 and Fig. C.3 are analysed in Table C.1, where the doublet of each fringe is labelled by the corresponding refractive index that gives rise to it. Subsequently, peak values in Fig. C.3, are averaged and converted into wavelengths based on the reference Hg lines. Next comes to the calculation of the refractive index of mica μ_{mica}, nF_n, n, the apparent thickness of mica Y, phase change by reflection on the silver mirror and phase retardation of birefringence, which all rely on the wavelength of two adjacent fringes. The following equations are used for all the calculations,

$$\mu_\gamma = 1.5\ 9\ 5 + 34.7\ 6 \times 1\ \theta / \lambda^2\ (\text{Å}) \qquad \text{(C.3)}$$

$$\mu_\beta = 1.5\ 97\ 0 + 4.7\ 6 \times 1\ \ 0^{5}/\lambda^2\ (\text{Å}) \quad \text{(C.4)}$$

where the refractive indices of brownish mica μ_β and μ_γ are a function of wavelength.

$$nF_n = \lambda_{n-1}/(\lambda_{n-1} - \lambda_n) \quad \text{(C.5)}$$

$$F_n \approx 1.0\ \ 2 - 1/n \quad \text{(C.6)}$$

where F_n is a factor for correcting the dispersion of the refractive index and phase change of silver mirrors. Chromatic order *n* obtained from equation C.5,6 usually is not an integer, but with the correction factor F_n, it will be very close to an integer which can be calculated by rounding. Note that F_n and *n* for the *q*-2 fringe for which the calculation relies on the *q*-3 fringe cannot be directly obtained from the wavelength data. The integer *n* is calculated from the *q*-1 and *q* fringes As a result, 3 fringes at contact are sufficient for checking the self-consistency of chromatic order.

With the parameters analysed above, the apparent thickness of mica is calculated with two-layer mica interference in equation C.7, where *Y* is the thickness of a single mica layer.

$$n\ \lambda = 4\mu_{mi\ \ c} Y_a \quad \text{(C.7)}$$

Table C.1 shows that the deviation of mica thickness *Y* found in different chromatic orders is a few nanometres, indicating strong phase change of silver layers. By taking into account this phase change and dispersion with empirical equation C.8, the deviation of the real thickness *Y* is only a few angstroms.

$$Y_\delta = b_0 + b_1\lambda + b_2\lambda^2 + b_3\lambda^3 \quad \text{(C.8)}$$

Where Y_δ is the apparent reduction of thickness which is negative, thus real thickness is larger than apparent thickness. The constants b_0, b_1, b_2 and b_3 valid for 50 nm silver are obtained from the literature[193].

The intersection angle Ψ of mica results in a change of the splitting of the fringes in different setups of experiments. The effective birefringence is a function of cosΨ given by[170, 171],

$$\Delta\mu_\Psi = \Delta\mu \cos\Psi \tag{C.9}$$

$$\Delta\mu_\Psi \approx (\lambda_\gamma^0 - \lambda_\beta^0)\mu_{mica}/\bar{\lambda} \tag{C.10}$$

Where $\Delta\mu_\Psi$ is effective birefringence at a certain angle Ψ, $\bar{\lambda}$ is the average wavelength of fringes with the same chromatic order, while $\Delta\mu = \mu_\gamma - \mu_\beta$ is the maximum birefringence of mica.

Finally, the real thickness Y and intersection angle Ψ of mica from each fringe are calculated and averaged for further analysis. For the experiment in Fig. C.1, the real thickness of a single layer mica Y = 3.1000 μm, while the intersection angle between two mica layers is Ψ = 46.8 °.

Parity of fringe		*q*-2, odd		*q*-1, even		*q*, odd		
Hg line/Fringe	Hg yellow	γ	β	γ	β	γ	β	Hg green
λ (pix)	675.5	121.9	211.4	1266.8	1353.7	2342.8	2427.9	2965.5
λ (Å)	5790.67	5870.4	5857.5	5705.5	5693.0	5550.5	5538.2	5460.75
Average λ (Å)		5864.0		5699.2		5544.3		
μ_{mica}		1.598	1.593	1.599	1.594	1.600	1.595	
Average μ_{mica}		1.596		1.597		1.597		
nF_n		-		35.59		36.80		
n		-		33.78134		34.95676		
Integer *n*		33		34		35		
Apparent *Y* (Å)		30314.9		30340.5		30368.3		
Apparent *Y* (μm)		3.0315		3.0341		3.0368		
Y_δ (nm)		-68.6	-68.6	-65.9	-65.9	-63.3	-63.3	
Average Y_δ (nm)		-68.6		-65.9		-63.3		
Real *Y* (μm)		3.1001		3.0999		3.1001		
$\Delta\mu_\Psi$		0.00351		0.00351		0.00354		
cosΨ		0.68270		0.68352		0.68901		
Ψ ( )		46.9		46.9		46.4		

Table C.1 The procedure for calibration of thickness and intersection angle of mica based on FECO and reference of Hg lines.

C.4 Shape of fringes at contact

As has been discussed in section C.1, the shape of odd and even fringes depends on the refractive index of the medium, as shown in Fig. C.4a for the case in air. After injection of 5CB, with refractive indices close to those of mica, and bringing to contact again, the parity of fringes is indistinguishable in Fig. C.4b. However, one can still estimate the contact geometry by checking the shape of fringes. Fig. C.4c,d correspond to the geometry that produces the fringes shown in Fig. C.4a,b. Although Fig. C.4b is at contact position, the existence of liquid molecules reduced surface adhesion such that surfaces are not flattened. However, if the surfaces are crushed with a high speed of motor approach, the contact could be totally deformed, for instance, one more drastic fringe shape is shown in Fig. C.4e,f, where surfaces are squeezed into a concave shape with some liquids stored inside.

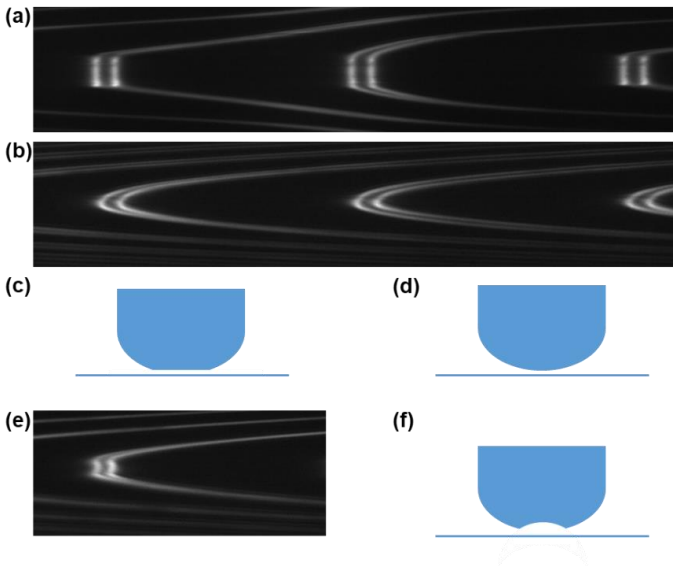

Figure C.4 Different shapes of fringes observed for two surfaces at contact: (a) Mica-mica contact in the air before injection and (b) after injection of 5CB, which correspond to the shape of contact geometry (c) and (d) respectively. (e) Example of concave fringe and (f) schematic diagram of contact geometry.

In brief, the fringes at contact usually reflect the shape of contact geometry, which can be used to examine the radius of the cylinders R, integrity of the surfaces, cleanness of the liquid, capillary condensation or even molecular orientation.

References

1. Beller, D.A. et al. Geometry of the Cholesteric Phase. *Physical Review X* **4**, 031050 (2014).
2. De Gennes, P.-G. & Prost, J. The physics of liquid crystals (Clarendon Press, Oxford, 1993).
3. Dierking, I. & Al-Zangana, S. Lyotropic Liquid Crystal Phases from Anisotropic Nanomaterials. *Nanomaterials* **7**, 305 (2017).
4. Chuang, I., Durrer, R., Turok, N. & Yurke, B. Cosmology in the Laboratory - Defect Dynamics in Liquid-Crystals. *Science* **251**, 1336-1342 (1991).
5. Grelet, E. & Fraden, S. What is the origin of chirality in the cholesteric phase of virus suspensions? *Physical Review Letters* **90**, 198302 (2003).
6. Tortora, M.M.C. & Doye, J.P.K. Hierarchical bounding structures for efficient virial computations: Towards a realistic molecular description of cholesterics. *Journal of Chemical Physics* **147**, 224504 (2017).
7. Mitov, M. Cholesteric liquid crystals in living matter. *Soft Matter* **13**, 4176-4209 (2017).
8. Hough, L.E. et al. Chiral Isotropic Liquids from Achiral Molecules. *Science* **325**, 452-456 (2009).
9. Jeong, J. et al. Chiral structures from achiral liquid crystals in cylindrical capillaries. *Proceedings of the National Academy of Sciences of the United States of America* **112**, E1837-E1844 (2015).
10. Eelkema, R. & Feringa, B.L. Amplification of chirality in liquid crystals. *Organic & Biomolecular Chemistry* **4**, 3729-3745 (2006).
11. Lettinga, M.P. & Grelet, E. Self-diffusion of rodlike viruses through smectic layers. *Physical Review Letters* **99**, 197802 (2007).
12. Bohle, A.M., Holyst, R. & Vilgis, T. Polydispersity and ordered phases in solutions of rodlike macromolecules. *Physical Review Letters* **76**, 1396-1399 (1996).
13. Bolhuis, P. & Frenkel, D. Tracing the phase boundaries of hard spherocylinders. *Journal of Chemical Physics* **106**, 666-687 (1997).
14. Bates, M.A. & Frenkel, D. Influence of polydispersity on the phase behavior of colloidal liquid crystals: A Monte Carlo simulation study. *Journal of Chemical Physics* **109**, 6193-6199 (1998).
15. van der Kooij, F.M., Kassapidou, K. & Lekkerkerker, H.N.W. Liquid crystal phase transitions in suspensions of polydisperse plate-like particles. *Nature* **406**, 868-871 (2000).
16. Lettinga, M.P. Viruses as colloidal model systems (2004).
17. Sheng, P. Boundary-Layer Phase-Transition in Nematic Liquid-Crystals. *Physical Review A* **26**, 1610-1617 (1982).
18. Israelachvili, J.N. Intermolecular and surface forces (Academic press, 2011).
19. Israelachvili, J.N., Mitchell, D.J. & Ninham, B.W. Theory of Self-Assembly of Hydrocarbon Amphiphiles into Micelles and Bilayers. *Journal of the Chemical Society-Faraday Transactions Ii* **72**, 1525-1568 (1976).
20. Nagarajan, R. Molecular packing parameter and surfactant self-assembly: The neglected role of the surfactant tail. *Langmuir* **18**, 31-38 (2002).

21. Damasceno, P.F., Engel, M. & Glotzer, S.C. Predictive Self-Assembly of Polyhedra into Complex Structures. *Science* **337**, 453-457 (2012).
22. Goodby, J.W., Mandle, R.J., Davis, E.J., Zhong, T. & Cowling, S.J. What makes a liquid crystal? The effect of free volume on soft matter. *Liquid Crystals* **42**, 593-622 (2015).
23. Miesowicz, M. The 3 Coefficients of Viscosity of Anisotropic Liquids. *Nature* **158**, 27-27 (1946).
24. Smalyukh, I.I. & Lavrentovich, O.D. Anchoring-mediated interaction of edge dislocations with bounding surfaces in confined cholesteric liquid crystals. *Physical Review Letters* **90**, 085503 (2003).
25. Dammone, O.J. et al. Confinement Induced Splay-to-Bend Transition of Colloidal Rods. *Physical Review Letters* **109**, 108303 (2012).
26. Smalyukh, I.I. Liquid Crystal Colloids. *Annual Review of Condensed Matter Physics* **9**, 207 (2018).
27. Sidky, H., de Pablo, J.J. & Whitmer, J.K. In Silico Measurement of Elastic Moduli of Nematic Liquid Crystals. *Physical Review Letters* **120**, 107801 (2018).
28. Kos, Z. & Ravnik, M. Relevance of saddle-splay elasticity in complex nematic geometries. *Soft Matter* **12**, 1313-1323 (2016).
29. Pairam, E. et al. Stable nematic droplets with handles. *Proceedings of the National Academy of Sciences of the United States of America* **110**, 9295-9300 (2013).
30. Kuksenok, O.V., Ruhwandl, R.W., Shiyanovskii, S.V. & Terentjev, E.M. Director structure around a colloid particle suspended in a nematic liquid crystal. *Physical Review E* **54**, 5198-5203 (1996).
31. Lubensky, T.C., Pettey, D., Currier, N. & Stark, H. Topological defects and interactions in nematic emulsions. *Physical Review E* **57**, 610-625 (1998).
32. Stark, H. Physics of colloidal dispersions in nematic liquid crystals. *Physics Reports-Review Section of Physics Letters* **351**, 387-474 (2001).
33. Gu, Y.D. & Abbott, N.L. Observation of Saturn-ring defects around solid microspheres in nematic liquid crystals. *Physical Review Letters* **85**, 4719-4722 (2000).
34. Senyuk, B., Puls, O., Tovkach, O.M., Chernyshuk, S.B. & Smalyukh, I.I. Hexadecapolar colloids. *Nature Communications* **7**, 10659 (2016).
35. Zhou, Y., Senyuk, B., Zhang, R., Smalyukh, I.I. & de Pablo, J.J. Degenerate conic anchoring and colloidal elastic dipole-hexadecapole transformations. *Nature Communications* **10**, 1000 (2019).
36. Park, S., Liu, Q.K. & Smalyukh, I.I. Colloidal Surfaces with Boundaries, Apex Boojums, and Nested Elastic Self-Assembly of Nematic Colloids. *Physical Review Letters* **117**, 277801 (2016).
37. Meyer, R.B., Stebler, B. & Lagerwall, S.T. Observation of Edge Dislocations in Smectic Liquid-Crystals. *Physical Review Letters* **41**, 1393-1395 (1978).
38. Repula, A. & Grelet, E. Elementary Edge and Screw Dislocations Visualized at the Lattice Periodicity Level in the Smectic Phase of Colloidal Rods. *Physical Review Letters* **121**, 097801 (2018).
39. Chen, K., Metcalf, L.P., Rivas, D.P., Reich, D.H. & Leheny, R.L. Anisotropic colloidal transport and periodic stick-slip motion in cholesteric finger textures. *Soft Matter* **11**, 4189-4196 (2015).

40. Wang, X.G., Miller, D.S., Bukusoglu, E., de Pablo, J.J. & Abbott, N.L. Topological defects in liquid crystals as templates for molecular self-assembly. *Nature Materials* **15**, 106 (2016).
41. Zapotocky, M., Ramos, L., Poulin, P., Lubensky, T.C. & Weitz, D.A. Particle-stabilized defect gel in cholesteric liquid crystals. *Science* **283**, 209-212 (1999).
42. Ramos, L., Zapotocky, M., Lubensky, T.C. & Weitz, D.A. Rheology of defect networks in cholesteric liquid crystals. *Physical Review E* **66**, 031711 (2002).
43. Mitov, M. Cholesteric Liquid Crystals with a Broad Light Reflection Band. *Advanced Materials* **24**, 6260-6276 (2012).
44. Mulder, D.J., Schenning, A.P.H.J. & Bastiaansen, C.W.M. Chiral-nematic liquid crystals as one dimensional photonic materials in optical sensors. *Journal of Materials Chemistry C* **2**, 6695-6705 (2014).
45. Kahn, F.J. Electric-Field-Induced Color Changes and Pitch Dilation in Cholesteric Liquid Crystals. *Physical Review Letters* **24**, 209 (1970).
46. Hikmet, R.A.M. & Kemperman, H. Electrically switchable mirrors and optical components made from liquid-crystal gels. *Nature* **392**, 476-479 (1998).
47. Meyer, R.B. Effects of Electric and Magnetic Fields on Structure of Cholesteric Liquid Crystals. *Applied Physics Letters* **12**, 281 (1968).
48. Meyer, R.B. Distortion of a Cholesteric Structure by a Magnetic Field. *Applied Physics Letters* **14**, 208 (1969).
49. Durand, G., Leger, L., Rondelez, F. & Veyssie, M. Magnetically Induced Cholesteric-to-Nematic Phase Transition in Liquid Crystals. *Physical Review Letters* **22**, 227 (1969).
50. Chanishvili, A. et al. Phototunable lasing in dye-doped cholesteric liquid crystals. *Applied Physics Letters* **83**, 5353-5355 (2003).
51. Furumi, S., Yokoyama, S., Otomo, A. & Mashiko, S. Phototunable photonic bandgap in a chiral liquid crystal laser device. *Applied Physics Letters* **84**, 2491-2493 (2004).
52. Chanishvili, A. et al. Widely tunable ultraviolet-visible liquid crystal laser. *Applied Physics Letters* **86**, 051107 (2005).
53. Huang, Y.H., Chen, L.P., Doyle, C., Zhou, Y. & Wu, S.T. Spatially tunable laser emission in dye-doped cholesteric polymer films. *Applied Physics Letters* **89**, 111106 (2006).
54. Ilchishin, I.P., Tikhonov, E.A., Tishchenko, V.G. & Shpak, M.T. Generation of a Tunable Radiation by Impurity Cholesteric Liquid-Crystals. *Jetp Letters* **32**, 24-27 (1980).
55. Watanabe, J. & Nagase, T. Thermotropic Polypeptides .5. Temperature-Dependence of Cholesteric Pitches Exhibiting a Cholesteric Sense Inversion. *Macromolecules* **21**, 171-175 (1988).
56. Funamoto, K., Ozaki, M. & Yoshino, K. Discontinuous shift of lasing wavelength with temperature in cholesteric liquid crystal. *Japanese Journal of Applied Physics Part 2-Letters* **42**, L1523-L1525 (2003).
57. Warner, M., Terentjev, E.M., Meyer, R.B. & Mao, Y. Untwisting of a cholesteric elastomer by a mechanical field. *Physical Review Letters* **85**, 2320-2323 (2000).
58. Finkelmann, H., Kim, S.T., Munoz, A., Palffy-Muhoray, P. & Taheri, B. Tunable mirrorless lasing in cholesteric liquid crystalline elastomers. *Advanced Materials* **13**, 1069 (2001).

59. Xiang, J. et al. Electrically Tunable Selective Reflection of Light from Ultraviolet to Visible and Infrared by Heliconical Cholesterics. *Advanced Materials* **27**, 3014-3018 (2015).
60. Choi, S.S., Morris, S.M., Huck, W.T.S. & Coles, H.J. Electrically Tuneable Liquid Crystal Photonic Bandgaps. *Advanced Materials* **21**, 3915 (2009).
61. Ahmad, F., Jamil, M. & Jeon, Y.J. Reverse mode polymer stabilized cholesteric texture (PSCT) light shutter display - A short review. *Journal of Molecular Liquids* **233**, 187-196 (2017).
62. Crissey, J.T., Fergason, J.L. & Bettenhausen, J.M. Cutaneous Thermography with Liquid Crystals. *Journal of Investigative Dermatology* **45**, 329 (1965).
63. Khandelwal, H., Schenning, A.P.H.J. & Debije, M.G. Infrared Regulating Smart Window Based on Organic Materials. *Advanced Energy Materials* **7**, 1602209 (2017).
64. Broer, D.J., Lub, J. & Mol, G.N. Wide-Band Reflective Polarizers from Cholesteric Polymer Networks with a Pitch Gradient. *Nature* **378**, 467-469 (1995).
65. Coles, H. & Morris, S. Liquid-crystal lasers. *Nature Photonics* **4**, 676-685 (2010).
66. Vanmegen, W. & Snook, I. Solvent Structure and Solvation Forces between Solid Bodies. *Journal of the Chemical Society-Faraday Transactions Ii* **75**, 1095-1102 (1979).
67. Horn, R.G. & Israelachvili, J.N. Direct Measurement of Structural Forces between 2 Surfaces in a Non-Polar Liquid. *Journal of Chemical Physics* **75**, 1400-1411 (1981).
68. Christenson, H.K., Horn, R.G. & Israelachvili, J.N. Measurement of Forces Due to Structure in Hydrocarbon Liquids. *Journal of Colloid and Interface Science* **88**, 79-88 (1982).
69. Thompson, P.A. & Robbins, M.O. Shear-Flow near Solids - Epitaxial Order and Flow Boundary-Conditions. *Physical Review A* **41**, 6830-6837 (1990).
70. Blinov, L.M., Kats, E.I. & Sonin, A.A. Surface Physics of Thermotropic Liquid-Crystals. *Uspekhi Fizicheskikh Nauk* **152**, 449-477 (1987).
71. Kleman, M. & Laverntovich, O.D. Soft matter physics an introduction (Springer Science & Business Media, 2003).
72. Yokoyama, H. Surface Anchoring of Nematic Liquid-Crystals. *Molecular Crystals and Liquid Crystals* **165**, 265-316 (1988).
73. Jerome, B. Surface Effects and Anchoring in Liquid-Crystals. *Reports on Progress in Physics* **54**, 391-451 (1991).
74. Barbero, G. & Evangelista, L.R. Adsorption phenomena and anchoring energy in nematic liquid crystals (Taylor & Francis, Boca Raton, 2006).
75. Rapini, A., Papoular, M. & Pincus, P. Structural Distortion of a Nematic Film under a Magnetic Field. *Comptes Rendus Hebdomadaires Des Seances De L Academie Des Sciences Serie B* **267**, 1230 (1968).
76. Jerome, B. & Shen, Y.R. Anchoring of Nematic Liquid-Crystals on Mica in the Presence of Volatile Molecules. *Physical Review E* **48**, 4556-4574 (1993).
77. Szilvasi, T. et al. Design of Chemoresponsive Liquid Crystals through Integration of Computational Chemistry and Experimental Studies. *Chemistry of Materials* **29**, 3563-3571 (2017).
78. Szilvasi, T. et al. The role of anions in adsorbate-induced anchoring transitions of liquid crystals on surfaces with discrete cation binding sites. *Soft Matter* **14**, 797-805 (2018).

79. Cao, Y.K., Yu, H.Z., Abbott, N.L. & Zavala, V.M. Machine Learning Algorithms for Liquid Crystal-Based Sensors. *Acs Sensors* **3**, 2237-2245 (2018).
80. Mezger, M. et al. Molecular layering of fluorinated ionic liquids at a charged sapphire (0001) surface. *Science* **322**, 424-428 (2008).
81. Zobel, M., Neder, R.B. & Kimber, S.A.J. Universal solvent restructuring induced by colloidal nanoparticles. *Science* **347**, 292-294 (2015).
82. Stark, H. Saturn-ring defects around microspheres suspended in nematic liquid crystals: An analogy between confined geometries and magnetic fields. *Physical Review E* **66**, 032701 (2002).
83. Gryn, I., Lacaze, E., Bartolino, R. & Zappone, B. Controlling the Self-Assembly of Periodic Defect Patterns in Smectic Liquid Crystal Films with Electric Fields. *Advanced Functional Materials* **25**, 142-149 (2015).
84. Castellano, J.A. Surface Anchoring of Liquid-Crystal Molecules on Various Substrates. *Molecular Crystals and Liquid Crystals* **94**, 33-41 (1983).
85. Berreman, D.W. Solid Surface Shape and Alignment of an Adjacent Nematic Liquid-Crystal. *Physical Review Letters* **28**, 1683 (1972).
86. Berreman, D.W. Alignment of Liquid-Crystals by Grooved Surfaces. *Molecular Crystals and Liquid Crystals* **23**, 215-231 (1973).
87. Wolff, U., Greubel, W. & Kruger, H. Homogeneous Alignment of Liquid-Crystal Layers. *Molecular Crystals and Liquid Crystals* **23**, 187-196 (1973).
88. Barbero, G. Surface Geometry and Induced Orientation of a Nematic Liquid-Crystal. *Lettere Al Nuovo Cimento* **29**, 553-559 (1980).
89. Geary, J.M., Goodby, J.W., Kmetz, A.R. & Patel, J.S. The Mechanism of Polymer Alignment of Liquid-Crystal Materials. *Journal of Applied Physics* **62**, 4100-4108 (1987).
90. Cheng, K.C.K. et al. Templated nanofiber synthesis via chemical vapor polymerization into liquid crystalline films. *Science* **362**, 804 (2018).
91. Proust, J.E., Terminas.L & Guyon, E. Orientation of a Nematic Liquid-Crystal by Suitable Boundary Surfaces. *Solid State Communications* **11**, 1227 (1972).
92. Stohr, J. et al. Liquid crystal alignment on carbonaceous surfaces with orientational order. *Science* **292**, 2299-2302 (2001).
93. Gupta, V.K. & Abbott, N.L. Design of surfaces for patterned alignment of liquid crystals on planar and curved substrates. *Science* **276**, 1533-1536 (1997).
94. Patel, J.S. & Yokoyama, H. Continuous Anchoring Transition in Liquid-Crystals. *Nature* **362**, 525-527 (1993).
95. Gibbons, W.M., Shannon, P.J., Sun, S.T. & Swetlin, B.J. Surface-Mediated Alignment of Nematic Liquid-Crystals with Polarized Laser-Light. *Nature* **351**, 49-50 (1991).
96. Schadt, M., Schmitt, K., Kozinkov, V. & Chigrinov, V. Surface-Induced Parallel Alignment of Liquid-Crystals by Linearly Polymerized Photopolymers. *Japanese Journal of Applied Physics Part 1-Regular Papers Short Notes & Review Papers* **31**, 2155-2164 (1992).
97. Skaife, J.J. & Abbott, N.L. Quantitative interpretation of the optical textures of liquid crystals caused by specific binding of immunoglobulins to surface-bound antigens. *Langmuir* **16**, 3529-3536 (2000).
98. Shah, R.R. & Abbott, N.L. Principles for measurement of chemical exposure based on recognition-driven anchoring transitions in liquid crystals. *Science* **293**, 1296-1299 (2001).

99. Carlton, R.J. et al. Chemical and biological sensing using liquid crystals. *Liquid Crystals Reviews* **1**, 29-51 (2013).
100. Lin, I.H. et al. Endotoxin-Induced Structural Transformations in Liquid Crystalline Droplets. *Science* **332**, 1297-1300 (2011).
101. Janning, J.L. Thin-Film Surface Orientation for Liquid-Crystals. *Applied Physics Letters* **21**, 173 (1972).
102. Turiv, T. et al. Effect of Collective Molecular Reorientations on Brownian Motion of Colloids in Nematic Liquid Crystal. *Science* **342**, 1351-1354 (2013).
103. Ruhwandl, R.W. & Terentjev, E.M. Friction drag on a particle moving in a nematic liquid crystal. *Physical Review E* **54**, 5204-5210 (1996).
104. Stark, H. & Ventzki, D. Stokes drag of spherical particles in a nematic environment at low Ericksen numbers. *Physical Review E* **64**, 031711 (2001).
105. Loudet, J.C., Hanusse, P. & Poulin, P. Stokes drag on a sphere in a nematic liquid crystal. *Science* **306**, 1525-1525 (2004).
106. Mondiot, F. et al. Stokes-Einstein diffusion of colloids in nematics. *Physical Review E* **86**, 010401 (2012).
107. Abbott, N.L. Colloid Science Collides with Liquid Crystals. *Science* **342**, 1326-1327 (2013).
108. Hashemi, S.M. et al. Fractal nematic colloids. *Nature Communications* **8**, 1 (2017).
109. Araki, T., Buscaglia, M., Bellini, T. & Tanaka, H. Memory and topological frustration in nematic liquid crystals confined in porous materials. *Nature Materials* **10**, 303-309 (2011).
110. Yokoyama, H. Nematic Isotropic Transition in Bounded Thin-Films. *Journal of the Chemical Society-Faraday Transactions Ii* **84**, 1023-1040 (1988).
111. Golemme, A., Zumer, S., Allender, D.W. & Doane, J.W. Continuous Nematic-Isotropic Transition in Submicron-Size Liquid-Crystal Droplets. *Physical Review Letters* **61**, 2937-2940 (1988).
112. Kityk, A.V. et al. Continuous Paranematic-to-Nematic Ordering Transitions of Liquid Crystals in Tubular Silica Nanochannels. *Physical Review Letters* **101**, 187801 (2008).
113. Urbanski, M. et al. Liquid crystals in micron-scale droplets, shells and fibers. *Journal of Physics-Condensed Matter* **29**, 133003 (2017).
114. Wang, P.X. & MacLachlan, M.J. Liquid crystalline tactoids: ordered structure, defective coalescence and evolution in confined geometries. *Philosophical Transactions of the Royal Society a-Mathematical Physical and Engineering Sciences* **376**, 20170042 (2018).
115. Mirantsev, L.V., de Oliveira, E.J.L., de Oliveira, I.N. & Lyra, M.L. Defect structures in nematic liquid crystal shells of different shapes. *Liquid Crystals Reviews* **4**, 35-58 (2016).
116. Kralj, S., Zumer, S. & Allender, D.W. Nematic-Isotropic Phase-Transition in a Liquid-Crystal Droplet. *Physical Review A* **43**, 2943-2954 (1991).
117. Fernandez-Nieves, A. et al. Novel defect structures in nematic liquid crystal shells. *Physical Review Letters* **99**, 157801 (2007).
118. Lopez-Leon, T., Koning, V., Devaiah, K.B.S., Vitelli, V. & Fernandez-Nieves, A. Frustrated nematic order in spherical geometries. *Nature Physics* **7**, 391-394 (2011).
119. Bezic, J. & Zumer, S. Structures of the Cholesteric Liquid-Crystal Droplets with Parallel Surface Anchoring. *Liquid Crystals* **11**, 593-619 (1992).

120. Li, Y.F. et al. Colloidal cholesteric liquid crystal in spherical confinement. *Nature Communications* **7**, 12520 (2016).
121. Tran, L. et al. Change in Stripes for Cholesteric Shells via Anchoring in Moderation. *Physical Review X* **7**, 041029 (2017).
122. Humar, M. & Musevic, I. 3D microlasers from self-assembled cholesteric liquid-crystal microdroplets. *Optics Express* **18**, 26995-27003 (2010).
123. Fréedericksz, V. & Zolina, V. Forces causing the orientation of an anisotropic liquid. *Transactions of the Faraday Society* **29**, 919 (1933).
124. Huang, Y.H., Wu, T.X. & Wu, S.T. Simulations of liquid-crystal Fabry-Perot etalons by an improved 4X4 matrix method. *Journal of Applied Physics* **93**, 2490-2495 (2003).
125. Kristiansen, K., Zeng, H.B., Zappone, B. & Israelachvili, J.N. Simultaneous Measurements of Molecular Forces and Electro-Optical Properties of a Confined 5CB Liquid Crystal Film Using a Surface Forces Apparatus. *Langmuir* **31**, 3965-3972 (2015).
126. Rosenblatt, C. Liquid-Crystal Freedericksz Transition and Surface-Induced Smectic Ordering. *Physical Review Letters* **53**, 791-794 (1984).
127. Baessler, H. & Labes, M.M. Relationship between Electric Field Strength and Helix Pitch in Induced Cholesteric-Nematic Phase Transitions. *Physical Review Letters* **21**, 1791 (1968).
128. Belyaev, S.V. & Blinov, L.M. Step Unwinding of a Spiral in a Cholesteric Liquid-Crystal. *Jetp Letters* **30**, 99-103 (1979).
129. Dreher, R. Remarks on Distortion of a Cholesteric Structure by a Magnetic-Field. *Solid State Communications* **13**, 1571-1574 (1973).
130. Brokx, J., Vertogen, G. & Vangroesen, E.W.C. On the Field-Induced Cholesteric-Nematic Transition in Cholesteric Liquid-Crystals with Homeotropic Boundary-Conditions. *Zeitschrift Fur Naturforschung Section a-a Journal of Physical Sciences* **38**, 1-9 (1983).
131. Lee, J.C., Allender, D.W. & Neff, V.D. The Effect of Homeotropic Surface Anchoring on the Critical Voltage for Unwinding the Cholesteric Phase. *Molecular Crystals and Liquid Crystals* **210**, 11-20 (1992).
132. Kedney, P.J. & Stewart, I.W. The Untwisting of a Bounded Sample of Cholesteric Liquid-Crystal. *Continuum Mechanics and Thermodynamics* **6**, 141-148 (1994).
133. Xianyu, H.Q., Faris, S. & Crawford, G.P. In-plane switching of cholesteric liquid crystals for visible and near-infrared applications. *Applied Optics* **43**, 5006-5015 (2004).
134. Uto, S. A helix unwinding process in ferroelectric liquid crystals with fixed boundaries. *Journal of Applied Physics* **97** (2005).
135. Zakhlevnykh, A.N. & Shavkunov, V.S. Magnetic-field-induced stepwise director reorientation and untwisting of a planar cholesteric structure with finite anchoring energy. *Physical Review E* **94**, 042708 (2016).
136. Zink, H. & Belyakov, V.A. Determination of changes in director orientation with temperature in oriented cholesteric layers. *Molecular Crystals and Liquid Crystals Science and Technology Section a-Molecular Crystals and Liquid Crystals* **282**, 17-26 (1996).
137. Belyakov, V.A., Stewart, I.W. & Osipov, M.A. Surface anchoring and dynamics of jump-wise director reorientations in planar cholesteric layers. *Physical Review E* **71**, 051708 (2005).

138. Kiselev, A.D. & Sluckin, T.J. Twist of cholesteric liquid crystal cells: Stability of helical structures and anchoring energy effects. *Physical Review E* **71**, 031704 (2005).
139. Mckay, G. Bistable surface anchoring and hysteresis of pitch jumps in a planar cholesteric liquid crystal. *European Physical Journal E* **35**, 1 (2012).
140. Lelidis, I., Barbero, G. & Alexe-Ionescu, A.L. Cholesteric pitch transitions induced by mechanical strain. *Physical Review E* **87**, 022503 (2013).
141. de Souza, R.F. et al. Surface induced twist in nematic and chiral nematic liquid crystals: stick-slip-like and constrained motion. *Soft Matter* **14**, 2084-2093 (2018).
142. Oswald, P., Dequidt, A. & Zywocinski, A. Sliding planar anchoring and viscous surface torque in a cholesteric liquid crystal. *Physical Review E* **77**, 061703 (2008).
143. de Souza, R.F., Yang, D.K., Lenzi, E.K., Evangelista, L.R. & Zola, R.S. Effect of surface viscosity, anchoring energy, and cell gap on the response time of nematic liquid crystals. *Annals of Physics* **346**, 14-21 (2014).
144. Nie, X.Y., Lu, R.B., Xianyu, H.Q., Wu, T.X. & Wu, S.T. Anchoring energy and cell gap effects on liquid crystal response time. *Journal of Applied Physics* **101**, 103110 (2007).
145. Yoon, H.G., Roberts, N.W. & Gleeson, H.F. An experimental investigation of discrete changes in pitch in a thin, planar chiral nematic device. *Liquid Crystals* **33**, 503-510 (2006).
146. Orlova, T.N., Iegorov, R.I. & Kiselev, A.D. Light-induced pitch transitions in photosensitive cholesteric liquid crystals: Effects of anchoring energy. *Physical Review E* **89**, 012503 (2014).
147. Britton, J. et al. A Graphene Surface Force Balance. *Langmuir* **30**, 11485-11492 (2014).
148. Israelachvili, J.N. & Adams, G.E. Direct Measurement of Long-Range Forces between 2 Mica Surfaces in Aqueous Kno3 Solutions. *Nature* **262**, 773-776 (1976).
149. Israelachvili, J.N. & Tabor, D. Measurement of Van-Der-Waals Dispersion Forces in Range 1.4 to 130 Nm. *Nature-Physical Science* **236**, 106 (1972).
150. Tabor, D. & Winterto.Rh. Direct Measurement of Normal and Retarded Van Der Waals Forces. *Proceedings of the Royal Society of London Series a-Mathematical and Physical Sciences* **312**, 435 (1969).
151. Israelachvili, J.N. Thin-Film Studies Using Multiple-Beam Interferometry. *Journal of Colloid and Interface Science* **44**, 259-272 (1973).
152. Israelachvili, J. et al. Recent advances in the surface forces apparatus (SFA) technique. *Reports on Progress in Physics* **73**, 036601 (2010).
153. Klein, J. & Kumacheva, E. Simple liquids confined to molecularly thin layers. I. Confinement-induced liquid-to-solid phase transitions. *Journal of Chemical Physics* **108**, 6996-7009 (1998).
154. Christenson, H.K. & Thomson, N.H. The nature of the air-cleaved mica surface. *Surface Science Reports* **71**, 367-390 (2016).
155. Sridhar, I., Johnson, K.L. & Fleck, N.A. Adhesion mechanics of the surface force apparatus. *Journal of Physics D-Applied Physics* **30**, 1710-1719 (1997).
156. Klein, J. Forces between Mica Surfaces Bearing Adsorbed Macromolecules in Liquid-Media. *Journal of the Chemical Society-Faraday Transactions I* **79**, 99 (1983).

157. van Engers, C.D., Balabajew, M., Southam, A. & Perkin, S. A 3-mirror surface force balance for the investigation of fluids confined to nanoscale films between two ultra-smooth polarizable electrodes. *Review of Scientific Instruments* **89**, 123901 (2018).
158. Kristiansen, K., Donaldson, J.S.H., Berkson, Z.J. & al., e. Multimodal miniature surface forces apparatus. *arXiv preprint* (2019).
159. Idziak, S.H.J. et al. The X-Ray Surface Forces Apparatus - Structure of a Thin Smectic Liquid-Crystal Film under Confinement. *Science* **264**, 1915-1918 (1994).
160. Heuberger, M. The extended surface forces apparatus. Part I. Fast spectral correlation interferometry. *Review of Scientific Instruments* **72**, 1700-1707 (2001).
161. Heuberger, M., Vanicek, J. & Zach, M. The extended surface forces apparatus. II. Precision temperature control. *Review of Scientific Instruments* **72**, 3556-3560 (2001).
162. Zach, M., Vanicek, J. & Heuberger, M. The extended surface forces apparatus. Part III. High-speed interferometric distance measurement. *Review of Scientific Instruments* **74**, 260-266 (2003).
163. Dushkin, C.D. & Kurihara, K. A resonance shear force rheometer modeled as simple oscillating circuit. *Review of Scientific Instruments* **69**, 2095-2104 (1998).
164. Restagno, F., Crassous, J., Charlaix, E., Cottin-Bizonne, C. & Monchanin, M. A new surface forces apparatus for nanorheology. *Review of Scientific Instruments* **73**, 2292-2297 (2002).
165. Cho, Y.K. & Granick, S. A surface forces platform for dielectric measurements. *Journal of Chemical Physics* **119**, 547-554 (2003).
166. Luesse, C., Vanalsten, J., Carson, G. & Granick, S. Drive Mechanism for a Surface Force Apparatus. *Review of Scientific Instruments* **59**, 811-812 (1988).
167. Ruths, M., Steinberg, S. & Israelachvili, J.N. Effects of confinement and shear on the properties of thin films of thermotropic liquid crystal. *Langmuir* **12**, 6637-6650 (1996).
168. Kitaev, V. & Kumacheva, E. Thin films of liquid crystals confined between crystalline surfaces. *Journal of Physical Chemistry B* **104**, 8822-8829 (2000).
169. Artsyukhovich, A., Broekman, L.D. & Salmeron, M. Friction of the liquid crystal 8CB as probed by the surface forces apparatus. *Langmuir* **15**, 2217-2223 (1999).
170. Mcguiggan, P.M. & Israelachvili, J.N. Adhesion and Short-Range Forces between Surfaces .2. Effects of Surface Lattice Mismatch. *Journal of Materials Research* **5**, 2232-2243 (1990).
171. Rabinowitz, P. Eigenvalue Analysis of the Surface Forces Apparatus Interferometer. *Journal of the Optical Society of America a-Optics Image Science and Vision* **12**, 1593-1601 (1995).
172. Janik, J., Tadmor, R. & Klein, J. Shear of molecularly confined liquid crystals .1. Orientation and transitions under confinement. *Langmuir* **13**, 4466 (1997).
173. Janik, J., Tadmor, R. & Klein, J. Shear of molecularly confined liquid crystals. 2. Stress anisotropy across a model nematogen compressed between sliding solid surfaces. *Langmuir* **17**, 5476-5485 (2001).
174. Pieranski, P. & Jerome, B. Adsorption-Induced Anchoring Transitions at Nematic Liquid-Crystal - Crystal Interfaces. *Physical Review A* **40**, 317-322 (1989).
175. Ruths, M. & Zappone, B. Direct Nanomechanical Measurement of an Anchoring Transition in a Nematic Liquid Crystal Subject to Hybrid Anchoring Conditions. *Langmuir* **28**, 8371-8383 (2012).

176. Carbone, G., Lombardo, G., Barberi, R., Musevic, I. & Tkalec, U. Mechanically Induced Biaxial Transition in a Nanoconfined Nematic Liquid Crystal with a Topological Defect. *Physical Review Letters* **103**, 167801 (2009).
177. Krishnan, M., Ugaz, V.M. & Burns, M.A. PCR in a Rayleigh-Benard convection cell. *Science* **298**, 793-793 (2002).
178. Horn, R.G., Israelachvili, J.N. & Perez, E. Forces Due to Structure in a Thin Liquid-Crystal Film. *Journal De Physique* **42**, 39-52 (1981).
179. Chan, D.Y.C. & Horn, R.G. The Drainage of Thin Liquid-Films between Solid-Surfaces. *Journal of Chemical Physics* **83**, 5311-5324 (1985).
180. Zappone, B., Richetti, P., Barberi, R., Bartolino, R. & Nguyen, H.T. Forces in nematic liquid crystals constrained to the nanometer scale under hybrid anchoring conditions. *Physical Review E* **71** (2005).
181. Kekicheff, P. & Christenson, H.K. Forces Measured in a Swollen Lyotropic Lamellar Mesophase Confined between Solid-Surfaces. *Physical Review Letters* **63**, 2823-2826 (1989).
182. Richetti, P., Kekicheff, P., Parker, J.L. & Ninham, B.W. Measurement of the Interactions between Membranes in a Stack. *Nature* **346**, 252-254 (1990).
183. Herke, R.A., Clark, N.A. & Handschy, M.A. Stress-Induced Vortex Line Helixing Avalanches in the Plastic-Flow of a Smectic a Liquid-Crystal. *Science* **267**, 651-654 (1995).
184. Mao, Y., Cates, M.E. & Lekkerkerker, H.N.W. Depletion force in colloidal systems. *Physica A* **222**, 10-24 (1995).
185. Herke, R.A., Clark, N.A. & Handschy, M.A. Dynamic behavior of oscillatory plastic flow in a smectic liquid crystal. *Physical Review E* **56**, 3028-3043 (1997).
186. Blanc, C., Zuodar, N., Lelidis, I., Kleman, M. & Martin, J.L. Defect dynamics in a smectic Grandjean-Cano wedge. *Physical Review E* **69**, 011705 (2004).
187. Blanc, C., Zuodar, N., Martin, J.L., Lelidis, I. & Kleman, M. Role of microscopic defects in the plasticity of lamellar materials. *Molecular Crystals and Liquid Crystals* **412**, 1695-1702 (2004).
188. Lelidis, I., Blanc, C. & Kleman, M. Optical and confocal microscopy observations of screw dislocations in smectic-A liquid crystals. *Physical Review E* **74**, 051710 (2006).
189. Kneppe, H., Schneider, F. & Sharma, N.K. A Comparative-Study of the Viscosity Coefficients of Some Nematic Liquid-Crystals. *Berichte Der Bunsen-Gesellschaft-Physical Chemistry Chemical Physics* **85**, 784-789 (1981).
190. Helfrich, W. Capillary Flow of Cholesteric and Smectic Liquid Crystals. *Physical Review Letters* **23**, 372 (1969).
191. Michel-Levy Birefringence Chart (https://www.olympus-lifescience.com/zh/microscope-resource/primer/techniques/polarized/michel/).
192. Perkin, S. et al. Forces between mica surfaces, prepared in different ways, across aqueous and nonaqueous liquids confined to molecularly thin films. *Langmuir* **22**, 6142-6152 (2006).
193. Horn, R.G. & Smith, D.T. Analytic Solution for the 3-Layer Multiple Beam Interferometer. *Applied Optics* **30**, 59-65 (1991).
194. Clarkson, M.T. Multiple-Beam Interferometry with Thin Metal-Films and Unsymmetrical Systems. *Journal of Physics D-Applied Physics* **22**, 475-482 (1989).

195. Levins, J.M. & Vanderlick, T.K. Extended Spectral-Analysis of Multiple-Beam Interferometry - a Technique to Study Metallic-Films in the Surface Forces Apparatus. *Langmuir* **10**, 2389-2394 (1994).
196. Kienle, D.F. & Kuhl, T.L. Analyzing Refractive Index Profiles of Confined Fluids by Interferometry. *Analytical Chemistry* **86**, 11860-11867 (2014).
197. Kienle, D.F. & Kuhl, T.L. Analyzing refractive index profiles of confined fluids by interferometry part II: Multilayer and asymmetric systems. *Analytica Chimica Acta* **936**, 236-244 (2016).
198. Born, M., Wolf, E. & Bhatia, A.B. Principles of optics : electromagnetic theory of propagation, interference and diffraction of light (Cambridge University Press, Cambridge, 1999).
199. Zappone, B., Zheng, W.C. & Perkin, S. Multiple-beam optical interferometry of anisotropic soft materials nanoconfined with the surface force apparatus. *Review of Scientific Instruments* **89**, 085112 (2018).
200. Schwenzfeier, K.A. et al. Optimizing multiple beam interferometry in the surface forces apparatus: Novel optics, reflection mode modeling, metal layer thicknesses, birefringence, and rotation of anisotropic layers. *Review of Scientific Instruments* **90**, 043908 (2019).
201. Berreman, D.W. Optics in Stratified and Anisotropic Media - 4x4-Matrix Formulation. *Journal of the Optical Society of America* **62**, 502 (1972).
202. Schubert, M. Polarization-dependent optical parameters of arbitrarily anisotropic homogeneous layered systems. *Physical Review B* **53**, 4265-4274 (1996).
203. Miyagi, K. & Teramoto, Y. Dual mechanochromism of cellulosic cholesteric liquid-crystalline films: wide-ranging colour control and circular dichroism inversion by mechanical stimulus. *Journal of Materials Chemistry C* **6**, 1370-1376 (2018).
204. Zheng, W.C., Perez-Martinez, C.S., Petriashvili, G., Perkin, S. & Zappone, B. Direct measurements of structural forces and twist transitions in cholesteric liquid crystal films with a surface force apparatus. *Soft Matter* **15**, 4905-4914 (2019).
205. Richetti, P., Kekicheff, P. & Barois, P. Measurement of the Layer Compressibility Modulus of a Lamellar Mesophase with a Surface Forces Apparatus. *Journal De Physique Ii* **5**, 1129-1154 (1995).
206. Lhermerout, R. & Perkin, S. Nanoconfined ionic liquids: Disentangling electrostatic and viscous forces. *Physical Review Fluids* **3**, 014201 (2018).
207. Grass, A.J. Structural Features of Turbulent Flow over Smooth and Rough Boundaries. *Journal of Fluid Mechanics* **50**, 233 (1971).
208. Lauga, E., Brenner, M. & Stone, H. Microfluidics: the no-slip boundary condition. *Springer handbook of experimental fluid mechanics*, 1219-1240 (2007).
209. Bonn, D., Denn, M.M., Berthier, L., Divoux, T. & Manneville, S. Yield stress materials in soft condensed matter. *Reviews of Modern Physics* **89**, 035005 (2017).
210. Smalyukh, I.I. & Lavrentovich, O.D. Three-dimensional director structures of defects in Grandjean-Cano wedges of cholesteric liquid crystals studied by fluorescence confocal polarizing microscopy. *Physical Review E* **66**, 051703 (2002).
211. Erk, K.A., Henderson, K.J. & Shull, K.R. Strain Stiffening in Synthetic and Biopolymer Networks. *Biomacromolecules* **11**, 1358-1363 (2010).
212. Cubuk, E.D. et al. Structure-property relationships from universal signatures of plasticity in disordered solids. *Science* **358**, 1033-1037 (2017).

213. Tawfick, S. & Tang, Y.C. Stronger artificial muscles, with a twist. *Science* **365**, 125-126 (2019).
214. Rotational Friction (https://uk.mathworks.com/help/physmod/simscape/ref/rotationalfriction.html).
215. Lavrentovich, O.D. & Yang, D.K. Cholesteric cellular patterns with electric-field-controlled line tension. *Physical Review E* **57**, R6269-R6272 (1998).
216. Sano, T.G., Yamaguchi, T. & Wada, H. Slip Morphology of Elastic Strips on Frictional Rigid Substrates. *Physical Review Letters* **118** (2017).
217. Bayart, E., Svetlizky, I. & Fineberg, J. Fracture mechanics determine the lengths of interface ruptures that mediate frictional motion. *Nature Physics* **12**, 166 (2016).
218. Svetlizky, I. & Fineberg, J. Classical shear cracks drive the onset of dry frictional motion. *Nature* **509**, 205-+ (2014).
219. Svetlizky, I., Bayart, E. & Fineberg, J. Brittle Fracture Theory Describes the Onset of Frictional Motion. *Annual Review of Condensed Matter Physics* **10**, 253 (2019).
220. Bayart, E., Svetlizky, I. & Fineberg, J. Slippery but Tough: The Rapid Fracture of Lubricated Frictional Interfaces. *Physical Review Letters* **116**, 194301 (2016).
221. Rosenhek-Goldian, I., Kampf, N., Yeredor, A. & Klein, J. On the question of whether lubricants fluidize in stick-slip friction. *Proceedings of the National Academy of Sciences of the United States of America* **112**, 7117-7122 (2015).
222. Marenduzzo, D., Orlandini, E. & Yeomans, J.M. Permeative flows in cholesteric liquid crystals. *Physical Review Letters* **92**, 1-4 (2004).
223. Moller, P.C.F., Fall, A. & Bonn, D. Origin of apparent viscosity in yield stress fluids below yielding. *Epl* **87** (2009).
224. Yuk, H., Zhang, T., Lin, S.T., Parada, G.A. & Zhao, X.H. Tough bonding of hydrogels to diverse non-porous surfaces. *Nature Materials* **15**, 190 (2016).
225. Lin, J.S., Wang, L.W. & Chen, G.H. Modification of Graphene Platelets and their Tribological Properties as a Lubricant Additive. *Tribology Letters* **41**, 209-215 (2011).
226. Pelham, R.J. & Wang, Y.L. Cell locomotion and focal adhesions are regulated by substrate flexibility (vol 94, pg 13661, 1997). *Proceedings of the National Academy of Sciences of the United States of America* **95**, 12070-12070 (1998).
227. Fukuda, J. & Zumer, S. Structural forces in liquid crystalline blue phases. *Physical Review E* **84**, 040701 (2011).
228. Eelkema, R. et al. Nanomotor rotates microscale objects. *Nature* **440**, 163-163 (2006).
229. Donato, M.G. et al. Polarization-dependent optomechanics mediated by chiral microresonators. *Nature Communications* **5**, 3656 (2014).
230. Ozawa, T. et al. Topological photonics. *Reviews of Modern Physics* **91**, 015006 (2019).